

# Molecular inventory of a young eruptive star's environment

## Case study of the classical FU Orionis star V1057 Cyg

Zs. M. Szabó<sup>1,2,3,\*</sup>, A. Belloche<sup>1</sup>, K. M. Menten<sup>1,\*\*</sup>, Y. Gong<sup>4,1</sup>, Á. Kóspál<sup>3,5,7</sup>, P. Ábrahám<sup>3,5</sup>, W. Yang<sup>6,1</sup>, C. J. Cyganowski<sup>2</sup>, and F. Wyrowski<sup>1</sup>

<sup>1</sup> Max-Planck-Institut für Radioastronomie, Auf dem Hügel 69, 53121 Bonn, Germany

e-mail: zszabo@mpi-fr-bonn.mpg.de

<sup>2</sup> Scottish Universities Physics Alliance (SUPA), School of Physics and Astronomy, University of St Andrews, North Haugh, St Andrews, KY16 9SS, UK

<sup>3</sup> Konkoly Observatory, HUN-REN Research Centre for Astronomy and Earth Sciences, MTA Centre of Excellence, Konkoly-Thege Miklós út 15-17, 1121 Budapest, Hungary

<sup>4</sup> Purple Mountain Observatory, and Key Laboratory of Radio Astronomy, Chinese Academy of Sciences, 10 Yuanhua Road, Nanjing 210023, China

<sup>5</sup> Institute of Physics and Astronomy, ELTE Eötvös Loránd University, Pázmány Péter sétány 1/A, 1117 Budapest, Hungary

<sup>6</sup> School of Astronomy & Space Science, Nanjing University, 163 Xianlin Avenue, Nanjing 210023, People's Republic of China

<sup>7</sup> Max-Planck-Institut für Astronomie, Königstuhl 17, D-69117 Heidelberg, Germany

Received ; accepted

### ABSTRACT

**Context.** Studying accretion-driven episodic outbursts in young stellar objects (YSOs) is crucial for understanding the later stages of star and planet formation. FU Orionis type objects (briefly FUors) represent a small but rather pivotal class of YSOs, whose outbursts are characterised by a rapid, multi-magnitude increase in brightness at optical and near-infrared wavelengths. These outbursts may have a long-lasting influence on the chemistry and molecular inventory around eruptive young stars. However, no complete line survey in the millimeter wavelength range exists in the literature for more evolved (i.e., Class II) sources, in contrast to wideband coverages at optical and near-infrared wavelengths

**Aims.** We carried out the first dedicated wide-band millimeter line survey towards the low-mass young eruptive star and classical FUor V1057 Cyg, which has the highest observed peak accretion rate among FUors. This source is known to have a molecular outflow, and is associated with dense material, making it a good candidate to search for molecular species.

**Methods.** We performed a wideband spectral line survey of V1057 Cyg with the IRAM 30-m telescope from  $\sim 72$  to  $\sim 263$  GHz (with spatial resolution between  $\sim 36''$  and  $\sim 10''$ ), complemented by on-the-fly maps of selected molecules. We also recorded additional spectra around 219, 227, 291, and 344 GHz (with spatial resolution between  $\sim 30''$  and  $\sim 19''$ ) with the APEX 12-m telescope. We conducted simple radiative transfer and population diagram analyses to derive column densities and excitation temperatures. We constructed integrated intensity maps of the emission from several molecular species, including those that reveal outflows. These maps a  $^{12}\text{CO}$  (3–2) position-velocity diagram provide insight into the past outburst activity of the source.

**Results.** We identified mainly simple C-, N-, O-, S-bearing molecules, deuterated species, molecular ions, and complex organic molecules. Several molecular species (HCN,  $\text{HC}_3\text{N}$ , and HNC) trace large-scale ( $\sim 2'$ ) structures in the environment of V1057 Cyg with hints of small-scale fragmentation that remains unresolved by the single-dish data. The position-velocity diagram of  $^{12}\text{CO}$  shows concentrated knots, which may indicate past episodic outburst activity. We calculated the dynamical timescale of the outflow and found it to be on the order of a few tens of thousands of years (between 15 000 and 22 000 years), similar to other eruptive stars, suggesting that the outflow cannot result from the ongoing outburst alone, since the source has been in the current outburst for less than a century. The population diagrams for species such as  $\text{CH}_3\text{OH}$ ,  $\text{H}_2\text{CO}$ ,  $\text{HC}_3\text{N}$ , indicate rotational temperatures ranging from 8 K to 15 K, and column densities ranging from  $1.4 \times 10^{12} \text{ cm}^{-2}$  to  $2.8 \times 10^{13} \text{ cm}^{-2}$ .

**Conclusions.** With over 30 molecular species (including isotopologues) detected, V1057 Cyg and its environment display a rich chemistry, considering the more evolved state of this source compared to well studied, but younger (i.e., Class 0/I) FUors like V883 Ori. The results of our line survey show that V1057 Cyg is a good candidate for future interferometric observations aimed at resolving emission extents to constrain molecular freeze-out and searching for emission lines of water and additional complex organic molecules. Our observations highlight the potential of mm line surveys to characterise the chemistry of eruptive stars and their environments, including more evolved sources, and so to complement optical and near-infrared studies in improving current statistics regarding the molecular inventories of these objects.

**Key words.** Stars: pre-main sequence – Stars: protostars – Stars: low-mass – Stars: variables: T Tauri – Stars: individual: V1057 Cyg – ISM: molecules – Line: identification – Circumstellar matter – Astrochemistry – Methods: observational – Methods: data analysis

\* Member of the International Max Planck Research School (IM-PRS) for Astronomy and Astrophysics at the Universities of Bonn and Cologne.

\*\* This work is dedicated to the memory of Karl M. Menten, who proposed the idea of the line survey. His profound knowledge, thoughtful

mentorship, unwavering guidance, and fruitful discussions inspired us throughout this journey. This work is a tribute to his vision and lasting impact.

## 1. Introduction

Young stellar objects (YSOs) undergo accretion-driven episodic outbursts. Studying the impact of these outbursts, in particular on the molecular composition of their environments, is fundamental for our understanding of star and planet formation. FU Orionis objects (briefly FUors) represent a small but rather pivotal class of YSOs, whose outbursts are primarily characterised by a rapid, multi-magnitude increase in brightness at optical and near-infrared wavelengths, attributed to a sudden increase in the accretion flow from the disk onto the protostar, a process lasting for several decades, likely centuries (for a recent review, see Fischer et al. 2023, and references therein). The prototype of the class, FU Orionis, went into outburst around 1936/1937 (Wachmann 1954). It was later considered as a new phenomenon different from a nova outburst (Herbig 1966), and eventually the FUor class was defined by Herbig (1977). During an outburst, the accretion rate of a FUor rises from the average rate of a typical T Tauri star of  $10^{-9} - 10^{-7} M_{\odot} \text{ yr}^{-1}$  up to  $10^{-5} - 10^{-4} M_{\odot} \text{ yr}^{-1}$  (e.g., Hartmann & Kenyon 1996; Audard et al. 2014).

The powerful and energetic FUor outbursts potentially have a long-lasting influence on the chemistry and molecular inventory of the disks around eruptive stars. The elevated temperatures can, temporarily, increase the abundances of complex organic molecules (COMs), which are carbon-bearing molecules with six or more atoms (e.g., Herbst & van Dishoeck 2009; Ceccarelli et al. 2017; van 't Hoff et al. 2018; Lee et al. 2019; Jørgensen et al. 2020; Ceccarelli et al. 2022). Improvements in observational techniques and the sensitivity of instruments allow the chemistry of FUors and FUor-like objects to be studied in a new way, covering different frequency regimes (e.g., L1551 IRS5, Fridlund et al. 2002; Bianchi et al. 2020; Mercimek et al. 2022; Andreu et al. 2023; Marchand et al. 2024) and providing small scale views of the inner regions around these objects. Among the most noteworthy results from interferometric observations is the direct evidence of the outburst affecting the location of the water snow-line, shifting it from a typical few au to  $\sim 40\text{--}120$  au observed in the FUor V883 Ori (see Cieza et al. 2016; van 't Hoff et al. 2018; Leemker et al. 2021, and references therein). Observational studies of young eruptive stars in the (sub)millimeter regime targeting both molecular line emission and dust continuum radiation provide more in-depth views of the small-scale structures and kinematics of the disk, and the envelope surrounding these objects: transitions of  $^{12}\text{CO}$  and its rarer isotopic species  $^{13}\text{CO}$  and  $\text{C}^{18}\text{O}$  can be used to detect low- and high-density circumstellar material (e.g., Kóspál 2011; Kóspál et al. 2016, 2017b; Fehér et al. 2017; Cruz-Sáenz de Miera et al. 2023).  $\text{HCO}^+$  and  $\text{HCN}$  emission can trace cavity walls, while  $\text{SiO}$  and  $\text{SO}$  trace the shocked material in outflows (Hogerheijde et al. 1999), and finally, the line wings of  $^{12}\text{CO}$  emission trace the outflow itself (Evans et al. 1994).

Despite the growing number of observational studies in the millimeter regime including FUors and FUor-like objects (e.g., McMudroch et al. 1995; Fridlund et al. 2002; White et al. 2006; Fehér et al. 2017; Lee et al. 2019; Bianchi et al. 2020; Wendeborn et al. 2020; Mercimek et al. 2022; Ruíz-Rodríguez et al. 2022; Lee et al. 2024) and model predictions on molecules as outburst tracers in eruptive systems (Visser et al. 2015; Rab et al. 2017; Molyarova et al. 2018; Zwicky et al. 2024), wide-band spectral line surveys at (sub)mm wavelengths of more evolved FUors do not yet exist. The lack of studies could be (primarily) due to the distances of many of these sources, highlighted by Audard et al. (2014) and revised recently by Szabó et al. (2023a,b). Broad frequency coverage is needed to cover multiple transitions

of a given species, which is crucial to determine the physical properties of the gas using population diagrams (e.g., Goldsmith & Langer 1999).

Historically FUors, especially classical prominent examples of these stars, have been well-studied at optical and near-infrared wavelengths. This resulted in comprehensive analyses that are utilised to identify and characterise new members of the class (e.g., Herbig 1977; Herbig et al. 2003; Clarke et al. 2005; Connelley & Reipurth 2018; Hillenbrand et al. 2018; Szegedi-Elek et al. 2020; Szabó et al. 2021; Nagy et al. 2022; Szabó et al. 2022; Nagy et al. 2023). Millimeter wavelength observations of spectral lines and modeling have addressed their molecular content (e.g., Rab et al. 2017; Molyarova et al. 2018; Zwicky et al. 2024). Eruptive stars appear to be still close to their natal cores, whose chemistry can be investigated well through (sub)mm and radio wavelength observations (e.g., Szabó et al. 2023a,b, and references therein), which indicate the presence of high concentrations of dense material in the vicinity of the surveyed protostars. A line survey covering wide frequency regimes, aiming to provide an in-depth view of the molecular inventory of the environment of an FUor can motivate interferometric studies, which may allow further study of the outburst effects on the chemical composition of the stars' close environment.

This paper focuses on V1057 Cyg, a classical FUor in the Class II evolutionary phase (e.g., Herbig 1977; Herbig et al. 2003), the second FUor discovered. At a distance of  $897^{+19}_{-20}$  pc (Bailer-Jones et al. 2018a,b), V1057 Cyg has the highest peak accretion rate among FUors (Szabó et al. 2021) measured to date. The source went into outburst in 1969–1970, brightening by  $\sim 6$  magnitudes in the  $V$ -band (Welin 1971a,b). The only pre-outburst spectrum shows properties of a T Tauri star (TTS, Herbig 1977, 2009). The source displays variable and high-velocity wind features of P Cygni profiles blueshifted by up to  $100 - 300 \text{ km s}^{-1}$  and recently jet tracers were detected, usually rare in FUors, but more common in classical T Tauri stars (Magakian et al. 2013; Takagi et al. 2018; Kóspál et al. 2020; Park et al. 2020; Szabó et al. 2021). V1057 Cyg has exhibited multiple extraordinary flares in the 1720 MHz OH maser transition, remaining the only eruptive star known to show this phenomenon (Lo & Bechis 1973, 1974; Winnberg et al. 1981). We note that although the optical and near-infrared properties of V1057 Cyg suggest a more evolved evolutionary state (e.g., Herbig et al. 2003; Szabó et al. 2021), observations conducted in the millimeter regime have suggested a younger, Class I state (e.g., significant contribution of the envelope, Fehér et al. 2017; Calahan et al. 2024a).

In this paper, we present the results of a wideband spectral line survey of V1057 Cyg complemented by on-the-fly maps of emission from selected molecules. The line survey was conducted with the IRAM 30-m telescope and has an almost continuous coverage from  $\sim 72$  GHz ( $\sim 4.1$  mm) to  $\sim 263$  GHz ( $\sim 1.1$  mm). Other selected frequencies, around 219 GHz – 227 GHz ( $\sim 1.3$  mm), 291 GHz ( $\sim 1.0$  mm), and 344 GHz ( $\sim 0.8$  mm), were observed with the APEX 12-m telescope. Together, this dataset provides an in-depth view of the molecular composition of this young eruptive star's environment. The paper is laid out as follows. In Sect. 2 we describe the observations as well as the data reduction. In Sect. 3 we present the results and analysis of the data, while in Sect. 4 we compare our findings with results reported in the literature. Finally, in Sect. 5 we summarise the most important findings of this study.

## 2. Observations and data reduction

To acquire our main spectral line survey data of V1057 Cyg we observed the star's position,  $(\alpha, \delta)_{J2000} = 20^{\text{h}}58^{\text{m}}53^{\text{s}}73, +44^{\circ}15'28''4$ , with the IRAM 30-m telescope, operated by the Instituto de Radioastronomía Milimétrica (IRAM) on Pico Veleta in the Spanish Sierra Nevada. The observations (project id: 060-23, PI: Menten) took place from 2021 August 4 to 6, with a total observing time of 35.5 hours. We used the Eight Mixer Receiver<sup>1</sup> (EMIR, Carter et al. 2012) in the E0, E1 and E2 bands, with the fast Fourier transform spectrometers (FFTSs), providing an instantaneous bandwidth of 16 GHz and a spectral resolution of  $\sim 200$  kHz. The survey was conducted in the position-switching mode with a reference position at the relative equatorial offset ( $-600''$ ,  $600''$ ). In addition, mapping was conducted using on-the-fly (otf) mode, centred on the position of V1057 Cyg with a reference position at ( $300''$ ,  $300''$ ). NGC 7027 and K3-50A were used to obtain pointing and focus corrections regularly during each observing session. The main parameters of the 30-m observations are summarised in Table 1. The main beam efficiencies were computed using the Ruze formula, with parameters taken from the IRAM webpage<sup>2</sup>. The data were reduced using the GILDAS/CLASS software developed by IRAM (Pety 2005). Platforming effects, materialising as intensity offsets in the spectra, were identified and corrected by subtracting first order baselines in each subband. In addition, we excluded scans, where careful inspection revealed remaining platforming, which generally stemmed from problems in the outer basebands, or any other issues (see also Fig. 1, 2, and A.1 to A.9).

In addition to the IRAM 30-m observations we conducted observations with the Atacama Pathfinder EXperiment (APEX) 12-m submillimeter telescope at selected frequencies centered around 227, 291, and 344 GHz (project ids: M9530C\_107, M9515A\_108, M9523C\_109; PI: Menten). APEX is located on a 5100 m altitude site in the Llano de Chajnantor, Chile (Güsten et al. 2006). The APEX data were obtained using several instruments, summarised here in chronological order of their use (see also Table 2). We used the dual-sideband, dual-polarization receiver nFLASH230<sup>3</sup> with the Fast Fourier Transform Spectrometer (FFTS, Klein et al. 2006) backend, providing a bandwidth of 32 GHz and a spectral resolution of 61 kHz, covering frequencies between  $\sim 213$  and  $\sim 245$  GHz. The observations were carried out on 2021 July 20, 21, and 31 with a total observing time of  $\sim 5.5$  hours. For the July 20 and 21 observations the wobbler switching mode was used with a single pointing toward the position of the source and a wobbler throw of  $200''$  in azimuth, and for the July 31 observation mapping was conducted with a reference position at the relative equatorial offset ( $6000''$ ,  $4000''$ ). We also used LAsMA<sup>4</sup>, a 7-pixel, dual-sideband, single-polarization, heterodyne receiver, consisting of a hexagonal array of six pixels surrounding a central pixel. The backend consisted of Fast Fourier Transform Spectrometers (FFTSs) covering an intermediate frequency (IF) bandwidth of 4 – 8 GHz. The observing time with LAsMA was  $\sim 8.5$  hours. The LAsMA observations were conducted using the on-the-fly mapping mode with reference position at ( $400''$ ,  $400''$ ). Finally, we used the dual-sideband, dual-polarization receiver SEPIA345<sup>5</sup>. The upper and lower sidebands each cover the IF range 4 – 12 GHz, giving a total of 32 GHz IF bandwidth, with each sideband recorded

by two FFTS units. The observations were conducted with the position-switching mode with a reference position at ( $300''$ ,  $300''$ ). The observing time was  $\sim 1$  hour with SEPIA. The total observing time with APEX was  $\sim 15$  hours. For all APEX observations, the antenna temperature,  $T_A^*$ , was converted to main-beam temperature,  $T_{MB}$ , using the relationship  $T_{MB} = T_A^* \eta_f / \eta_{mb}$  where  $\eta_f$  and  $\eta_{mb}$  are the forward and main-beam efficiencies, respectively, from the APEX website<sup>6</sup>. The main parameters of the observations are listed in Table 2. The data obtained with APEX were also reduced using the GILDAS/CLASS software (see Figs. A.10–A.13).

## 3. Results and analysis

### 3.1. Line detection and identification

Figure 1 presents the complete spectrum obtained towards V1057 Cyg with the IRAM 30-m telescope, with frequencies of prominent lines marked with vertical lines. Line identifications were based on spectroscopic data from the Cologne Database for Molecular Spectroscopy<sup>7</sup> (CDMS, Müller et al. 2001, 2005) and the Jet Propulsion Laboratory catalog<sup>8</sup> (JPL, Pickett et al. 1998). A line is considered detected if its peak intensity is  $\geq 3\sigma$ , where  $\sigma$  is the rms noise level measured in the portion of the spectrum surrounding the candidate line. We only report lines of molecules with at least 2 detected transitions within the coverage of our line survey. In general, the detected lines are relatively narrow ( $< 2.5$  km s<sup>-1</sup>), and well isolated, thus their identification is straightforward compared to line-rich sources such as hot cores or hot corinos (in high-mass or low-mass star-forming regions; e.g., Belloche et al. 2013; Bianchi et al. 2020; Busch et al. 2024). Figure 2 shows examples of the detected line profiles for several molecules observed with the 30-m telescope. These examples illustrate the identification of molecules with specific transitions (e.g., DCO<sup>+</sup>), hyperfine structure components (e.g., CN), multiple transitions within a narrow frequency range (e.g., CH<sub>3</sub>OH), and the presence of broad wings indicating outflow activity (e.g., <sup>13</sup>CO). The complete list of identified lines is given in Table A.1 with upper energy levels, Einstein coefficients, and the parameters derived from Gaussian fits (discussed in Sect. 3.2), while each detected line is displayed in a narrow frequency window in Figs. A.1–A.9. There are several cases where the data suggest potential detections of molecules, however, these identifications remain uncertain due to low signal-to-noise ratios (with candidate lines detected  $< 3\sigma$ ) or because they are based on a single, weakly detected transition (below  $< 3\sigma$ ). These occurrences are not included in the final line identification and fit results in Table A.1, but are instead marked with green labels in Figs. A.1–A.9 (e.g., some transitions of H<sub>2</sub>CO, H<sub>2</sub>CN, H<sub>3</sub>CN, CH<sub>3</sub>OH in Fig. A.7). The list of identified lines from the APEX observations is given in Table A.2 and the detected lines are displayed in Figs. A.10–A.13.

We detect emission of molecules ranging from simple neutral molecular species to COMs. Identified species are listed in Table 3, with the molecules organised from the simplest to the most complex. In total, 35 molecular species are detected (including isotopologues) in the spectrum of V1057 Cyg. We detect C-, N-, O-, S-bearing molecules (e.g., CO, CN, CS, CCS, HCN, HNC, H<sub>2</sub>CO, H<sub>2</sub>CS), deuterated species (e.g., DCN, DNC), molecular ions (e.g., HCO<sup>+</sup>, HCS<sup>+</sup>), carbon-chain molecules (e.g., C<sub>2</sub>H,

<sup>1</sup> <https://publicwiki.iram.es/EmirforAstronomers#Overview>

<sup>2</sup> <https://publicwiki.iram.es/Iram30mEfficiencies>

<sup>3</sup> <https://www.apex-telescope.org/ns/nflash/>

<sup>4</sup> <https://www.mpifr-bonn.mpg.de/5278286/lasma>

<sup>5</sup> <https://www.apex-telescope.org/ns/instruments/sepia/>

<sup>6</sup> <https://www.apex-telescope.org/telescope/efficiency/>

<sup>7</sup> <https://cdms.astro.uni-koeln.de>

<sup>8</sup> <https://spec.jpl.nasa.gov>

Table 1: Information on the IRAM 30-m observations conducted with EMIR.

Date yyyy-mm-dd	Mode	Band	Tuning (GHz)	Frequency range (LSB, USB) (GHz)	Beam ( $''$ )	Measured rms noise level <sup>(*)</sup>				Size of otf map ( $''$ )
						LO (mK)	LI (mK)	UI (mK)	UO (mK)	
2021-08-04	onOff	E0	73	72 – 78.5, 86.4 – 94.1	34.4 – 26.7	12.5	8	5.5	11.2	–
2021-08-04	onOff	E0	80	77.7 – 85.5, 93.2 – 101.1	32.2 – 22.8	5.1	3.9	4.5	4.7	–
2021-08-06	otf	E0	90	87.7 – 95.5, 103.3 – 111.1	28.2 – 22.6	11.2	10.7	12.3	14.7	300'' $\times$ 300'' 315'' $\times$ 315''
2021-08-04	onOff	E0	94	92.7 – 99.8, 107.7 – 115.5	27.3 – 21.6	4.5	3.5	4.4	6.4	–
2021-08-05	onOff	E1	133	130.7 – 138.5, 146.3 – 154.1	19.1 – 16.31	7.6	5.8	9.3	12	–
2021-08-05	onOff	E1	141	138.7 – 146.5, 154.4 – 162.1	18.1 – 15.51	7.5	5.9	10	9.5	–
2021-08-06	onOff	E2	202	199.7 – 207.5, 215.4 – 223.1	12.5 – 11.2	19.3	36.1	37.3	39.2	–
2021-08-06	onOff	E2	210	207.7 – 215.5, 223.4 – 231.1	12.1 – 10.8	46.5	43.9	43	45.9	–
2021-08-06	onOff	E2	234 <sup>(a)</sup>	231.7 – 239.5, 247.4 – 255.1	10.8 – 9.8	37.8	41.6	54	74.8	–
2021-08-06	onOff	E2	242	239.7 – 247.5, 255.4 – 263.1	10.4 – 9.5	52.3	52.4	64.8	67.8	–

**Notes.** <sup>(\*)</sup> The rms noise levels were measured separately for the lower outer (LO), lower inner (LI), upper inner (UI), and upper outer (UO) bands of the lower and upper side bands. <sup>(a)</sup> The 234 GHz tuning observations are not presented in this paper due to low atmospheric transmission in the covered frequency range.

Table 2: Information on the APEX 12-m observations.

Date yyyy-mm-dd	Receiver	Mode	Band	Tuning (GHz)	Frequency range (GHz)	Beam ( $''$ )	Measured rms noise level				Size of otf ( $''$ )
							LO (mK)	LI (mK)	UI (mK)	UO (mK)	
2021-07-20	nFLASH	onOff	nFLASH230	219.2	213.2 – 221.1, 229.3 – 237.2	29.5 – 26.5	20.3	38.5	21	122.5	–
2021-07-21	nFLASH	onOff	nFLASH230	227.2	221.1 – 229, 237.3 – 245.2	28.4 – 25.6	19.7	67.9	20.2	67.8	–
2021-07-31	nFLASH	otf	nFLASH230	227.2	213.2 – 221.1, 229.3 – 237.2	28.4 – 25.6	101	350	138	–*	600'' $\times$ 600''
2021-11-19	LAsMA	otf	LAsMA345	344.2	342.2 – 346.3, 354.2 – 358.2	18.3 – 17.5	30.4 <sup>(a)</sup>		59.3 <sup>(b)</sup>		120'' $\times$ 120''
2021-11-20	LAsMA	otf	LAsMA345	344.2	342.2 – 346.3, 354.2 – 358.2	18.3 – 17.5	31.1 <sup>(a)</sup>		105.1 <sup>(b)</sup>		120'' $\times$ 120''
2022-05-28	SEPIA	onOff	SEPIA345	291.0	272.9 – 280.8, 289.2 – 297	23.0 – 21.1	69.9	29.5	38	41.5	–

**Notes.** <sup>(\*)</sup> Due to high noise level and deep atmospheric lines the rms of the UO cannot be measured accurately. <sup>(a)</sup> Measured rms noise level for the whole LSB. <sup>(b)</sup> Measured rms noise level for the whole USB.

HC<sub>3</sub>N), a cyclic molecule (e.g., c-C<sub>3</sub>H<sub>2</sub>), COMs (e.g., CH<sub>3</sub>OH), and in many cases some of their isotopologues (see Table A.1).

The spectral energy distribution (SED) of V1057 Cyg implies a flared disk and envelope geometry (e.g., [Kenyon & Hartmann 1991](#)), while an envelope with an estimated size of 7000 au was confirmed from Spitzer/IRS observations ([Green et al. 2006](#)), and later 50–670  $\mu$ m far infrared/submillimeter wavelength imaging with *Herschel* indicated a reservoir of cold dust ([Green et al. 2013](#)). From <sup>13</sup>CO observations using the Plateau de Bure Interferometer (with a beam of 2.7'' $\times$ 2.2''), [Fehér et al. \(2017\)](#) reported a rotating envelope around V1057 Cyg, with a radius of 5'' (3000 au). Thus it is likely that our single-dish data, with a beam size larger than 9'', corresponding to  $\sim$ 8100 au at the 897 pc distance to the target, traces emission both from the disk and the envelope around the source. For instance, CO and its isotopologues likely trace the disk and outflow, while CS (2–1), HCN (1–0), and the hyperfine structure components of CN (2–1) and C<sub>2</sub>H (1–0) could sample the cold gas closer to the midplane (seen in T Tauri stars, e.g., [Dutrey et al. 2014](#)). We also detected other dense gas tracers, such as CS, CCS, HCO<sup>+</sup>, including their isotopologues <sup>13</sup>CS, C<sup>33</sup>S, C<sup>34</sup>S, and H<sup>13</sup>CO<sup>+</sup>, as well as N<sub>2</sub>H<sup>+</sup> (e.g., [Shirley 2015](#); [Yamamoto 2017](#), and references therein).

For most molecular species, several transitions with different upper-level energies are detected, which allows a more detailed analysis including simple radiative transfer modelling and the construction of population diagrams, presented in Sects. 3.4 and 3.5, respectively.

Table 3: Overview of molecules and isotopic species detected detected towards V1057 Cyg in this survey.

<i>Simple neutral molecules:</i> CN, <sup>13</sup> CN, CO, <sup>13</sup> CO, C <sup>17</sup> O, C <sup>18</sup> O, SO, CS, <sup>13</sup> CS, C <sup>33</sup> S, C <sup>34</sup> S, HCN, HNC, H <sub>2</sub> CO, H <sub>2</sub> <sup>13</sup> CO, H <sub>2</sub> CS
<i>Deuterated species:</i> CCD, DCN, DCO <sup>+</sup> , DNC, N <sub>2</sub> D <sup>+</sup> , HDCO
<i>Molecular ions:</i> HCO <sup>+</sup> , H <sup>13</sup> CO <sup>+</sup> , HCS <sup>+</sup> , N <sub>2</sub> H <sup>+</sup>
<i>Carbon chain molecules:</i> C <sub>2</sub> H, CCS, C <sub>4</sub> H, CH <sub>3</sub> CCH, HC <sub>3</sub> N
<i>Cyclic molecules:</i> c-C <sub>3</sub> H <sub>2</sub>
<i>Complex organic molecules:</i> CH <sub>3</sub> OH, CH <sub>3</sub> CN
<i>Other molecules:</i> HNCO

### 3.2. Line profiles, LSR velocities, and line widths

Based on single-dish observations, it can be challenging to distinguish emission from foreground/background clouds and from different physical structures within a source (e.g., disk, envelope) unless these components have different velocities. In this survey, we only detect molecules with similar velocities, suggesting that the observed line emission is associated with V1057 Cyg and its environment.



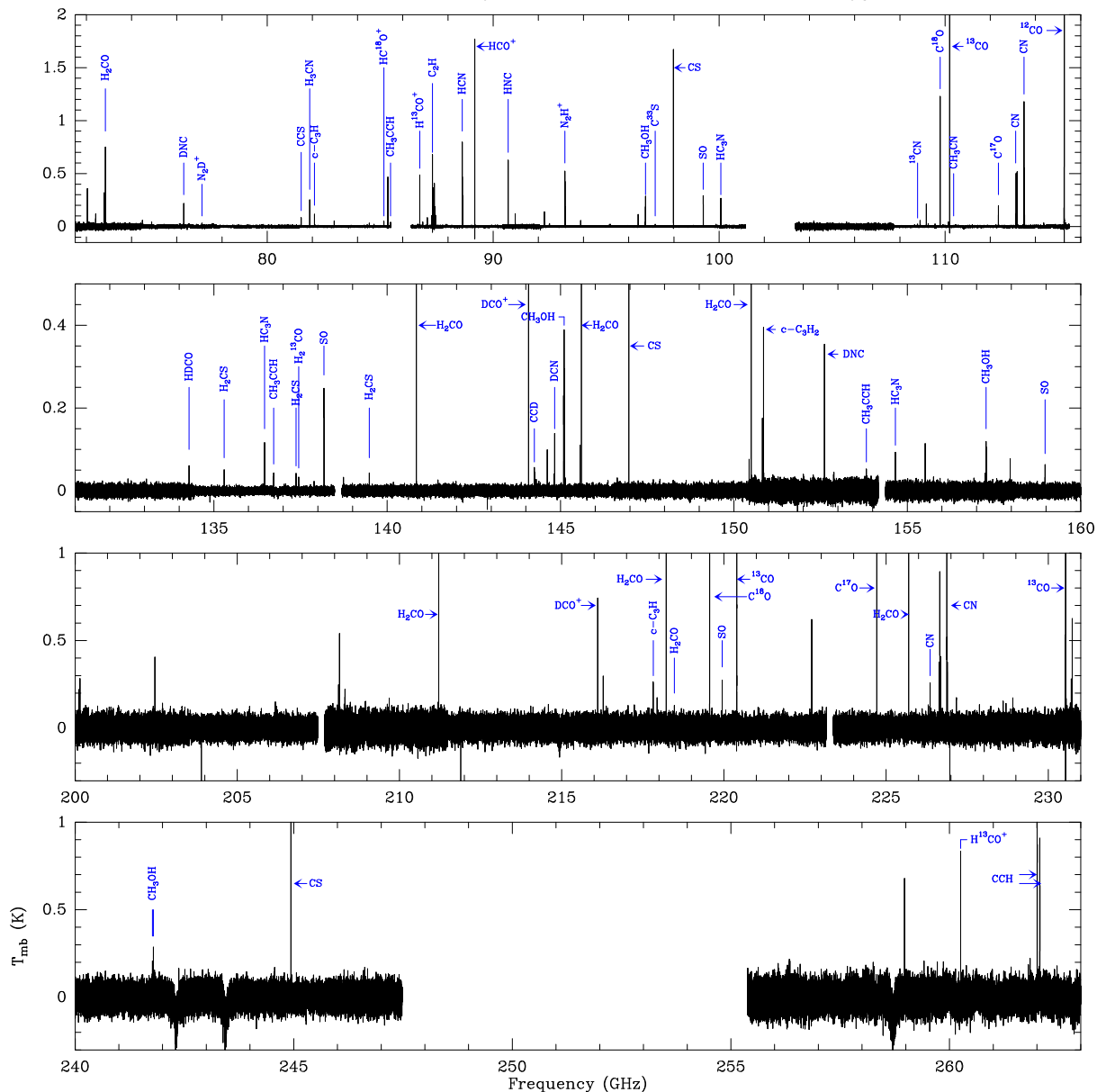


Fig. 1: Complete spectrum of V1057 Cyg obtained with the IRAM 30-m telescope, with selected lines labelled with the name of the molecular species. The complete list of identified lines is provided in Table A.1 and zoom views of all lines are displayed in Fig. 2 and Figs. A.1 – A.9. The deep absorption features around 242–244 GHz and 258–259 GHz represent residual atmospheric absorption.

Most of the detected lines show narrow single-peaked profiles that can be fitted by a single Gaussian. In the case of outflow tracers (e.g.,  $^{13}\text{CO}$ ) the line profiles are also single-peaked (except  $^{12}\text{CO}$ , see below), but show broader wings, suggesting outflow activity. For the spectrum at the source position, each line profile was fitted with a single Gaussian component using the built-in function in CLASS, and the results are presented in Tables A.1 and A.2. The Gaussian fitting method does not yield good results for the  $^{12}\text{CO}$  transitions because they show self-absorption, suggesting that these lines are optically thick (see examples for other FUors in Evans et al. 1994; Kóspál et al. 2017a; Kóspál 2011; Cruz-Sáenz de Miera et al. 2023). Therefore, these lines are only reported as detected in Tables A.1 and A.2, while Gaussian fit results are not presented. The LSR velocities obtained from the Gaussian fits range from 2.45 to 4.80  $\text{km s}^{-1}$  for the 30-m, and from 3.95 to 4.46  $\text{km s}^{-1}$  for the APEX data. Comparing to single-dish and interferometric observations

from the past decade, we find that the previously reported velocities of, for example,  $^{13}\text{CO}$  (1–0) (4.6 and 4.05  $\text{km s}^{-1}$ , Kóspál 2011; Fehér et al. 2017),  $\text{C}^{18}\text{O}$  (1–0) (4.10  $\text{km s}^{-1}$ , Kóspál 2011), and  $\text{NH}_3$  (1,1) (4.35  $\text{km s}^{-1}$ , Szabó et al. 2023a) are generally within  $\sim 0.5 \text{ km s}^{-1}$  of the  $v_{\text{LSR}}$  values derived in this study, further indicating that the molecular species detected in our survey are associated with V1057 Cyg and its environment. Notably, we find that the measured velocities of dense gas tracers such as CS, CCS,  $\text{H}^{13}\text{CO}^+$ ,  $\text{N}_2\text{H}^+$  and  $\text{HC}_3\text{N}$  coincide within  $\sim 0.3 \text{ km s}^{-1}$  (within the uncertainties of the Gaussian fits) with the systemic velocity of V1057 Cyg derived from the most recent ammonia observations ( $4.35 \pm 0.02 \text{ km s}^{-1}$ , Szabó et al. 2023a).

From the Gaussian fits, we find FWHM line widths between 0.67 and 3.43  $\text{km s}^{-1}$  for the 30-m, and from 0.71 to 1.78  $\text{km s}^{-1}$  for the APEX data. In general, lines that show wings, indicating outflow activity, have FWHM line widths broader than the other species (e.g.,  $^{12}\text{CO}$  and its isotopologues). The line widths of

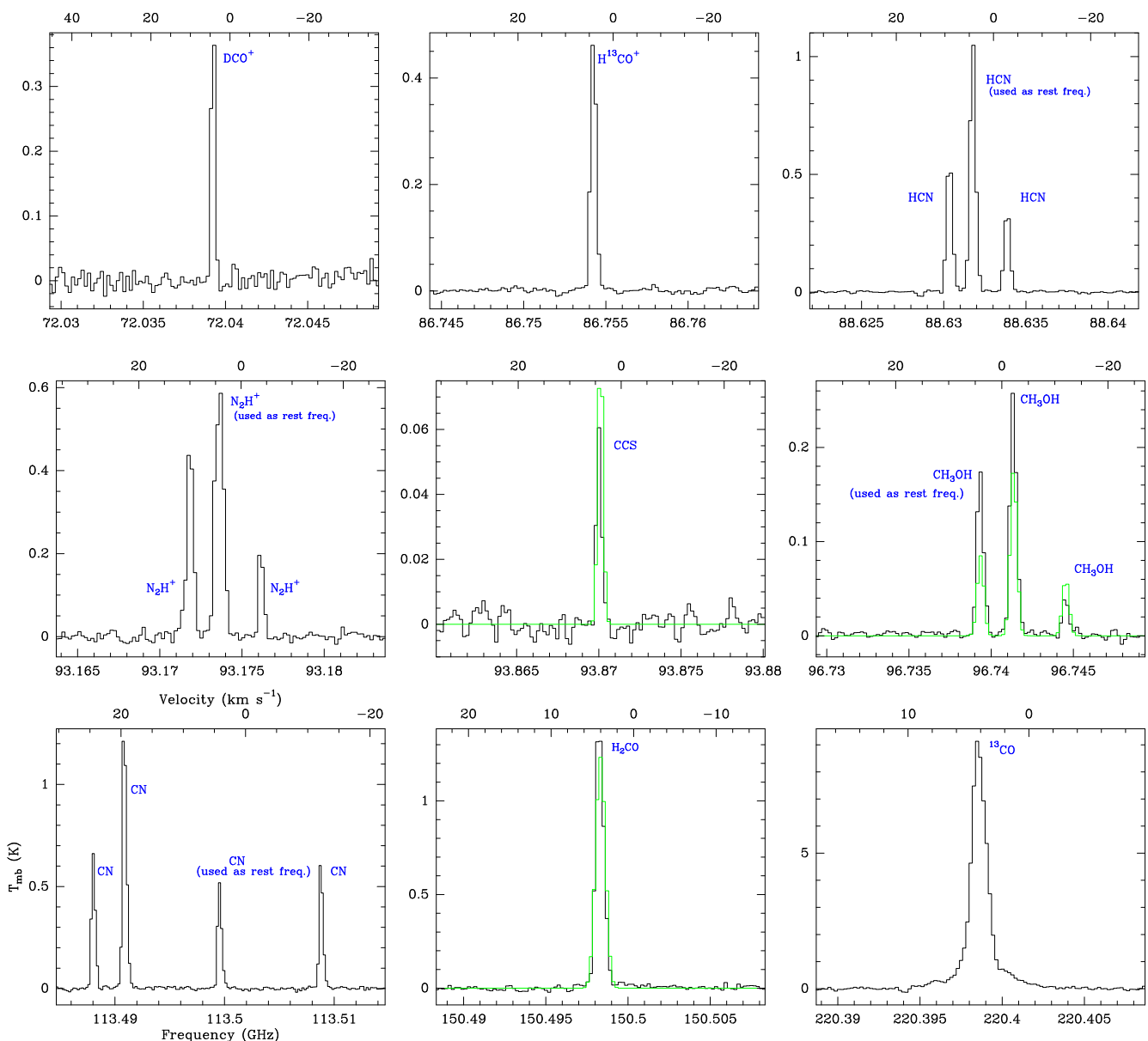


Fig. 2: Selection of lines detected with the IRAM 30-m telescope, labelled with the molecular species name in blue; the other lines are shown in Figs. A.1–A.9. LTE synthetic spectra are overlaid in green for selected species (see Sects. 3.4 and 3.5). In each panel, the bottom and top axes are labelled in frequency and velocity, respectively.

more than  $>50\%$  of the fitted lines cluster around  $1.3\text{--}1.5\text{ km s}^{-1}$  for mainly the transitions of  $\text{CH}_3\text{OH}$ ,  $\text{HC}_3\text{N}$ , and  $\text{H}_2\text{CO}$ . Narrower widths are mainly found for CN and  $c\text{-C}_3\text{H}_2$  lines, the former clustered around  $1.1\text{ km s}^{-1}$  and the latter around  $0.9\text{--}1\text{ km s}^{-1}$ .

We note that the transition of methanol ( $\text{CH}_3\text{OH}$ ) at  $84.5\text{ GHz}$  is a well-known Class I maser line (e.g., [Batra & Menten 1988](#); [Breen et al. 2019](#), and references therein). However, the line emission detected towards V1057 Cyg does not show clear maser characteristics (such as strong, and narrow features in comparison to other transitions), thus not suggesting maser activity. The well-known Class I  $\text{CH}_3\text{OH}$  maser line at  $95.1\text{ GHz}$  ([Plambeck & Menten 1990](#); [Chen et al. 2011](#); [Yang et al. 2023](#)) was not detected in our survey, which we discuss in Sect. 3.5.

### 3.3. Line mapping

Figures 3 and 4 present integrated intensity maps for lines mapped in the off mode with the IRAM 30-m and APEX 12-m telescopes, respectively. In most cases (except  $^{13}\text{CO}$  1–0 and 2–1, see Figs. 3i and 4b), the molecular line emission does not peak on V1057 Cyg itself. The HCN (1–0) HNC (1–0),  $\text{HC}_3\text{N}$  (10–9),  $\text{HCO}^+$  (1–0), and  $\text{N}_2\text{H}^+$  (1–0) maps show a primary concentration of emission offset from V1057 Cyg towards the north, while a secondary peak is distributed towards the southwest, connected with a ridge that traces a pc-scale filamentary structure (Fig. 3c,d,f,g,h). The northern peak is offset by approximately  $14.7''$  ( $\sim 0.06\text{ pc}$ ) to the north, while the southern peak is located approximately  $1.8'$  ( $\sim 0.46\text{ pc}$ ) to the southwest of V1057 Cyg. The offset of the northern concentration relative to V1057 Cyg corresponds to only half a beam width in the 3 mm maps, but given the high signal-to-noise ratio of most maps, it is

significant. It is unlikely the result of an optical depth effect because  $^{13}\text{CO}$  (1–0) does peak towards the source. Moreover, the offset is larger than the pointing error. Furthermore, this peak is also visible in the dust-based  $\text{H}_2$  column density map (Szabó et al. 2023a). The larger-scale ridge structure is well traced by the 1–0 and 2–1 transitions of  $^{13}\text{CO}$  and  $\text{C}^{18}\text{O}$  (see Figs. 3i,j and 4b,c). The ridge towards the southwest appears fainter compared to the northern peak seen in the maps of the 1–0 transitions of  $\text{HCN}$ ,  $\text{HCO}^+$ , and  $\text{N}_2\text{H}^+$ . Notably, the extent of the emission from some transitions (e.g.,  $\text{HC}_3\text{N}$  10–9,  $\text{HNC}$  1–0) to the southwest seems comparable in size and intensity to that of the northern peak. The integrated intensity maps of  $\text{CCS}$  (7–6),  $\text{H}_2\text{CS}$  (3–2), and  $\text{HC}_3\text{N}$  (12–11) have lower signal-to-noise ratios but appear to trace the same extensions toward the north and southwest.

The molecular outflow of V1057 Cyg was first reported by Evans et al. (1994) on the basis of the strong blueshifted wing emission detected in their  $^{12}\text{CO}$  3–2 spectrum obtained with the Caltech Submillimeter Observatory 10.4 m telescope (CSO). These authors also mentioned the existence of maps towards this source as a private communication from S. McMurdock but we could not find any publication reporting them. The APEX spectrum has a similar line profile as the CSO spectrum, with a slightly more pronounced self-absorption, however, our more sensitive spectrum reveals the redshifted wing for the first time. The APEX map of the  $^{12}\text{CO}$  3–2 emission, presented in Fig. 5, reveals a bipolar outflow that appears to originate from V1057 Cyg. The outflow appears to be more collimated on the redshifted side, with discrete peaks to the south of the source position. Fig. 6 shows a  $^{12}\text{CO}$  (3–2) position-velocity ( $p$ - $v$ ) diagram taken along the cut shown in Fig. 5. The  $p$ - $v$  diagram shows several peaks (labelled R1, R2, and B1; R for red and B for blue), which are more prominent in the redshifted emission. The highest velocity extensions are revealed by the first contour close to R1, which may mark an episodic ejection event (Plunkett et al. 2015). Peak R1 appears close to the systemic velocity of the source, while peak R2 is located around  $5 \text{ km s}^{-1}$ . The fainter blueshifted peak, B1, appears at a velocity around  $1 \text{ km s}^{-1}$ . The  $p$ - $v$  diagram also shows weak "fingers" (indicated by white arrows) revealed by the lowest contours of the  $^{12}\text{CO}$  emission. These results are further discussed in Sect. 4.2.

### 3.4. Radiative transfer modelling

The observed spectra were modeled using Weeds (a GILDAS/CLASS extension for the analysis of millimeter and submillimeter data, Maret et al. 2011) to create synthetic spectra with the assumption of local thermodynamic equilibrium (LTE). The spectroscopic information required for the synthetic spectra was taken from the CDMS database (Müller et al. 2005; Endres et al. 2016). Multiple transitions are detected from molecules such as methanol ( $\text{CH}_3\text{OH}$ ), formaldehyde ( $\text{H}_2\text{CO}$ ), cyclopropenylidene ( $c\text{-C}_3\text{H}_2$ ), carbon monosulfide (CS), thioethenylidene (CCS), cyanoacetylene ( $\text{HC}_3\text{N}$ ), and thioformaldehyde ( $\text{H}_2\text{CS}$ ) (see Tables 4 and A.1). These species were chosen because several of their lines show significant emission (i.e.,  $> 3\sigma$ ) and their profiles do not show indication of outflow (i.e., extended wings, as seen in lines from  $^{12}\text{CO}$  and its isotopologues). Only transitions detected with the IRAM 30-m telescope with a signal-to-noise ratio higher than  $3\sigma$  were used for the following analysis. The radiative transfer model presented here, along with the population diagrams in Sect. 3.5, provides initial estimates of the temperatures and column

densities of V1057 Cyg and its surrounding environment as observed in the single-dish data.

The purpose of applying a Weeds model to the chosen molecules is to improve the line identification and to investigate whether the spectrum is well-represented by an LTE model. The radiative transfer is computed by accounting for the line optical depth and the angular resolution of the observations. Weeds requires five input parameters for each molecule: the size of the emitting region ( $\theta_s$ ) in arcseconds, column density ( $N_{\text{tot}}$ ), temperature ( $T_{\text{rot}}$ ), line width ( $\Delta v$  in  $\text{km s}^{-1}$ ), and velocity offset ( $v_{\text{off}}$ , with respect to the systemic velocity of the source). For each molecule, the line width was set to the average value of the line widths determined from the Gaussian fits of its detected transitions. The column density and rotational temperature were set by eye, and subsequently adjusted until the best-fit was achieved. The population diagrams described in Sect. 3.5 were used to optimise the temperature, emission size, and, in turn, the column density, of the Weeds models to reach the best fits possible.

We explored a range of source sizes between  $1.5''$  (e.g., Calahan et al. 2024b) and  $35''$  (larger than the largest beam size) and found the best fits with a source size of  $25''$  for  $\text{HC}_3\text{N}$  and  $30''$  for the rest of the molecular species. These results are consistent with the integrated intensity maps of the different species (see Fig. 3), and are further discussed in Sect. 3.5. Calahan et al. (2024b) detected methanol emission towards V1057 Cyg using the NOEMA interferometer, which remained unresolved. They derived the column density and temperature of methanol with a similar LTE analysis, assuming a size of  $1.5''$  (Calahan priv. comm.). Using the same parameters in our Weeds model of the single-dish data results in methanol lines that are much weaker than those detected with the 30-m telescope. The 218.44 GHz methanol line is detected in both the interferometric and the single-dish data. The peak intensity of this line is  $53 \text{ mJy/beam}$  in the NOEMA data (Calahan priv. comm.) and  $440 \text{ mJy/beam}$  in the IRAM 30-m telescope spectrum,  $\sim 8.3$  times higher. Since the  $\text{CH}_3\text{OH}$  emission in the NOEMA data was unresolved (Calahan et al. 2024b), this difference implies that the single-dish observations trace extended emission that is not detected by the interferometer. With the single-dish telescope, we are likely capturing several components blended together, including disk, envelope, and surrounding cloud emission.

The best-fit column densities from our LTE modeling are used to derive abundances relative to  $\text{H}_2$ . We derived values for the  $\text{H}_2$  column density by following the method used in Szabó et al. (2023a, and references therein). We used archival *Herschel* data at 160, 250, and  $350 \mu\text{m}$  to fit a spectral energy distribution (SED) to the data and derive  $\text{H}_2$  column densities at  $25''$  and  $30''$  resolution (corresponding to the sizes mentioned above) using the same method as used by Szabó et al. (2023a). However, unlike Szabó et al. (2023a), we did not use the  $500 \mu\text{m}$  data because of their relatively poor angular resolution ( $37''$ ). Based on the SED fit, we find  $\text{H}_2$  column densities of  $1.14 \times 10^{22} \text{ cm}^{-2}$  and  $1.21 \times 10^{22} \text{ cm}^{-2}$  at the angular resolution of  $30''$  and  $25''$ , respectively (beam centered on the optical stellar position), with typical uncertainties of about 10%. The derived column densities and abundances are further discussed in Sect. 3.5 and listed in Table 4. In a number of cases (especially for certain transitions of methanol) the LTE synthetic spectra do not match the observed spectra that well, whose excitation may deviate from LTE. Non-LTE modeling is beyond the scope of this work.

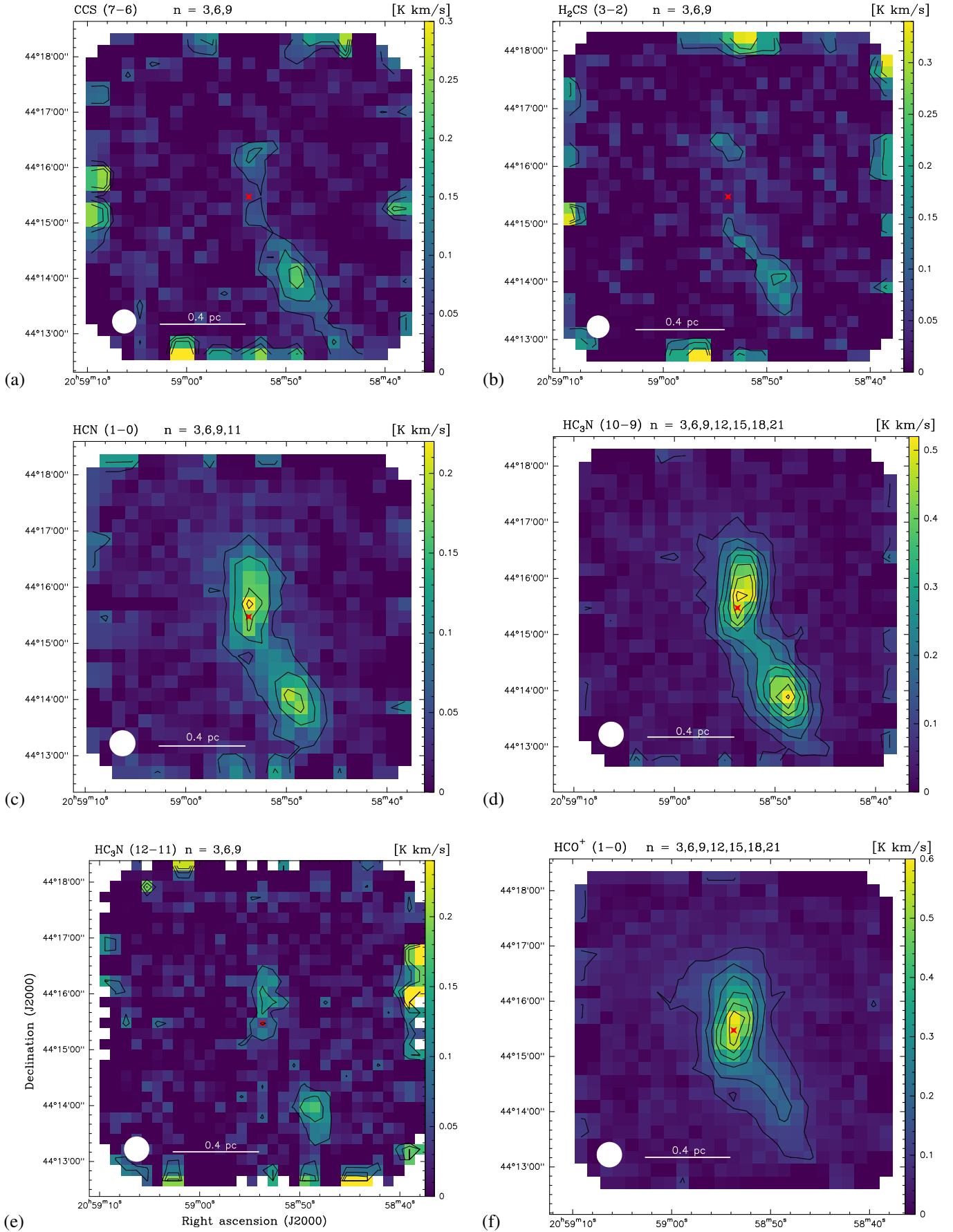


Fig. 3: Integrated intensity maps of molecular lines obtained with the IRAM 30-m telescope. The red cross marks the position of V1057 Cyg and the white circle shows the telescope beam size at the line frequency. The physical scale is presented near the beam size. Contour levels are  $n\sigma_{int}$  (multiples of the noise level in each map), with the corresponding values of  $n$  given above each panel.



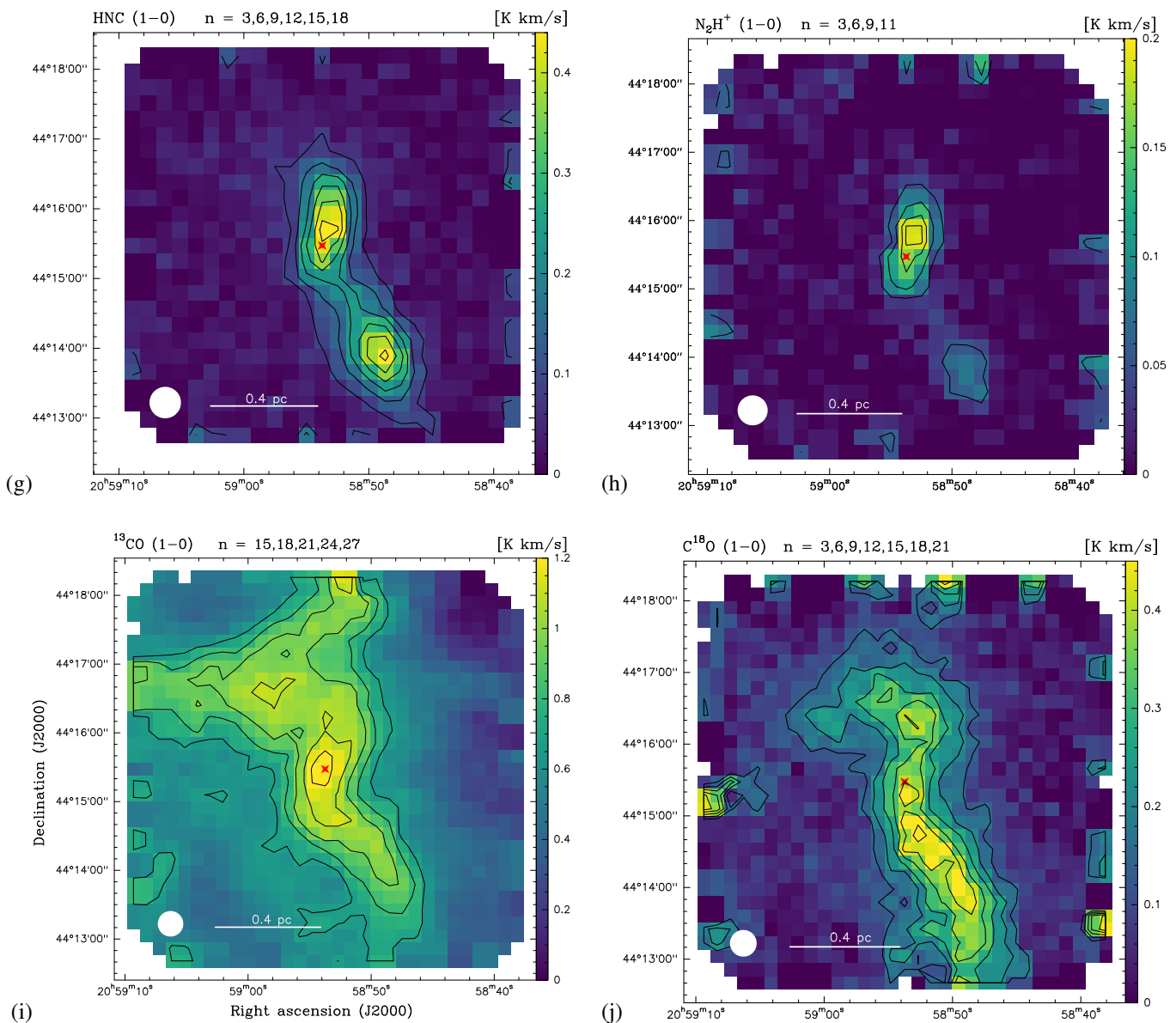


Fig. 3: Continued.

### 3.5. Population diagrams and abundances

The transitions used for the population diagrams are well isolated in the spectrum of V1057 Cyg, therefore it was not necessary to discard any transitions owing to contamination by other species (a potential issue in line-rich sources; e.g., [Belloche et al. 2009, 2016](#)). The population diagrams were constructed using the integrated intensities of the observed profiles, and are presented in Fig. 7, while the fit results are given in Table 4. The population diagrams presented in this paper account for beam dilution, using the sizes determined in Sect. 3.4, including the changing beam size through the frequency coverage. Additionally, the diagrams are also corrected for optical depth, using the opacity correction factor  $C_\tau = \frac{\tau}{1-e^{-\tau}}$  (see [Goldsmith & Langer 1999](#)) from the Weeds model.

In the case of methanol (Fig. 7a), we separated the *A*- and *E*-type transitions using two shades of green to test if there is a systematic difference, however, we found none. The population diagram is also a good way to see hints of maser activity of

known maser species. The methanol emission in the 84.5 GHz transition does not show deviation from the rest of the transitions in Fig. 7(a), so does not indicate maser activity. However, we note, that the best-fit model with Weeds underestimates the line strength. The other common maser transition at 95.1 GHz was not detected in this survey.

In all cases, a linear trend is present without significant departure from the linearity that could indicate the effect of optically thick emission or sub-thermal excitation (e.g., [Velilla Prieto et al. 2017](#)). The assumed emission size can affect the spread of data points in the population diagram due to the frequency-dependent beam size, while the opacities were found to be  $\ll 1$  for all transitions, and thus do not affect the shape of the diagrams. We checked emission from CH<sub>3</sub>OH, from which multiple lower-frequency transitions (below 120 GHz,  $\sim 3$  mm window) are detected, and we found that assuming emission sizes smaller than 30'' increases the spread of the data points. This leads to a larger gap between the low- and high-frequency transitions, which in turn compromises the fit to the data.

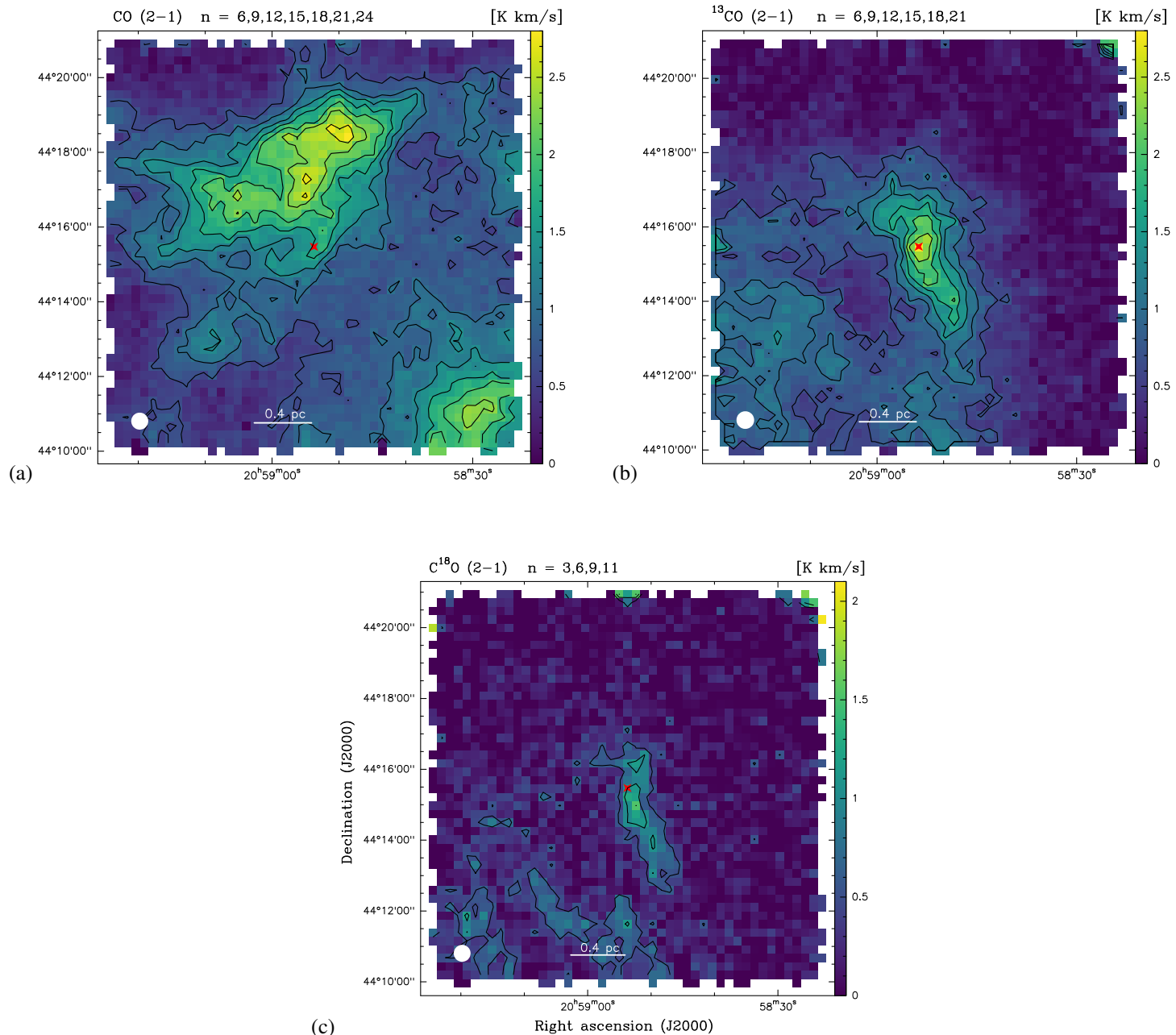


Fig. 4: Same as Fig. 3, but for the maps of (a)  $^{12}\text{CO}$ , (b)  $^{13}\text{CO}$ , and (c)  $\text{C}^{18}\text{O}$  (2–1) obtained with APEX.

From the population diagram method, we find column densities ranging from  $2.8 \times 10^{13} \text{ cm}^{-2}$  for  $\text{CH}_3\text{OH}$ , down to  $1.4 \times 10^{12} \text{ cm}^{-2}$  for  $\text{H}_2\text{CS}$ , and rotational temperatures ranging from 8.1 K to 14.8 K. The Weeds models were optimised on the basis of the population diagram results and the two methods agree within the errors of the population diagram method for both the column density and rotational temperature values.

## 4. Discussion

### 4.1. Large- and small-scale structures in the environment of V1057 Cyg

In Sect. 3.3 we presented the integrated intensity maps of several molecular species, in most cases tracing lower energy transitions (Figs. 3 and 4). Here, we discuss the different structures traced

in our single-dish observations in the environment of our target and compare our findings with those in the literature.

The observed molecular emission traces a ridge structure seen in most of the integrated intensity maps with two peaks offset from V1057 Cyg: one towards the north at  $\sim 14.7''$  and one towards the southwest at  $\sim 1.8'$ . The interferometric  $^{13}\text{CO}$  (1–0) data presented by Fehér et al. (2017) show a structure to the north of V1057 Cyg referred to as clump B with a similar offset to that seen in the single-dish data. Their maps show the close vicinity of V1057 Cyg and do not cover the southwestern extension. Extended  $850 \mu\text{m}$  emission distributed over large scales has been reported by Sandell & Weintraub (2001), who used the Submillimeter Common User Bolometer Array (SCUBA) on the James Clerk Maxwell Telescope. These authors found V1057 Cyg to be located in a narrow ridge, traced by the dust continuum emission, extending to the north and southwest of the star. Our single-dish data extend further to the southwest providing more information.

Table 4: Parameters of our best-fit LTE model and population diagram fit of methanol, formaldehyde, thioethenylidene, cyanoacetylene, thioformaldehyde, carbon monosulfide, and cyclopropenylidene.

Molecule	Parameters of the best-fit LTE model					Results of the population diagram method	
	Source size <sup>(a)</sup> ( $''$ )	$N_{\text{Weeds}}^{(b)}$ ( $\text{cm}^{-2}$ )	$T_{\text{rot}}^{(c)}$ (K)	$\Delta v^{(d)}$ ( $\text{km s}^{-1}$ )	$N_{\text{X}}/N_{\text{H}_2}^{(e)}$	$N_{\text{pop}}^{(f)}$ ( $\text{cm}^{-2}$ )	$T_{\text{rot}}^{(g)}$ (K)
CH <sub>3</sub> OH	30 $''$	$3.3 \times 10^{13}$	12.0	1.42	$2.8 \times 10^{-09}$	$2.8 \times 10^{13} \pm 1.0 \times 10^{13}$	$11.7 \pm 1.9$
H <sub>2</sub> CO	30 $''$	$2.0 \times 10^{13}$	9.7	1.27	$1.7 \times 10^{-09}$	$1.6 \times 10^{13} \pm 4.2 \times 10^{12}$	$10.6 \pm 1.3$
CCS	30 $''$	$3.0 \times 10^{12}$	9.4	1.14	$2.8 \times 10^{-10}$	$3.3 \times 10^{12} \pm 1.2 \times 10^{12}$	$8.1 \pm 0.8$
HC <sub>3</sub> N	25 $''$	$5.0 \times 10^{12}$	14.5	1.19	$3.5 \times 10^{-10}$	$4.2 \times 10^{12} \pm 5.7 \times 10^{11}$	$14.4 \pm 0.7$
H <sub>2</sub> CS	30 $''$	$1.5 \times 10^{12}$	14.0	1.29	$1.2 \times 10^{-10}$	$1.4 \times 10^{12} \pm 1.5 \times 10^{11}$	$14.8 \pm 9.5$
CS	30 $''$	$2.2 \times 10^{13}$	10.5	1.33	$1.9 \times 10^{-09}$	$1.7 \times 10^{13} \pm 5.4 \times 10^{12}$	$10.5 \pm 1.5$
c-C <sub>3</sub> H <sub>2</sub>	30 $''$	$6.0 \times 10^{12}$	9.0	1.09	$4.7 \times 10^{-10}$	$5.5 \times 10^{12} \pm 1.5 \times 10^{12}$	$8.6 \pm 0.7$

**Notes.** <sup>(a)</sup> Emission diameter (FWHM). <sup>(b)</sup> Column density. <sup>(c)</sup> Temperature. <sup>(d)</sup> Average line width of all detected transitions. <sup>(e)</sup> Abundance values with respect to the H<sub>2</sub> column density using  $N_{\text{tot}}$  values from the best-fit LTE model. <sup>(f)</sup> Column density from the population diagram method. <sup>(g)</sup> Rotational temperature from the population diagram method.

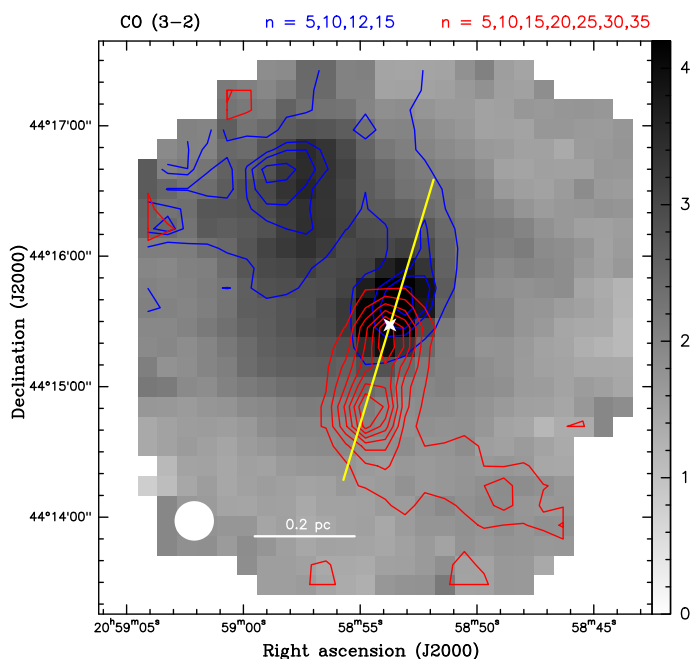


Fig. 5: Integrated intensity map of <sup>12</sup>CO (3–2) (grey-scale image). The blue and red contours represent the blueshifted and redshifted wing emission integrated over the velocity ranges of  $[-6, 2] \text{ km s}^{-1}$  and  $[5.5, 12] \text{ km s}^{-1}$ . The HPBW is shown in the bottom left corner in white. The position of V1057 Cyg is marked with a white cross. The yellow line shows the cut used for the position-velocity diagram shown in Fig. 6. The position angle (PA) of the cut is  $-17^\circ$  (East from North).

The ridge to the southwest seen in our molecular line data is visible in *Herschel* dust-based H<sub>2</sub> column density maps (Szabó et al. 2023a). The dust map, along with our integrated intensity maps, further suggests a large-scale morphology of a filamentary cloud, in which V1057 Cyg is located, as proposed by Sandell & Weintraub (2001).

Ridge structures or filaments, similar to what is seen around V1057 Cyg are typically found in star forming regions (e.g., André et al. 2010; Hacar et al. 2023, for a recent review). A famous example is the Taurus Molecular Cloud 1 (TMC-1), where numerous cloud cores are located along a ridge structure (e.g., Hirahara et al. 1992; Langer et al. 1995). Naturally, the size of the TMC-1 filaments are much larger ( $\sim 10 \text{ pc}$  with cores around

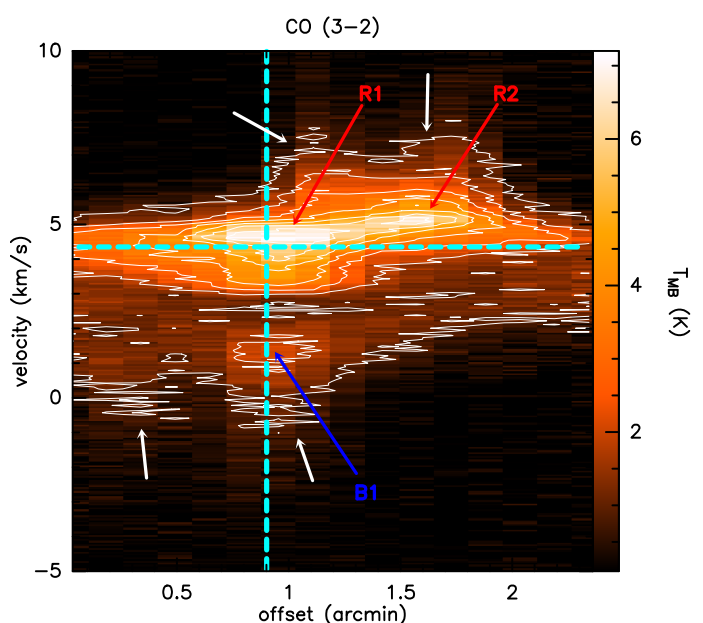


Fig. 6: Position-velocity (p-v) diagram along the yellow line shown in Fig. 5. The horizontal dashed cyan line corresponds to the systemic  $v_{\text{lsr}}$  velocity of  $4.35 \text{ km s}^{-1}$  (Szabó et al. 2023a), while the vertical one corresponds to the source position. The contours start at  $5\sigma$  and end at  $35\sigma$  with  $5\sigma$  steps in between. Peaks of redshifted emission are labeled R1 and R2 and the peak of blueshifted emission is labeled B1. The white arrows highlight the presence of weak "fingers" that may trace episodic ejection events.

$0.1 \text{ pc}$  in size, e.g., L1495 in TMC-1, Schmalzl et al. 2010) than the ridge we see around V1057 Cyg ( $\sim 1\text{--}1.5 \text{ pc}$ ) within our field of view. Ridges with similar sizes to that seen around V1057 Cyg are found in many low-mass star forming regions, with NGC 1333 being a prominent example (e.g., Hacar et al. 2017). We speculate that the condensation detected to the southwest of V1057 Cyg in high density tracers (see Sect. 3.3) represents a secondary, possibly protostellar, dense core in the vicinity of V1057 Cyg. The spatial extent of the  $850 \mu\text{m}$  data of Sandell & Weintraub (2001) do not extend far enough to the south to localise the peak, however, the *Herschel* derived H<sub>2</sub> column density map shows a peak at the position of the southwestern peak

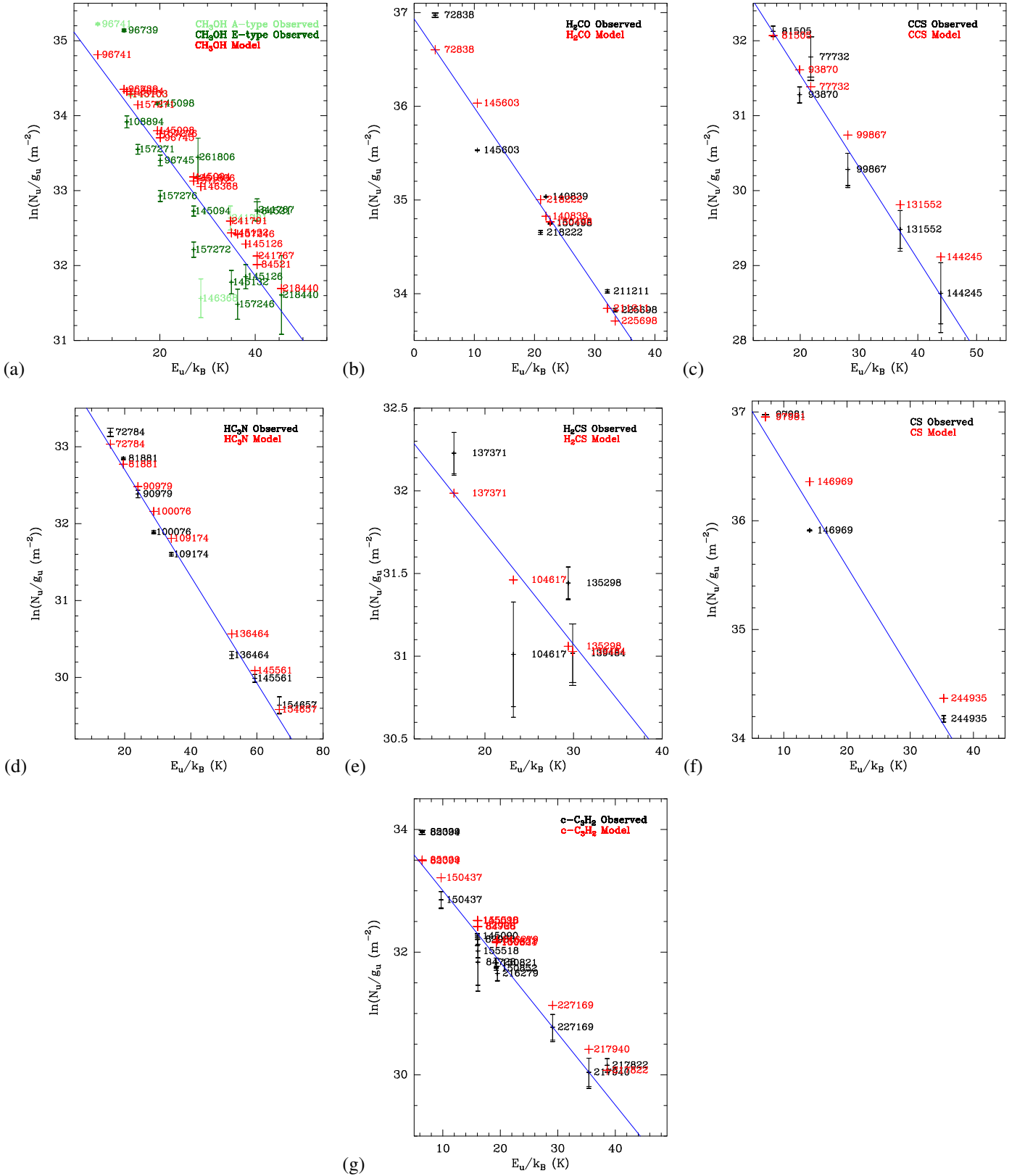


Fig. 7: Population diagrams of: (a) CH<sub>3</sub>OH; (b) H<sub>2</sub>CO; (c) CCS; (d) HC<sub>3</sub>N, (e) H<sub>2</sub>CS; (f) CS; (g) c-C<sub>3</sub>H<sub>2</sub>. The black points (green in the case of CH<sub>3</sub>OH) represent the observations while the red points correspond to the Weeds synthetic spectra computed with the parameters given in Table 4. The blue line is a fit to the observed data points.

seen in our single-dish molecular line data (see, e.g., Green et al. 2013; Szabó et al. 2023a, and Fig. C.1 in the latter).

Previously, the NH<sub>3</sub> (1,1) transition towards V1057 Cyg has been detected with a beam size of  $\sim 37''$  using the Effelsberg 100-



m telescope (Szabó et al. 2023a). In light of our 30-m single-dish map of, for example, the  $\text{N}_2\text{H}^+$  (1–0) emission, it is plausible that the  $\text{NH}_3$  spectrum is contaminated by the northern peak, located at  $\sim 15''$  offset of V1057 Cyg. High-angular resolution observations of high-density tracers with interferometers might probe if V1057 Cyg is an isolated protostar or a member of a cluster similarly to the RNO 1B/1C FUor system (Quanz et al. 2007).

#### 4.2. Temporal variations in the molecular outflow

Both single-dish and interferometric observations of  $^{12}\text{CO}$  (and its isotopologues) have been used to identify molecular outflows associated with FUors and FUor-like objects (e.g., Evans et al. 1994; Kóspál 2011; Fehér et al. 2017; Kóspál et al. 2017a; Cruz-Sáenz de Miera et al. 2023, and references therein). As presented in Sect. 3.3, the molecular outflow of V1057 Cyg was first reported by Evans et al. (1994), based only on the presence of blueshifted wing emission in a single  $^{12}\text{CO}$  3–2 spectrum of the source observed with the Caltech Submillimeter Observatory 10.4-meter telescope (CSO). Our new  $^{12}\text{CO}$  (3–2) APEX map reveals a clear bipolar outflow morphology (Fig. 5), with the redshifted component reported here for the first time. We note that the CSO spectrum of Evans et al. (1994), which peaks at  $8.7 \text{ km s}^{-1}$ , is shifted by about  $4.5 \text{ km s}^{-1}$  compared to the APEX one. This discrepancy is puzzling. Although the Gaussian fit is unreliable for the  $^{12}\text{CO}$  data, it would still be closer to our  $^{13}\text{CO}$  and  $\text{C}^{18}\text{O}$  (1–0)  $v_{\text{lsr}}$  of  $3.86 \text{ km s}^{-1}$  and  $4.09 \text{ km s}^{-1}$ , and also to those derived from interferometric data by Fehér et al. (2017) for  $^{13}\text{CO}$  and  $\text{C}^{18}\text{O}$  (1–0) with values of  $4.05 \text{ km s}^{-1}$  and  $4.10 \text{ km s}^{-1}$ , respectively. We suspect that the frequency axis of the spectrum published in Evans et al. (1994) was not properly calibrated.

Figure 5 reveals the outflow originating from V1057 Cyg, with the redshifted lobe pointing to the South-South-East and the blueshifted one to the North-North-West. We measured the length of the lobes,  $R_{\text{lobe}}$ , and maximum velocities,  $v'_{\text{max}}$ , to estimate the dynamical time,  $t_d$ , of the outflow with the formula  $t_d = \frac{R_{\text{lobe}}}{v'_{\text{max}} \tan i}$ , with  $i$  the inclination of the outflow axis to the line of sight (summarised in Table 5, Beuther et al. 2002). The outflow map shows bipolar morphology with no overlap between the redshifted and blueshifted emissions, implying an intermediate inclination angle. Therefore we estimated  $t_d$  assuming a range of inclinations between  $10^\circ$  and  $80^\circ$  and obtained values ranging from  $5 \times 10^3$  yrs to  $234 \times 10^3$  yrs. Previous studies analysing the disk of V1057 Cyg derived an inclination of  $62^\circ$  (Liu et al. 2018; Szabó et al. 2021). In the following we adopt the dynamical times estimated with  $62^\circ$ , which is 15 000 years for the blue, and 22 000 years for the red lobe of the outflow of V1057 Cyg. A survey of 20 FUors, also using the APEX 12-m telescope (Cruz-Sáenz de Miera et al. 2023), found dynamical times on the order of thousands of years, from  $3 \times 10^3$  yrs to  $130 \times 10^3$  yrs, suggesting that the detected outflows are most likely not related to the current outbursts in the sample. V1057 Cyg has been in outburst for about 50 years (Herbig 1977; Herbig et al. 2003; Clarke et al. 2005; Szabó et al. 2021), therefore the outflow cannot result from the ongoing outburst alone. High velocity gas may have been ejected in the recent outburst, however, this gas would be confined to small-scales, remaining unresolved in single-dish observations (see also the results of Cruz-Sáenz de Miera et al. 2023).

Signs of potential past ejection activity in V1057 Cyg have not yet been explored. One way to search for historical mass ejection events is to inspect the kinematics of the outflow in a

Table 5: Properties of each lobe of the outflow of V1057 Cyg determined from the APEX  $^{12}\text{CO}$  3–2 observations.

Lobe	$v_{\text{max}}^{(a)}$ ( $\text{km s}^{-1}$ )	$v'_{\text{max}}^{(b)}$ ( $\text{km s}^{-1}$ )	$R_{\text{lobe}}^{\text{proj}(c)}$ ( $''$ )	$i^{(d)}$ ( $^\circ$ )	$t_d^{(e)}$ ( $10^3$ years)
Blue	–6	10.35	70	10	163
Red	12	7.65	74	10	235
Blue				45	29
Red				45	41
Blue				62	15
Red				62	22
Blue				80	5
Red				80	7.3

**Notes.** <sup>(a)</sup> Minimum (blueshifted) and maximum (redshifted) velocities. <sup>(b)</sup> Maximum velocities  $v'_{\text{max}} = |v_{\text{max}} - v_{\text{sys}}|$ , where  $v_{\text{sys}} = 4.35 \text{ km s}^{-1}$ . <sup>(c)</sup> Projected length of a lobe along the outflow axis. <sup>(d)</sup> Input inclination for estimating the dynamical time of the outflow lobe. <sup>(e)</sup> Dynamical time of the outflow lobe.

position-velocity (p-v) diagram, which can be used as a "fossil record" (e.g., Arce & Goodman 2001; Zhou et al. 2024). The p-v diagram displayed in Fig. 5 shows discrete peaks and hints at structures similar to the turbulent jet + jet bow shock model, which can be interpreted as episodic accretion/ejection events (see, e.g., Plunkett et al. 2015). In this model, the episodic variation in the jet velocity produces an internal bow shock driving an internal shell in addition to the terminal shock. The  $^{12}\text{CO}$  emission traces cool (i.e., lower than 100 K) swept-up material, providing a record of the timing history of mass-loss event(s). Our p-v diagram shows blue- and redshifted peaks (R1, R2, and B1 in Fig. 6), with velocity offsets from the systemic velocity of V1057 Cyg. Moreover, the p-v diagram shows weak "fingers", revealed by the lowest contour in the blue- and redshifted emission (indicated by white arrows in Fig. 6). This is reminiscent of the results of Plunkett et al. (2015), who report a saw-like pattern along the extent of the  $^{12}\text{CO}$  emission of the Class 0 source CARMA-7. Plunkett et al. (2015) proposed that the peaks may indicate shocks and the fingers (in their case the saw-like structure) may be evidence for a period where the faster ejecta overtakes the slower one. Furthermore, previous ejections could entrain the outflow material, therefore appearing as clumpy (see peaks R1, R2, and B1 in Fig. 6), creating distinct shocks when a newer ejecta overtakes the previous, older one (Plunkett et al. 2015). The clumpy structure of the  $^{12}\text{CO}$  emission of V1057 Cyg might indicate episodic ejection mechanisms, rather than a smooth, continuous/homogeneous outflow. The prominent peaks and weak fingers complemented with the estimated dynamical times further suggest past outburst activity of V1057 Cyg.

#### 4.3. Brief comparison to other FUors

Millimeter-wavelength observations can provide information on both the small- and large-scales in the environments of YSOs. The majority of previous studies of FUors, whether single-dish or interferometric observations, have mainly focused on  $^{12}\text{CO}$  and its rarer isotopologues of  $^{13}\text{CO}$  and  $\text{C}^{18}\text{O}$  to probe the molecular outflows (e.g., Evans et al. 1994; Fehér et al. 2017; Ruiz-Rodríguez et al. 2017b,a; Hales et al. 2020; Wendeborn et al. 2020; Cruz-Sáenz de Miera et al. 2023; Nogueira et al. 2023, and references therein). However, employing other molecular species has been increasing over the past decade using both

single-dish and interferometric facilities. Despite being a famous member within its class and a classical FUor, V1057 Cyg had not yet been systematically searched for molecular emission in the millimeter domain, which similar to the optical and near-infrared in depth-studies (see, e.g., [Herbig et al. 2003](#); [Szabó et al. 2021, 2022](#)) could be valuable when classifying new FUors. Prior to this work, molecular line observations towards our target mainly focused on  $^{12}\text{CO}$  (and its isotopic species), which has been observed since the 1970s, following the outburst.  $^{12}\text{CO}$  and  $^{13}\text{CO}$  1–0 line emission was first reported by [Bechis & Lo \(1975\)](#), followed by the detection of other transitions of  $^{12}\text{CO}$  and its isotopic species throughout the decades, conducted both with single-dishes and interferometers (see Sect. 3.2). Detection of the simple molecule CN (3–2) was also reported towards V1057 Cyg with a peak  $v_{\text{lsr}}$  comparable to the  $^{12}\text{CO}$  observations ([Stäuber et al. 2007](#)). The recent NOEMA observations by [Calahan et al. \(2024b\)](#) show that V1057 Cyg stands out among a small sample of surveyed eruptive YSOs, with detections of several COMs (e.g.,  $\text{CH}_3\text{OH}$ ,  $\text{CH}_3\text{CN}$ ,  $\text{CH}_3\text{OCHO}$ ), sulfur-bearing molecules (e.g.,  $\text{SO}$ ,  $\text{SO}_2$ ), and others. In the following, we give a brief overview of the most relevant molecular line studies targeting FUors and briefly compare their results to ours. These include both single-dish and interferometric observations. For the relevant comparison, we mention RNO 1B/1C, L1551 IRS5, and V883 Ori. It is important to note that beam dilution is an important factor when comparing single-dish and interferometric studies, since it limits the capability of single-dish telescopes to detect compact emission.

For the overview, we constructed Table 6, which lists a selection of species ranging from simple molecules to COMs. The table indicates for each molecule the sources for which a detection has been reported. The FUor binary RNO 1B/1C, is one of the earliest documented examples of molecular emission associated with FUors (apart from CO, [Evans et al. 1994](#)), which include detection of SiO (5–4),  $\text{H}_2\text{CO}$  (3–2),  $\text{CH}_3\text{OH}$  (4–3),  $\text{C}^{18}\text{O}$  (2–1), CS (7–6 and 2–1), and  $\text{HCO}^+$  (4–3) emission ([McMuldroy et al. 1995](#)). In this case, the CO emission was found to trace the bipolar outflow and CS (2–1) to probe the dense cloud core around the binary. In all cases, they find relatively cold (below 35 K) emission tracing the environment of RNO 1B/1C, which is similar to the cold molecular emission detected towards V1057 Cyg, however the rotational temperatures that we derived toward V1057 Cyg are lower than toward RNO 1B/1C. The column densities are about an order of magnitude lower for V1057 Cyg than in RNO 1B/1C. Similarly to RNO 1B/1C, we also detect further indication of dense material (together with the previous  $\text{NH}_3$  observations and compact morphology of dust emission, [Szabó et al. 2023a](#)) from a number of transitions of CS, CCS,  $\text{HCO}^+$  (and their isotopologues) or  $\text{N}_2\text{H}^+$  (see also, [McMuldroy et al. 1995](#); [Shirley 2015](#); [Yamamoto 2017](#), and references therein), traced on single-dish scales.

Probably the most prominent example in the literature for molecular line emission is the FUor-like, Class I protostar, L1551 IRS5 (e.g., [Adams et al. 1987](#); [Looney et al. 1997](#); [Connelley & Reipurth 2018](#)), located in Taurus, at a distance of  $\sim 140$  pc ([Zucker et al. 2019](#)), with a luminosity of  $L = 28 L_\odot$  ([Butner et al. 1991](#)). This source might be one of the most line-rich sources associated with the class, and includes detection of molecular species ranging from simple to complex molecules (see Table 6, and also e.g., [Fridlund et al. 2002](#); [White et al. 2006](#); [Mercimek et al. 2022](#), and references therein). The most notable result toward this source is the interferometric detection of a hot corino (a region around a low-mass protostar bright in emission of COMs, e.g., [Yamamoto 2017](#)) traced by  $\text{CH}_3\text{OH}$

(and its isotopologues),  $\text{CH}_2\text{DOH}$ ,  $\text{HCOOCH}_3$ , and  $\text{CH}_3\text{CH}_2\text{OH}$  ([Bianchi et al. 2020](#)). The most recent study on this source reports a survey, covering the 3 mm and 2 mm windows using the 30-m telescope, revealing a total of 75 species (including isotopologues, [Marchand et al. 2024](#)). V1057 Cyg is not as line-rich as L1551 IRS5 with a lower number of detected species and in particular only three COMs ( $\text{CH}_3\text{OH}$ ,  $\text{CH}_3\text{CCH}$ , and  $\text{CH}_3\text{CN}$ ) out of the 15 reported by [Marchand et al. \(2024\)](#). The majority of species detected in the recent survey of L1551 IRS5 trace the cold envelope with temperatures  $\leq 10$  K, however, the authors report molecules with  $\geq 5$  atoms and a few S-bearing species ( $\text{C}_3\text{S}$ ,  $\text{SO}$ ,  $\text{SO}_2$ ) to trace warmer,  $\geq 30$  K, regions. In V1057 Cyg, we do not detect molecular emission above 10 K, implying that we only trace cold molecular emission towards this source. The column densities derived by the authors for L1551 IRS5 are within the same order of magnitude as the column densities we derived for V1057 Cyg, with the exception of  $c\text{-C}_3\text{H}_2$ , which has an order of magnitude lower column density in V1057 Cyg ([Marchand et al. 2024](#)). However, we note that the emission detected by our single-dish observations is extended over  $25\text{--}30''$ , i.e.,  $\sim 0.1$  pc at the distance of  $\sim 900$  pc, and likely traces the disk, the envelope, and the surrounding cloud while the observations of L1551 IRS5 and V883 Ori trace smaller scales (see below).

Finally, we give a brief comparison to V883 Ori, a FUor transiting from the Class I to the Class II phase, located at a distance of  $d = 338$  pc, with a bolometric luminosity of  $L = \sim 220 L_\odot$  (e.g., [Furlan et al. 2016](#); [Connelley & Reipurth 2018](#); [Lee et al. 2019](#)). This source has been the focus of a number of interferometric observations, revealing in particular a snow-line shift attributed to the outburst, a complex physical structure of its environment traced by high-density (e.g., HCN,  $\text{HCO}^+$ , DCN) and shock tracers (e.g.,  $\text{CH}_3\text{OH}$ , SiO, SO), a ring-like structure traced by  $\text{HCO}^+$  emission, and a rich chemistry traced by COMs (see Table 6 and also e.g., [Ruíz-Rodríguez et al. 2017a](#); [Lee et al. 2019](#); [Ruíz-Rodríguez et al. 2022](#); [Yamamoto et al. 2024](#); [Lee et al. 2024](#)). The most recent study of [Lee et al. \(2024\)](#) focuses on the detection of simple molecular species and a small list of COMs using ALMA Band 6 data, a frequency regime partly covered by our single-dish observations. We find many molecular species detected in both V1057 Cyg and V883 Ori (see Table 6). The interferometric data traces different physical components of the environment of V883 Ori: HDCO and HNCO trace mainly the water sublimation front, HCN emission traces both the inner and outer disk, revealing an arm-like structure, while HNC and DNC trace a ring structure at the outer disk boundary ([Lee et al. 2024](#)). With the single-dish data of V1057 Cyg, we are only able to trace the large scale emission (the ridge with the southern peak and the northern concentration, and the outflow, see also Sects. 3.3, 4.1, and 4.2). Between these two sources, we find V883 Ori to harbor more COMs, similarly to L1551 IRS5. However, for the more evolved nature of V1057 Cyg it still demonstrates a line-rich environment, motivating follow-up interferometric observations. Furthermore, we do not detect water lines in this survey (despite transitions covered by the setup) compared to V883 Ori, however, we note that  $\text{HDO } 3_{(1,2)}\text{--}2_{(2,1)}$  emission has been recently confirmed by sensitive interferometric NOEMA observations towards V1057 Cyg ([Calahan et al. 2024b](#)).

#### 4.4. Chemical signatures of outbursts and outlook

Episodic outbursts may strongly influence the disks around protostars, introducing changes to the thermal structure and inducing chemical changes (e.g., [Fischer et al. 2023](#)), which may be used to identify past outburst events.

Table 6: Brief overview (for visualisation purposes) of the relevant molecular emission reported towards RNO 1B/1C, L1551 IRS5, V883 Ori, and V1057 Cyg discussed in Sect 4.4. For the table L1551 IRS5 is abbreviated as L1551. Only the main isotopologues are listed below, in many cases the secondary isotopologues of the main ones are also detected.

Species	Detected (source name/names)	Species	Detected (source name/names)
CN	L1551, V1057 Cyg	HDO	L1551, V883 Ori, V1057 Cyg
CO	RNO 1B/1C, L1551, V883 Ori, V1057 Cyg	HDCO	L1551, V883 Ori, V1057 Cyg
SO	L1551, V883 Ori, V1057 Cyg	NH <sub>2</sub> D	L1551
SiO	RNO 1B/1C, V883 Ori	N <sub>2</sub> D <sup>+</sup>	L1551
CS	RNO 1B/1C, L1551, V883 Ori, V1057 Cyg	C <sub>2</sub> DCCCH	L1551
NS	L1551	CCH	L1551 IRS5, V1057 Cyg
HCN	L1551, V883 Ori, V1057 Cyg	CCS	L1551, V1057 Cyg
HCO	L1551, V883 Ori, V1057 Cyg	c-C <sub>3</sub> H	L1551
H <sub>2</sub> S	L1551	l-C <sub>3</sub> H <sub>2</sub>	L1551
HNC	L1551, V883 Ori, V1057 Cyg	c-C <sub>3</sub> H <sub>2</sub>	L1551, V1057 Cyg
OCS	L1551, V883 Ori	HC <sub>3</sub> N	L1551, V1057 Cyg
SO <sub>2</sub>	L1551, V883 Ori	CH <sub>3</sub> CCH	L1551, V1057 Cyg
NH <sub>3</sub>	RNO 1B/1C, L1551, V1057 Cyg	HC <sub>5</sub> N	L1551, V1057 Cyg
H <sub>2</sub> CO	RNO 1B/1C, L1551, V883 Ori, V1057 Cyg	CH <sub>3</sub> CN	L1551, V883 Ori, V1057 Cyg
H <sub>2</sub> CS	L1551, V1057 Cyg	CH <sub>3</sub> OH	RNO 1B/1C, L1551, V883 Ori, V1057 Cyg
CH <sub>3</sub>	L1551	CH <sub>3</sub> CHO	L1551, V883 Ori
HCO <sup>+</sup>	RNO 1B/1C, L1551, V883 Ori, V1057 Cyg	CH <sub>3</sub> CCH	L1551, V883 Ori, V1057 Cyg
HCS <sup>+</sup>	L1551, V883 Ori, V1057 Cyg	CH <sub>3</sub> CH <sub>2</sub> OH	L1551
N <sub>2</sub> H <sup>+</sup>	L1551, V1057 Cyg	CH <sub>3</sub> OCH <sub>3</sub>	L1551, V883 Ori
N <sub>2</sub> D <sup>+</sup>	L1551	C <sub>2</sub> H <sub>3</sub> CN	V883 Ori
HOCO <sup>+</sup>	L1551	HCOOCH	L1551
CCD	L1551, V1057 Cyg	H <sub>2</sub> CCO	L1551, V883 Ori
DCN	L1551, V883 Ori, V1057 Cyg	HNCO	L1551, V883 Ori, V1057 Cyg
DCO <sup>+</sup>	L1551, V883 Ori, V1057 Cyg		
D <sub>2</sub> CO	L1551		
DNC	L1551, V883 Ori, V1057 Cyg		

**Notes.** The most relevant references for each source. RNO 1B/1C: Evans et al. (1994); McMuldroy et al. (1995). L1551 IRS5: Fridlund et al. (2002); White et al. (2006); Bianchi et al. (2020); Mercimek et al. (2022); Marchand et al. (2024, and references therein). V883 Ori: Ruíz-Rodríguez et al. (2017a); Lee et al. (2019); Ruíz-Rodríguez et al. (2022); Cruz-Sáenz de Miera et al. (2023, and references therein); Tobin et al. (2023); Lee et al. (2024); Yamato et al. (2024). V1057 Cyg: Bechis & Lo (1975); Leveault (1988); Evans et al. (1994); Stäuber et al. (2007); Kóspál (2011); Fehér et al. (2017); Calahan et al. (2024b); and this work.

Rab et al. (2017) extended the radiation thermo-chemical disk code, PRODIMO (PROtoplanetary DISk MOdel, Woitke et al. 2009, 2016), to treat envelope structures by feeding a representative Class I model. They used simulated, spatially resolved ALMA C<sup>18</sup>O 2–1 observations and found this particular transition to be a good tool to probe post-outburst sources. In the model, the spatially resolved 2–1 transition emission exhibits distinct signatures, such as a gap due to the freeze out of the molecules (see Fig. 4 of Rab et al. 2017). In our line survey, we detected and mapped the C<sup>18</sup>O 2–1 transition with APEX and the emission is resolved in the north-south direction, tracing the ridge, but our observations do not resolve the disk around V1057 Cyg (see Fig. 4 and Table A.2). Interferometric observations of the C<sup>18</sup>O 1–0 transition by Fehér et al. (2017) found a rotating envelope with a radius of 5'', or 3000 au at  $d = 600$  pc (common distance used before *Gaia*, Bailer-Jones et al. 2018a,b), corresponding to ~4500 au at ~900 pc, however, with the single-dish observations of this transition with a beam size of 22.4'', we do not resolve the envelope either. The model of Rab et al. (2017) accounts for both disk and envelope emission, and the outburst induced changes are seen in the radial distribution of the <sup>12</sup>CO emission on scales of a few 1000 au, thus much larger than the typical disk scales. Our single-dish observations have an angular resolution that corresponds to about ~18 000 au and, therefore, cannot resolve the <sup>12</sup>CO structures predicted by the model which are at a few 1000 au scales.

The other notable model is by Molyarova et al. (2018), who used the ANDES physical-chemical code (Akimkin et al. 2013) to follow the impact of a FUor outburst on the chemical evolution and to identify molecular tracers on different timescales. Two main groups are specified: species with abundances sensitive to the ongoing outburst but returning quickly (i.e., a few years after the peak outburst) to the quiescent (pre-outburst) values; and those that take longer to return to pre-outburst or even remain overabundant for decades (> 20 yrs). The most notable prediction is formaldehyde (H<sub>2</sub>CO), whose abundance can grow by up to 4–6 magnitudes, and take 30–120 years to deplete back onto dust grains, making it a good candidate tracer to, in theory, identify post-outburst sources. They modeled the brightest H<sub>2</sub>CO transition observed in disks, the 3<sub>03</sub>–2<sub>02</sub> transition at 218.222 GHz, with input parameters based on the FUor outburst of V346 Nor, which in 2010 seemed to finish abruptly its outburst (and was thought to be the first FUor to do so, see Kraus et al. 2016). However, the study of Kóspál et al. (2020) showed evidence for the source gradually brightening back to almost the same brightness level prior to the abrupt fading event, and concluded the fading was likely due to different mechanisms, including increase of the line-of-sight extinction, and appearance of warm material possibly refuelling the outburst. We detect the H<sub>2</sub>CO (3<sub>03</sub>–2<sub>02</sub>) transition toward V1057 Cyg in the 30-m data, however, it is fainter than other transitions of H<sub>2</sub>CO detected in the survey. We find the abundances of H<sub>2</sub>CO and CH<sub>3</sub>OH (see Table 4) to be orders of magnitude lower than the abundances



predicted by both the medium and grown dust models by Molyarova et al. (2018). However, our abundances correspond to material at the scale of  $\sim 30''$ , while the model abundances are predicted at the much smaller scale of the disk. In contrast, the  $\text{HC}_3\text{N}$  abundance is closer to the model predictions, although its abundance is lower than those of  $\text{H}_2\text{CO}$  and  $\text{CH}_3\text{OH}$ . We note that our  $\text{HC}_3\text{N}$  map shows extended emission, without a peak centered on V1057 Cyg, hence suggesting that the  $\text{HC}_3\text{N}$  line emission detected towards the target is not dominated by compact, unresolved emission. We do not have maps of  $\text{H}_2\text{CO}$  or  $\text{CH}_3\text{OH}$  emission to check whether the emission peaks on the target. The CS abundance derived for V1057 Cyg is higher than the model predictions. The  $\text{NH}_3$  abundance derived in an earlier study (Szabó et al. 2023a) is  $\sim 1$  order of magnitude lower than the abundance predicted by the model of Molyarova et al. (2018).

Considering that V1057 Cyg has been in outburst for over 50 years, it is plausible that during the peak of the outburst, the abundance values were elevated due to the heat from the central source. The detection of multiple transitions of many molecular species and the lower abundances compared to the model predictions show that many species are still present and not yet frozen-out to dust surfaces. On the other hand, the single-dish data clearly trace large-scale structures (i.e., the ridge), and it is uncertain what fraction of the measured flux is related to a more compact disk around the source and what is related to the extended ridge.

The available chemical models, together with line surveys such as the one presented here motivate follow-up studies both observational and theoretical. In the case of V1057 Cyg, high-angular resolution observations could resolve the smaller-scale structures (i.e., on scales of the disk and envelope system) and their connection to the larger scale emission traced by the ridge both to the north and south from the source position. Future spatially resolved observations can reveal similar structures predicted in the models due to the inside out freeze-out (Rab et al. 2017), snow-line shifts (either water or other molecules) attributed to the outburst, or help distinguishing which species trace the different layers in the system, similarly to what has been found in V883 Ori (e.g., Tobin et al. 2023; Yamato et al. 2024). This may allow to probe the impact of the outburst on the physical and chemical structure of the disk and the close environment of V1057 Cyg (e.g., Molyarova et al. 2018; Lee et al. 2024; Andreu et al. 2023). Further detection of indicators of the water snowline (e.g., Molyarova et al. 2018) and information on the D/H ratio in more evolved sources such as V1057 Cyg may add more information on Class II sources, currently absent from the statistics (see Fig. 3 of Andreu et al. 2023, and references therein). Despite our single-dish data not being able to resolve the small scales, the line survey shows a richer line emission than might have been expected for a relatively more evolved, classical FUor like V1057 Cyg, and motivates higher-angular resolution studies to determine whether emission from molecules, such as,  $\text{H}_2\text{CO}$  and  $\text{CH}_3\text{OH}$  is coming from the large-scale ridge or a compact structure around the source. Furthermore, high-angular resolution observations of  $^{12}\text{CO}$  could reveal past episodic ejection events in greater detail.

## 5. Conclusions

In this paper, we present the first wide-band line survey in the millimeter wavelength regime of V1057 Cyg and its surrounding environment. This Class II source has been in outburst for about 50 years, and has not yet shown signs of returning to qui-

escence (Szabó et al. 2021). The line survey has an almost continuous frequency coverage from  $\sim 72$  GHz to  $\sim 263$  GHz (with spatial resolution between  $\sim 36''$  and  $\sim 10''$ ) with the IRAM 30-m telescope. Additionally, specific frequency ranges around 219, 227, 291, and 344 GHz (with spatial resolution between  $\sim 30''$  and  $\sim 19''$ ) were observed with the APEX 12-m telescope. The line identification and analysis carried out on the data lead to the following conclusions:

- We identified (mostly) simple *C*-, *N*-, *O*-, *S*-bearing molecules (e.g., CN, CS, HCN), deuterated species (e.g., DCN), molecular ions (e.g.,  $\text{HCO}^+$ ), more simple *C*-chain molecules (e.g.,  $\text{C}_2\text{H}$ ,  $\text{HC}_3\text{N}$ ), and complex organic molecules. V1057 Cyg displays lines from 35 molecular species (including isotopologues). The different spatial distribution of emission in the integrated line intensity maps indicate that the various lines sample different regions in the environment of the source. Most of the lines detected in this survey have been detected in disks around T Tauri stars (e.g., Dutrey et al. 2014), the closest in evolution to V1057 Cyg and other well studied FUors (e.g., Marchand et al. 2024; Lee et al. 2024).
- Most of the lines show narrow single-peaked line profiles that are well described by single Gaussian fits, with the exception of outflow tracers that show broader line wings, indicating outflow activity. The LSR velocities in all cases indicate that the line emission is associated with the circumstellar environment of V1057 Cyg.
- Population diagrams of molecules detected in several transitions ( $\text{CH}_3\text{OH}$ ,  $\text{H}_2\text{CO}$ , CCS,  $\text{HC}_3\text{N}$ ,  $\text{H}_2\text{CS}$ , CS, *c*- $\text{C}_3\text{H}_2$ ) were constructed, indicating rotational temperatures ( $T_{\text{rot}}$ ) ranging from 8.1 K to 14.8 K. We derived column densities ( $N_{\text{tot}}$ ) of these molecules under the assumption of LTE with values ranging from  $1.4 \times 10^{12} \text{ cm}^{-2}$  to  $2.8 \times 10^{13} \text{ cm}^{-2}$ . The derived column densities are  $\sim 1$  order of magnitude lower than those derived for younger, line rich FUors, but our single-dish survey probes larger scales.
- The emission of several molecular species was mapped with the IRAM 30-m or the APEX 12-m telescopes. The integrated intensity maps trace a parsec-scale ridge that runs from the Southwest to the North, going through the position of V1057 Cyg. This ridge coincides with the ridge traced earlier in dust continuum emission (Sandell & Weintraub 2001; Green et al. 2013; Szabó et al. 2023a), however, our molecular line maps cover a larger area towards the southwest. Two clumps of molecular emission, clearly visible in the integrated intensity maps of HCN, HNC,  $\text{N}_2\text{H}^+$  1–0, and  $\text{HC}_3\text{N}$  10–9, are detected along the ridge to the North and Southwest of V1057 Cyg, offset by  $\sim 15''$  ( $\sim 0.06$  pc), and  $\sim 108''$  ( $\sim 0.46$  pc) respectively from the source position. Our results could indicate that V1057 Cyg is forming as part of a small cluster, similarly to several other FUors (e.g., White et al. 2006; Quanz et al. 2007), and motivate future interferometric observations to reveal the protostellar content of the filamentary structures.
- Our new  $^{12}\text{CO}$  3–2 map reveals a bipolar outflow centered on V1057 Cyg. We estimate a dynamical time for the outflow of tens of thousands of years (15 000 years for the blue and 22 000 years for the red lobe of the outflow), implying that the detected outflow does not result from the current outburst activity alone. The position-velocity diagram shows discrete peaks and hints at structures representing episodic ejection events, further indicating outburst activity in the past evolution of V1057 Cyg.



Despite being at a distance of almost 900 pc and being a more evolved (i.e., Class II) object, V1057 Cyg exhibits a line-rich environment in our single-dish observations. While the molecular emission in the environment of V1057 Cyg does not reveal clear evidence of the imprint of an outburst on the chemistry of the object on the scales traced by our single-dish data, the line-rich spectra motivate interferometric observations to spatially resolve the emission. Our results also motivate similar studies of a larger sample of FUors to study the range of astrochemical properties associated with this class of outbursting protostars, and to improve the current statistics regarding the outbursts' effects on the chemical composition of their close environments, ultimately the future birthplace of planets.

*Acknowledgements.* We thank the anonymous referee for valuable feedback which has improved the quality of our manuscript. Zs. M. Szabó acknowledges funding from a St. Leonards scholarship from the University of St. Andrews and C. J. C. acknowledges support from the STFC (grant ST/Y002229/1). For the purpose of open access, the author has applied a Creative Commons Attribution (CC BY) licence to any Author Accepted Manuscript version arising. Y.G. is supported by the Strategic Priority Research Program of the Chinese Academy of Sciences, Grant No. XDB0800301. This work is based on observations carried out under project number 060-21 (PI: Karl M. Menten) with the IRAM 30m telescope. IRAM is supported by INSU/CNRS (France), MPG (Germany) and IGN (Spain). This publication is based on data acquired with the Atacama Pathfinder Experiment (APEX) under programme ID M9530C\_107, M9515A\_108, and M9523C\_109. APEX has been a collaboration between the Max-Planck-Institut für Radioastronomie, the European Southern Observatory, and the Onsala Space Observatory. This work was also supported by the NKFIH excellence grant TKP2021-NKTA-64.

## References

- Adams, F. C., Lada, C. J., & Shu, F. H. 1987, *ApJ*, 312, 788
- Akimkin, V., Zhukovska, S., Wiebe, D., et al. 2013, *ApJ*, 766, 8
- André, P., Men'shchikov, A., Bontemps, S., et al. 2010, *A&A*, 518, L102
- Andreu, A., Coutens, A., Cruz-Sáenz de Miera, F., et al. 2023, *A&A*, 677, L17
- Arce, H. G. & Goodman, A. A. 2001, *ApJ*, 551, L171
- Audard, M., Abraham, P., Dunham, M. M., et al. 2014, in *Protostars and Planets VI*, ed. H. Beuther, R. S. Klessen, C. P. Dullemond, & T. Henning, 387
- Bailer-Jones, C. A. L., Rybizki, J., Founesneau, M., Mantelet, G., & Andrae, R. 2018a, *AJ*, 156, 58
- Bailer-Jones, C. A. L., Rybizki, J., Founesneau, M., Mantelet, G., & Andrae, R. 2018b, *VizieR Online Data Catalog*, I/347
- Batrla, W. & Menten, K. M. 1988, *ApJ*, 329, L117
- Bechis, K. P. & Lo, K. Y. 1975, *ApJ*, 201, 118
- Belloche, A., Garrod, R. T., Müller, H. S. P., et al. 2009, *A&A*, 499, 215
- Belloche, A., Müller, H. S. P., Garrod, R. T., & Menten, K. M. 2016, *A&A*, 587, A91
- Belloche, A., Müller, H. S. P., Menten, K. M., Schilke, P., & Comito, C. 2013, *A&A*, 559, A47
- Beuther, H., Schilke, P., Sridharan, T. K., et al. 2002, *A&A*, 383, 892
- Bianchi, E., Chandler, C. J., Ceccarelli, C., et al. 2020, *MNRAS*, 498, L87
- Breen, S. L., Contreras, Y., Dawson, J. R., et al. 2019, *MNRAS*, 484, 5072
- Busch, L. A., Belloche, A., Garrod, R. T., Müller, H. S. P., & Menten, K. M. 2024, *A&A*, 681, A104
- Butner, H. M., Evans, Neal J., I., Lester, D. F., Levreault, R. M., & Strom, S. E. 1991, *ApJ*, 376, 636
- Calahan, J. K., Bergin, E. A., van't Hoff, M., et al. 2024a, *ApJ*, 967, 158
- Calahan, J. K., Bergin, E. A., van't Hoff, M., et al. 2024b, *ApJ*, 967, 158
- Carter, M., Lazareff, B., Maier, D., et al. 2012, *A&A*, 538, A89
- Ceccarelli, C., Caselli, P., Fontani, F., et al. 2017, *ApJ*, 850, 176
- Ceccarelli, C., Codella, C., Balucani, N., et al. 2022, arXiv:2206.13270
- Chen, X., Ellingsen, S. P., Shen, Z.-Q., Titmarsh, A., & Gan, C.-G. 2011, *ApJS*, 196, 9
- Cieza, L. A., Casassus, S., Tobin, J., et al. 2016, *Nature*, 535, 258
- Clarke, C. J., Lodato, G., Melnikov, S. Y., & Ibrahimov, M. A. 2005, *MNRAS*, 361, 942
- Connelley, M. S. & Reipurth, B. 2018, *ApJ*, 861, 145
- Cruz-Sáenz de Miera, F., Kóspál, Á., Abraham, P., et al. 2023, *ApJ*, 945, 80
- Dutrey, A., Semenov, D., Chapillon, E., et al. 2014, in *Protostars and Planets VI*, ed. H. Beuther, R. S. Klessen, C. P. Dullemond, & T. Henning, 317–338
- Endres, C. P., Schlemmer, S., Schilke, P., Stutzki, J., & Müller, H. S. P. 2016, *Journal of Molecular Spectroscopy*, 327, 95
- Evans, Neal J., I., Balkum, S., Levreault, R. M., Hartmann, L., & Kenyon, S. 1994, *ApJ*, 424, 793
- Fehér, O., Kóspál, Á., Abraham, P., Hogerheijde, M. R., & Brinch, C. 2017, *A&A*, 607, A39
- Fischer, W. J., Hillenbrand, L. A., Herczeg, G. J., et al. 2023, in *Astronomical Society of the Pacific Conference Series*, Vol. 534, *Astronomical Society of the Pacific Conference Series*, ed. S. Inutsuka, Y. Aikawa, T. Muto, K. Tomida, & M. Tamura, 355
- Fridlund, C. V. M., Bergman, P., White, G. J., Pilbratt, G. L., & Tauber, J. A. 2002, *A&A*, 382, 573
- Furlan, E., Fischer, W. J., Ali, B., et al. 2016, *ApJS*, 224, 5
- Goldsmith, P. F. & Langer, W. D. 1999, *ApJ*, 517, 209
- Green, J. D., Evans, Neal J., I., Kóspál, Á., et al. 2013, *ApJ*, 772, 117
- Green, J. D., Hartmann, L., Calvet, N., et al. 2006, *ApJ*, 648, 1099
- Güsten, R., Nyman, L. Å., Schilke, P., et al. 2006, *A&A*, 454, L13
- Hacar, A., Clark, S. E., Heitsch, F., et al. 2023, in *Astronomical Society of the Pacific Conference Series*, Vol. 534, *Protostars and Planets VII*, ed. S. Inutsuka, Y. Aikawa, T. Muto, K. Tomida, & M. Tamura, 153
- Hacar, A., Tafalla, M., & Alves, J. 2017, *A&A*, 606, A123
- Hales, A. S., Pérez, S., Gonzalez-Ruilova, C., et al. 2020, *ApJ*, 900, 7
- Hartmann, L. & Kenyon, S. J. 1996, *ARA&A*, 34, 207
- Herbig, G. H. 1966, *Vistas in Astronomy*, 8, 109
- Herbig, G. H. 1977, *ApJ*, 217, 693
- Herbig, G. H. 2009, *AJ*, 138, 448
- Herbig, G. H., Petrov, P. P., & Duemmler, R. 2003, *ApJ*, 595, 384
- Herbst, E. & van Dishoeck, E. F. 2009, *ARA&A*, 47, 427
- Hillenbrand, L. A., Contreras Peña, C., Morrell, S., et al. 2018, *ApJ*, 869, 146
- Hirahara, Y., Suzuki, H., Yamamoto, S., et al. 1992, *ApJ*, 394, 539
- Hogerheijde, M. R., van Dishoeck, E. F., Salverda, J. M., & Blake, G. A. 1999, *ApJ*, 513, 350
- Jørgensen, J. K., Belloche, A., & Garrod, R. T. 2020, *ARA&A*, 58, 727
- Kenyon, S. J. & Hartmann, L. W. 1991, *ApJ*, 383, 664
- Klein, B., Philipp, S. D., Krämer, I., et al. 2006, *A&A*, 454, L29
- Kóspál, Á. 2011, *A&A*, 535, A125
- Kóspál, Á., Abraham, P., Acosta-Pulido, J. A., et al. 2016, *A&A*, 596, A52
- Kóspál, Á., Abraham, P., Csengeri, T., et al. 2017a, *ApJ*, 836, 226
- Kóspál, Á., Abraham, P., Westhues, C., & Haas, M. 2017b, *A&A*, 597, L10
- Kóspál, Á., Szabó, Z. M., Abraham, P., et al. 2020, *The Astrophysical Journal*, 889, 148
- Kraus, S., Caratti o Garatti, A., Garcia-Lopez, R., et al. 2016, *MNRAS*, 462, L61
- Langer, W. D., Velusamy, T., Kuiper, T. B. H., et al. 1995, *ApJ*, 453, 293
- Lee, J.-E., Kim, C.-H., Lee, S., et al. 2024, *ApJ*, 966, 119
- Lee, J.-E., Lee, S., Baek, G., et al. 2019, *Nature Astronomy*, 3, 314
- Leemker, M., van't Hoff, M. L. R., Trapman, L., et al. 2021, *A&A*, 646, A3
- Levreault, R. M. 1988, *ApJS*, 67, 283
- Liu, H. B., Dunham, M. M., Pascucci, I., et al. 2018, *A&A*, 612, A54
- Lo, K. Y. & Bechis, K. P. 1973, *ApJ*, 185, L71
- Lo, K. Y. & Bechis, K. P. 1974, in *Bulletin of the American Astronomical Society*, Vol. 6, 221
- Looney, L. W., Mundy, L. G., & Welch, W. J. 1997, *ApJ*, 484, L157
- Magakian, T. Y., Nikogossian, E. H., Movsessian, T., et al. 2013, *MNRAS*, 432, 2685
- Marchand, P., Coutens, A., Scigliuto, J., et al. 2024, *A&A*, 687, A195
- Maret, S., Hily-Blant, P., Pety, J., Bardeau, S., & Reynier, E. 2011, *A&A*, 526, A47
- McMurdock, S., Blake, G. A., & Sargent, A. I. 1995, *AJ*, 110, 354
- Mercimek, S., Codella, C., Podio, L., et al. 2022, *A&A*, 659, A67
- Molyarova, T., Akimkin, V., Semenov, D., et al. 2018, *ApJ*, 866, 46
- Müller, H. S. P., Schlöder, F., Stutzki, J., & Winnewisser, G. 2005, *Journal of Molecular Structure*, 742, 215
- Müller, H. S. P., Thorwirth, S., Roth, D. A., & Winnewisser, G. 2001, *A&A*, 370, L49
- Nagy, Z., Abraham, P., Kóspál, Á., et al. 2022, *MNRAS*, 515, 1774
- Nagy, Z., Park, S., Abraham, P., et al. 2023, *MNRAS*, 524, 3344
- Nogueira, P. H., Zurlo, A., Pérez, S., et al. 2023, *MNRAS*, 523, 4970
- Park, S., Lee, J.-E., Pyo, T.-S., et al. 2020, *ApJ*, 900, 36
- Pety, J. 2005, in *SF2A-2005: Semaine de l'Astrophysique Française*, ed. F. Casoli, T. Contini, J. M. Hameury, & L. Pagani, 721
- Pickett, H. M., Poynter, R. L., Cohen, E. A., et al. 1998, *J. Quant. Spectr. Rad. Transf.*, 60, 883
- Plambeck, R. L. & Menten, K. M. 1990, *ApJ*, 364, 555
- Plunkett, A. L., Arce, H. G., Mardones, D., et al. 2015, *Nature*, 527, 70
- Quanz, S. P., Henning, T., Bouwman, J., Linz, H., & Lahuis, F. 2007, *ApJ*, 658, 487
- Rab, C., Elbakyan, V., Vorobyov, E., et al. 2017, *A&A*, 604, A15
- Ruíz-Rodríguez, D., Cieza, L. A., Williams, J. P., et al. 2017a, *MNRAS*, 468, 3266
- Ruíz-Rodríguez, D., Cieza, L. A., Williams, J. P., et al. 2017b, *MNRAS*, 466, 3519

- Ruíz-Rodríguez, D. A., Williams, J. P., Kastner, J. H., et al. 2022, MNRAS, 515, 2646
- Sandell, G. & Weintraub, D. A. 2001, ApJS, 134, 115
- Schmalzl, M., Kainulainen, J., Quanz, S. P., et al. 2010, ApJ, 725, 1327
- Shirley, Y. L. 2015, PASP, 127, 299
- Stäuber, P., Benz, A. O., Jørgensen, J. K., et al. 2007, A&A, 466, 977
- Szabó, Z. M., Gong, Y., Menten, K. M., et al. 2023a, A&A, 672, A158
- Szabó, Z. M., Gong, Y., Yang, W., et al. 2023b, A&A, 674, A202
- Szabó, Z. M., Kóspál, Á., Ábrahám, P., et al. 2021, ApJ, 917, 80
- Szabó, Z. M., Kóspál, Á., Ábrahám, P., et al. 2022, ApJ, 936, 64
- Szegedi-Elek, E., Ábrahám, P., Wyrzykowski, L., et al. 2020, ApJ, 899, 130
- Takagi, Y., Honda, S., Arai, A., et al. 2018, AJ, 155, 101
- Tobin, J. J., van't Hoff, M. L. R., Leemker, M., et al. 2023, Nature, 615, 227
- van 't Hoff, M. L. R., Tobin, J. J., Trapman, L., et al. 2018, ApJ, 864, L23
- Velilla Prieto, L., Sánchez Contreras, C., Cernicharo, J., et al. 2017, A&A, 597, A25
- Visser, R., Bergin, E. A., & Jørgensen, J. K. 2015, A&A, 577, A102
- Wachmann, A. 1954, ZAp, 35, 74
- Welin, G. 1971a, A&A, 12, 312
- Welin, G. 1971b, Information Bulletin on Variable Stars, 581, 1
- Wendeborn, J., Espaillat, C. C., Macías, E., et al. 2020, ApJ, 897, 54
- White, G. J., Fridlund, C. W. M., Bergman, P., et al. 2006, ApJ, 651, L41
- Winnberg, A., Graham, D., Walmsley, C. M., & Booth, R. S. 1981, A&A, 93, 79
- Woitke, P., Kamp, I., & Thi, W. F. 2009, A&A, 501, 383
- Woitke, P., Min, M., Pinte, C., et al. 2016, A&A, 586, A103
- Yamamoto, S. 2017, Introduction to Astrochemistry: Chemical Evolution from Interstellar Clouds to Star and Planet Formation
- Yamato, Y., Notsu, S., Aikawa, Y., et al. 2024, AJ, 167, 66
- Yang, W., Gong, Y., Menten, K. M., et al. 2023, A&A, 675, A112
- Zhou, W., Chen, Z., Jiang, Z., Feng, H., & Jiang, Y. 2024, ApJ, 969, L6
- Zucker, C., Speagle, J. S., Schlafly, E. F., et al. 2019, ApJ, 879, 125
- Zwicky, L., Molyarova, T., Akimkin, V., et al. 2024, MNRAS, 527, 7652

## Appendix A: Line detection

In Tables [A.1](#) and [A.2](#), we list the lines detected above  $3\sigma$ , with their respective quantum numbers, upper energy levels, Einstein coefficients, and the Gaussian fit results for the IRAM 30-m and the APEX 12-m telescopes, respectively. The lines detected in the 30-m survey are presented in Figs. [A.1–A.9](#). In certain tunings contamination from the image band cause false signal. These occurrences are labelled in red indicating rest frequency and peak temperature in the image band. An artifact is labelled on Fig. [A.7](#) around  $\sim 222.7$  GHz, which does not show similarities to any of the line profiles detected (i.e. extremely narrow). Lines are labeled in red and marked as unidentified ( $\sim 15$  lines in the 30-m spectrum) where we have a  $\geq 3\sigma$  detection but line identification does not match anything in the databases. Lines detected in the other selected frequencies covered with the APEX telescope are shown in Figs. [A.10](#) and [A.11](#).

Table A.1: Lines detected toward V1057 Cyg with the IRAM 30-m telescope

Rest frequency (GHz)	Molecule	Quantum numbers	$E_{\text{up}}^{(a)}$ (K)	$\log_{10} A_{ij}^{(b)}$ ( $\text{s}^{-1}$ )	$v_{\text{LSR}}^{(*)}$ ( $\text{km s}^{-1}$ )	$\Delta v^{(*)}$ ( $\text{km s}^{-1}$ )	$T_{\text{MB}}^{(*)}$ (K)	rms (mK)	Blended? (Y/N)
Tuning: 73 GHz									
72.039	DCO <sup>+</sup>	$J = 1 - 0, F = 0 - 1$	3.5	-4.65	4.28 (0.01)	1.12 (0.06)	0.45 (0.01)	10.50	N
72.413	DCN	$J = 1 - 0, F = 1 - 1$	3.5	-4.88	4.21 (0.06)	0.81 (0.10)	0.12 (0.01)	15.30	N
72.414	DCN	$J = 1 - 0, F = 2 - 1$	3.5	-4.88	4.13 (0.12)	1.01 (0.15)	0.12 (0.01)	15.30	N
72.783	HC <sub>3</sub> N	$J = 8 - 7$	15.7	-4.53	4.24 (0.02)	1.15 (0.04)	0.34 (0.05)	10.08	N
72.837	H <sub>2</sub> CO	1(0, 1) - 0(0, 0)	3.5	-5.08	4.16 (0.01)	0.81 (0.01)	0.49 (0.01)	10.68	N
76.117	C <sub>4</sub> H	$N = 8 - 7, J = 17/2 - 15/2$	16.4	-4.97	4.20 (0.16)	2.27 (0.41)	0.02 (0.01)	5.24	Y
76.117	C <sub>4</sub> H	$N = 8 - 7, J = 17/2 - 15/2$	16.4	-4.97					Y
76.156	C <sub>4</sub> H	$N = 8 - 7, J = 15/2 - 13/2$	16.5	-4.97					Y
76.156	C <sub>4</sub> H	$N = 8 - 7, J = 15/2 - 13/2$	16.5	-4.97	4.50 (0.14)	1.50 (0.35)	0.03 (0.01)	5.31	Y
76.305	DNC	$J = 1 - 0$	3.7	-4.79	4.32 (0.02)	1.56 (0.05)	0.22 (0.01)	5.87	N
77.107	N <sub>2</sub> D <sup>+</sup>	$J = 1 - 0$	3.7	-4.68	4.68 (0.17)	1.18 (0.45)	0.03 (0.01)	5.69	N
77.109	N <sub>2</sub> D <sup>+</sup>	$J = 1 - 0$	3.7	-4.68	4.49 (0.17)	2.17 (0.34)	0.03 (0.01)	3.59	N
77.731	CCS	$N = 6 - 5, J = 6 - 5$	21.8	-4.69	4.07 (0.26)	3.43 (0.64)	0.03 (0.01)	5.91	N
86.670	HCO	1(0, 1) - 0(0, 0), $J = 3/2 - 1/2$	4.2	-5.32	4.45 (0.12)	1.49 (0.28)	0.02 (0.01)	3.19	N
86.708	HCO	1(0, 1) - 0(0, 0), $J = 3/2 - 1/2$	4.2	-5.33	4.27 (0.21)	1.96 (0.53)	0.02 (0.01)	4.32	N
86.754	H <sup>13</sup> CO <sup>+</sup>	$J = 1 - 0$	4.2	-4.41	4.13 (0.01)	1.42 (0.01)	0.48 (0.01)	3.91	N
87.090	HN <sup>13</sup> C	$J = 1 - 0$	4.2	-4.62	4.37 (0.04)	1.46 (0.09)	0.08 (0.01)	3.92	N
87.284	CCH	$N = 1 - 0, J = 3/2 - 1/2$	4.2	-6.58	4.17 (0.02)	1.47 (0.07)	0.11 (0.01)	3.65	N
87.316	CCH	$N = 1 - 0, J = 3/2 - 1/2$	4.2	-5.81	4.18 (0.01)	1.38 (0.02)	0.75 (0.01)	5.62	N
87.328	CCH	$N = 1 - 0, J = 3/2 - 1/2$	4.2	-5.89	4.16 (0.01)	1.35 (0.02)	0.42 (0.12)	3.79	N
87.402	CCH	$N = 1 - 0, J = 1/2 - 1/2$	4.2	-5.89	4.17 (0.04)	1.32 (0.10)	0.43 (0.02)	33.94	N
87.407	CCH	$N = 1 - 0, J = 1/2 - 1/2$	4.2	-5.81	4.21 (0.20)	1.29 (0.39)	0.18 (0.09)	72.50	N
87.446	CCH	$N = 1 - 0, J = 1/2 - 1/2$	4.2	-6.58	4.15 (0.02)	1.46 (0.05)	0.11 (0.01)	3.06	N
87.925	HNCO	4(0, 4) - 3(0, 3)	10.5	-5.05	3.53 (0.08)	1.10 (0.14)	0.03 (0.01)	3.36	N
88.630	HCN	$J = 1 - 0$	4.3	-4.61	4.21 (0.17)	1.41 (0.43)	0.57 (0.15)	3.48	N
88.631	HCN	$J = 1 - 0$	4.3	-4.61	4.26 (0.05)	1.38 (0.13)	1.07 (0.09)	3.97	N
88.633	HCN	$J = 1 - 0$	4.3	-4.61	4.26 (0.28)	1.27 (0.75)	0.34 (0.18)	98.23	N
89.188	HCO <sup>+</sup>	$J = 1 - 0$	4.3	-4.37	4.25 (0.01)	1.46 (0.01)	2.26 (0.01)	3.77	N
90.663	HNC	$J = 1 - 0$	4.4	-4.57	4.30 (0.01)	1.45 (0.01)	1.59 (0.01)	10.08	N
90.979	HC <sub>3</sub> N	$J = 10 - 9$	24	-4.23	4.36 (0.02)	1.37 (0.05)	0.26 (0.01)	9.21	N
92.494	<sup>13</sup> CS	$J = 2 - 1$	6.7	-4.85	3.89 (0.33)	2.26 (0.87)	0.02 (0.01)	9.76	N
93.171	N <sub>2</sub> H <sup>+</sup>	$J = 1 - 0$	4.5	-4.44	4.11 (0.14)	1.45 (0.36)	0.47 (0.10)	24.52	N
93.173	N <sub>2</sub> H <sup>+</sup>	$J = 1 - 0$	4.5	-4.44	4.25 (0.09)	2.07 (0.20)	0.60 (0.98)	9.06	N
93.176	N <sub>2</sub> H <sup>+</sup>	$J = 1 - 0$	4.5	-4.44	3.97 (0.20)	0.77 (0.70)	0.25 (0.99)	9.21	N
93.870	CCS	$N = 7 - 6, J = 8 - 7$	19.9	-4.42	4.44 (0.12)	0.96 (0.21)	0.05 (0.01)	9.65	N
Tuning: 80 GHz									
81.505	CCS	$N = 6 - 5, J = 7 - 6$	15.4	-4.61	4.16 (0.02)	1.34 (0.06)	0.08 (0.01)	3.29	N
81.881	HC <sub>3</sub> N	$J = 9 - 8$	19.6	-4.37	4.26 (0.01)	1.53 (0.01)	0.27 (0.01)	2.59	N
82.093	c-C <sub>3</sub> H <sub>2</sub>	2(0, 2) - 1(1, 1)	6.4	-4.72	4.25 (0.01)	1.48 (0.04)	0.12 (0.01)	2.99	N
82.966	c-C <sub>3</sub> H <sub>2</sub>	3(1, 2) - 3(0, 3)	16	-5.00	4.26 (0.03)	1.30 (0.08)	0.05 (0.01)	2.21	Y
84.521	CH <sub>3</sub> OH	$5_{-1} - 4_0, E$	40.4	-5.71	4.31 (0.07)	1.60 (0.18)	0.03 (0.01)	3.57	N
84.727	c-C <sub>3</sub> H <sub>2</sub>	3(2, 2) - 3(1, 3)	16.1	-4.98	4.17 (0.12)	1.15 (0.18)	0.02 (0.01)	3.22	N
85.162	HC <sup>18</sup> O <sup>+</sup>	$J = 1 - 0$	4.1	-4.43	4.16 (0.04)	1.48 (0.11)	0.05 (0.01)	2.91	N
85.338	c-C <sub>3</sub> H <sub>2</sub>	2(1, 2) - 1(0, 1)	6.4	-4.63	4.22 (0.01)	1.31 (0.02)	0.47 (0.01)	5.38	N
85.347	HCS <sup>+</sup>	$J = 2 - 1$	6.1	-4.95	4.20 (0.07)	1.22 (0.19)	0.03 (0.01)	3.72	N
85.455	CH <sub>3</sub> CCH	5(1) - 4(1)	19.5	-5.71	4.11 (0.12)	1.20 (0.31)	0.03 (0.01)	4.07	N
85.457	CH <sub>3</sub> CCH	5(0) - 4(0)	12.3	-5.69	4.09 (0.09)	1.37 (0.21)	0.04 (0.01)	4.07	N
93.870	CCS	$N = 7 - 6, J = 8 - 7$	19.9	-4.42	4.31 (0.03)	1.18 (0.06)	0.06 (0.01)	3.26	N
95.150	C <sub>4</sub> H	$N = 10 - 9$	25.1	-4.67	4.36 (0.07)	1.32 (0.16)	0.02 (0.01)	3.04	Y
95.150	C <sub>4</sub> H	$N = 10 - 9$	25.1	-4.67					Y
95.188	C <sub>4</sub> H	$N = 10 - 9$	25.1	-4.68					Y
95.188	C <sub>4</sub> H	$N = 10 - 9$	25.1	-4.67	4.34 (0.09)	1.46 (0.30)	0.02 (0.01)	3.14	Y
96.412	C <sup>34</sup> S	$J = 2 - 1$	6.9	-4.79	4.21 (0.01)	1.41 (0.04)	0.11 (0.01)	3.15	N
96.739	CH <sub>3</sub> OH	2(1, 2) - 1(1, 1) E	12.5	-4.59	4.08 (0.13)	1.43 (0.31)	0.17 (0.03)	7.20	N
96.741	CH <sub>3</sub> OH	2(0, 2) - 1(0, 1) A	7.0	-5.46	4.08 (0.06)	1.45 (0.15)	0.25 (0.02)	2.95	N
96.744	CH <sub>3</sub> OH	2(-0, 2) - 1(-0, 1) E	20.1	-5.46	4.07 (0.60)	0.97 (1.57)	0.04 (0.05)	30.24	N
97.172	C <sup>33</sup> S	$J = 2 - 1$	7.0	-4.78	4.56 (0.14)	1.93 (0.30)	0.02 (0.01)	2.93	N
97.980	CS	$J = 2 - 1$	7.1	-4.77	4.25 (0.01)	1.39 (0.01)	1.61 (0.01)	4.37	N
99.299	SO	$J = 2 - 1$	9.2	-4.94	4.17 (0.01)	1.23 (0.02)	0.27 (0.01)	4.14	N
99.866	CCS	$N = 8 - 7, J = 7 - 6$	28.1	-4.35	4.33 (0.08)	1.08 (0.24)	0.02 (0.01)	3.28	N
100.076	HC <sub>3</sub> N	$J = 11 - 10$	28.8	-4.11	4.28 (0.01)	1.14 (0.02)	0.25 (0.01)	4.02	N
Tuning: 90 GHz off (spectrum towards the source position, i.e. (0'', 0''))									
88.630	HCN	$J = 1 - 0$	4.3	-4.61	4.06 (0.17)	1.46 (0.40)	0.10 (0.02)	10.36	N
88.631	HCN	$J = 1 - 0$	4.3	-4.62	3.32 (0.07)	1.19 (0.20)	0.15 (0.02)	11.34	N



Table A.1: continued.

Rest frequency (GHz)	Molecule	Quantum numbers	$E_{up}^{(a)}$ (K)	$\log_{10} A_{ij}^{(b)}$ ( $s^{-1}$ )	$v_{LSR}^{(*)}$ ( $km\ s^{-1}$ )	$\Delta v^{(*)}$ ( $km\ s^{-1}$ )	$T_{MB}^{(*)}$ (K)	rms (mK)	Blended? (Y/N)
88.633	HCN	$J = 1 - 0$	4.3	-4.61	4.35 (0.28)	0.75 (0.77)	0.08 (0.03)	20.04	N
89.188	HCO <sup>+</sup>	$J = 1 - 0$	4.3	-4.37	4.18 (0.03)	1.53 (0.07)	0.23 (0.01)	10.60	N
90.663	HNC	$J = 1 - 0$	4.4	-4.57	4.12 (0.04)	1.51 (0.11)	0.19 (0.01)	11.58	N
90.979	HC <sub>3</sub> N	$J = 10 - 9$	24.0	-4.23	4.29 (0.08)	0.65 (0.10)	0.09 (0.01)	12.14	N
93.171	N <sub>2</sub> H <sup>+</sup>	$J = 1 - 0$	4.5	-4.44	4.05 (0.17)	1.42 (0.38)	0.03 (0.01)	6.85	N
93.173	N <sub>2</sub> H <sup>+</sup>	$J = 1 - 0$	4.5	-4.44	4.29 (0.20)	2.38 (0.38)	0.03 (0.01)	8.45	N
93.870	CCS	$N = 7 - 6, J = 8 - 7$	19.9	-4.42	4.29 (0.17)	1.10 (0.53)	0.02 (0.01)	7.73	N
109.782	C <sup>18</sup> O	$J = 1 - 0$	5.3	-7.02	4.09 (0.02)	1.07 (0.04)	0.35 (0.01)	11.89	N
110.201	<sup>13</sup> CO	$J = 1 - 0$	5.3	-7.19	3.86 (0.01)	1.80 (0.01)	2.36 (0.02)	13.47	N
Tuning: 94 GHz									
92.494	<sup>13</sup> CS	$J = 2 - 1$	6.7	-4.85	4.12 (0.08)	1.26 (0.19)	0.04 (0.01)	5.21	N
93.171	N <sub>2</sub> H <sup>+</sup>	$J = 1 - 0$	4.5	-4.44	4.09 (0.09)	1.36 (0.25)	0.55 (0.08)	6.29	N
93.173	N <sub>2</sub> H <sup>+</sup>	$J = 1 - 0$	4.5	-4.44	4.22 (0.07)	1.92 (0.16)	0.71 (0.01)	6.29	N
93.176	N <sub>2</sub> H <sup>+</sup>	$J = 1 - 0$	4.5	-4.44	3.91 (0.21)	1.03 (0.46)	0.27 (0.01)	6.29	N
93.870	CCS	$N = 7 - 6, J = 8 - 7$	19.9	-4.42	4.36 (0.02)	0.86 (0.14)	0.08 (0.01)	4.53	N
95.150	C <sub>4</sub> H	$N = 10 - 9$	25.1	-5.41	4.32 (0.08)	0.97 (0.14)	0.03 (0.01)	4.49	Y
95.150	C <sub>4</sub> H	$N = 10 - 9$	25.1	-5.41					Y
96.412	C <sup>34</sup> S	$J = 2 - 1$	6.9	-5.41	4.14 (0.01)	1.41 (0.03)	0.11 (0.01)	2.46	N
96.739	CH <sub>3</sub> OH	$2(1, 2) - 1(1, 1) E$	12.5	-5.59	4.04 (0.10)	1.48 (0.24)	0.18 (0.01)	5.83	N
96.741	CH <sub>3</sub> OH	$2(0, 2) - 1(0, 1) A$	7.0	-5.46	4.06 (0.05)	1.45 (0.12)	0.27 (0.01)	2.42	N
96.744	CH <sub>3</sub> OH	$2(-0, 2) - 1(-0, 1) E$	20.1	-5.46	4.10 (0.49)	1.24 (1.02)	0.04 (0.01)	2.25	N
97.172	C <sup>33</sup> S	$J = 2 - 1$	7.0	-4.78	4.80 (0.09)	1.33 (0.21)	0.02 (0.01)	2.95	N
97.980	CS	$J = 2 - 1$	7.1	-4.77	4.17 (0.01)	1.49 (0.01)	1.52 (0.01)	2.68	N
99.299	SO	$J = 3 - 2$	9.2	-4.94	4.04 (0.01)	1.45 (0.01)	0.27 (0.01)	2.93	N
108.651	<sup>13</sup> CN	$N = 1 - 0, J = 1/2 - 1/2$	5.2	-5.01	4.16 (0.11)	1.24 (0.25)	0.02 (0.01)	3.72	N
108.780	<sup>13</sup> CN	$N = 1 - 0, J = 3/2 - 1/2$	5.2	-4.97	4.13 (0.06)	1.01 (0.13)	0.03 (0.01)	3.39	N
108.893	CH <sub>3</sub> OH	$0(0, 0) - 1(-1, 1) E$	13.1	-4.83	4.05 (0.03)	1.44 (0.07)	0.05 (0.01)	2.82	N
109.173	HC <sub>3</sub> N	$J = 12 - 11$	34.1	-3.99	2.45 (0.01)	1.13 (0.01)	0.21 (0.01)	2.47	N
109.252	SO	$2(3) - 1(2)$	21.1	-3.97	3.68 (0.05)	1.53 (0.15)	0.03 (0.01)	2.73	N
109.782	C <sup>18</sup> O	$J = 1 - 0$	5.3	-7.20	4.14 (0.01)	0.99 (0.01)	1.12 (0.01)	2.84	N
109.905	HNCO	$5(0, 5) - 4(0, 4)$	15.8	-4.75	4.19 (0.10)	1.61 (0.22)	0.02 (0.01)	3.34	N
110.153	NH <sub>2</sub> D	$1(1, 1)0 - 1(0, 1)0$	21.3	-4.78	4.46 (0.07)	1.97 (0.28)	0.04 (0.01)	3.16	N
110.201	<sup>13</sup> CO	$J = 1 - 0$	5.3	-7.19	3.02 (0.01)	1.51 (0.01)	5.66 (0.01)	2.48	N
110.381	CH <sub>3</sub> CN	$6(1) - 5(1)$	25.7	-3.96	4.15 (0.14)	1.41 (0.31)	0.02 (0.01)	2.99	N
110.383	CH <sub>3</sub> CN	$6(0) - 5(0)$	18.5	-3.95	3.76 (0.17)	1.66 (0.41)	0.01 (0.01)	3.02	N
112.358	C <sup>17</sup> O	$J = 1 - 0$	5.4	-7.17	3.72 (0.03)	1.29 (0.08)	0.21 (0.01)	4.81	N
112.360	C <sup>17</sup> O	$J = 1 - 0$	5.4	-7.17	4.20 (0.12)	1.13 (0.31)	0.12 (0.01)	5.07	N
113.123	CN	$N = 1 - 0, J = 1/2 - 1/2$	5.4	-5.88	4.26 (0.02)	1.01 (0.05)	0.15 (0.01)	5.93	N
113.144	CN	$N = 1 - 0, J = 1/2 - 1/2$	5.4	-5.97	4.28 (0.01)	1.15 (0.05)	0.56 (0.01)	5.42	N
113.170	CN	$N = 1 - 0, J = 1/2 - 1/2$	5.4	-5.28	4.21 (0.01)	1.16 (0.01)	0.56 (0.01)	5.35	N
113.191	CN	$N = 1 - 0, J = 1/2 - 1/2$	5.4	-5.17	4.22 (0.01)	1.13 (0.01)	0.63 (0.01)	4.68	N
113.488	CN	$N = 1 - 0, J = 3/2 - 1/2$	5.4	-5.17	4.24 (0.10)	1.09 (0.24)	0.65 (0.14)	56.14	N
113.490	CN	$N = 1 - 0, J = 3/2 - 1/2$	5.4	-4.92	4.30 (0.04)	1.05 (0.07)	1.26 (0.12)	84.52	N
113.499	CN	$N = 1 - 0, J = 3/2 - 1/2$	5.4	-4.97	4.27 (0.15)	1.04 (0.32)	0.49 (0.22)	160	N
113.508	CN	$N = 1 - 0, J = 3/2 - 1/2$	5.4	-5.28	4.29 (0.04)	0.99 (0.10)	0.59 (0.07)	56.98	N
113.520	CN	$N = 1 - 0, J = 3/2 - 1/2$	5.4	-5.88	4.31 (0.22)	0.92 (0.59)	0.13 (0.08)	65.04	N
115.271	CO	$J = 1 - 0$	5.5	-7.14	...	...	...	...	...
Tuning: 133 GHz									
131.551	CCS	$N = 10 - 9, J = 11 - 10$	37.0	-3.97	3.67 (0.18)	1.54 (0.49)	0.03 (0.03)	6.62	N
134.284	HD <sub>2</sub> CO	$2(1, 1) - 1(1, 0)$	17.6	-4.33	3.90 (0.05)	0.99 (0.12)	0.07 (0.01)	7.15	N
135.298	H <sub>2</sub> CS	$4(1, 4) - 3(1, 3)$	29.9	-4.48	3.93 (0.04)	1.53 (0.15)	0.05 (0.01)	4.82	N
136.464	HC <sub>3</sub> N	$J = 15 - 14$	52.4	-3.70	4.08 (0.01)	1.17 (0.04)	0.12 (0.01)	3.92	N
136.725	CH <sub>3</sub> CCH	$8(1) - 7(1)$	36.8	-5.07	4.12 (0.09)	0.95 (0.19)	0.04 (0.01)	5.24	N
136.728	CH <sub>3</sub> CCH	$8(0) - 7(0)$	29.5	-5.05	3.95 (0.11)	1.68 (0.31)	0.04 (0.01)	5.76	N
137.371	H <sub>2</sub> CS	$4(0, 4) - 3(0, 3)$	16.5	-4.43	4.28 (0.06)	1.33 (0.18)	0.04 (0.01)	4.29	N
137.449	H <sub>2</sub> <sup>13</sup> CO	$2(1, 2) - 1(1, 1)$	21.7	-4.30	3.95 (0.08)	1.67 (0.25)	0.03 (0.01)	4.29	N
138.178	SO	$4(3) - 3(2)$	15.9	-4.49	3.96 (0.01)	1.38 (0.02)	0.24 (0.01)	4.78	N
146.635	H <sub>2</sub> <sup>13</sup> CO	$2(1, 1) - 1(1, 0)$	22.4	-4.22	4.11 (0.10)	1.24 (0.20)	0.03 (0.01)	7.04	N
146.969	CS	$J = 3 - 2$	7	-4.21	4.18 (0.01)	1.26 (0.01)	1.70 (0.01)	6.87	N
150.436	c-C <sub>3</sub> H <sub>2</sub>	$2(2, 0) - 1(1, 1)$	9.7	-4.22	4.20 (0.04)	1.03 (0.11)	0.08 (0.01)	8.78	N
150.498	H <sub>2</sub> CO	$2(1, 1) - 1(1, 0)$	22.6	-4.18	4.12 (0.01)	1.18 (0.01)	1.41 (0.01)	10.81	N
150.820	c-C <sub>3</sub> H <sub>2</sub>	$4(0, 4) - 3(1, 3)$	19.3	-3.74	4.19 (0.02)	0.93 (0.05)	0.17 (0.01)	10.44	N
150.851	c-C <sub>3</sub> H <sub>2</sub>	$4(1, 4) - 3(0, 3)$	19.3	-3.74	4.23 (0.01)	0.97 (0.02)	0.41 (0.01)	9.89	N
152.609	DNC	$J = 2 - 1$	11.0	-3.81	4.32 (0.01)	0.97 (0.03)	0.34 (0.01)	9.61	N
153.814	CH <sub>3</sub> CCH	$9(1) - 8(1)$	44.1	-4.95	4.28 (0.16)	1.36 (0.31)	0.04 (0.01)	9.94	N

Table A.1: continued.

Rest frequency (GHz)	Molecule	Quantum numbers	$E_{up}^{(a)}$ (K)	$\log_{10} A_{ij}^{(b)}$ ( $s^{-1}$ )	$v_{LSR}^{(*)}$ ( $km\ s^{-1}$ )	$\Delta v^{(*)}$ ( $km\ s^{-1}$ )	$T_{MB}^{(*)}$ (K)	rms (mK)	Blended? (Y/N)
153.817	CH <sub>3</sub> CCH	9(0) – 8(0)	36.9	-4.94	4.12 (0.09)	1.01 (0.21)	0.05 (0.01)	9.14	N
Tuning: 141 GHz									
138.739	<sup>13</sup> CS	$J = 3 - 2$	13.3	-4.29	4.34 (0.09)	1.18 (0.20)	0.04 (0.0)	7.71	N
139.483	H <sub>2</sub> CS	4(1, 3) – 3(1, 2)	29.9	-4.44	4.36 (0.07)	1.18 (0.16)	0.05 (0.01)	7.11	N
140.839	H <sub>2</sub> CO	2(1, 2) – 1(1, 1)	21.9	-4.27	4.08 (0.01)	1.17 (0.01)	1.70 (0.01)	7.76	N
144.077	DCO <sup>+</sup>	$J = 2 - 1$	10.4	-3.67	4.21 (0.01)	1.01 (0.01)	0.71 (0.01)	4.00	N
144.241	CCD	$N = 2 - 1, J = 5/2 - 3/2$	10.4	-5.08	4.17 (0.09)	1.35 (0.45)	0.04 (0.01)	4.45	N
144.242	CCD	$N = 2 - 1, J = 5/2 - 3/2$	10.4	-5.20	4.06 (0.06)	1.14 (0.18)	0.05 (0.01)	4.41	N
144.244	CCS	$N, J = 11, 12 - 10, 11$	43.9	-3.85	4.20 (0.21)	0.97 (0.49)	0.02 (0.01)	4.17	N
144.296	CCD	$N = 2 - 1, J = 3/2 - 1/2$	10.4	-5.17	3.73 (0.17)	2.75 (0.43)	0.03 (0.01)	4.18	N
144.376	CCD	$N = 2 - 1, J = 3/2 - 3/2$	10.4	-5.42	4.38 (0.10)	0.91 (0.25)	0.02 (0.01)	4.59	N
144.617	C <sup>34</sup> S	3 – 2	13.9	-4.23	4.14 (0.02)	1.33 (0.05)	0.10 (0.01)	4.20	N
144.826	DCN	$J = 2 - 1, F = 2 - 2$	10.4	-4.50	3.93 (0.05)	1.23 (0.14)	0.03 (0.01)	3.52	Y
144.826	DCN	$J = 2 - 1, F = 1 - 0$	10.4	-4.15					Y
144.828	DCN	$J = 2 - 1, F = 2 - 1$	10.4 <sub>s</sub>	-3.89	4.05 (0.02)	1.15 (0.05)	0.13 (0.01)	3.367	N
145.089	c-C <sub>3</sub> H <sub>2</sub>	3(1, 2) – 2(2, 1)	16.0	-4.16	4.18 (0.13)	0.95 (0.70)	0.21 (0.06)	70.95	N
145.093	CH <sub>3</sub> OH	3(-0, 3) – 2(-0, 2) <i>E</i>	27.1	-4.91	3.99 (0.50)	1.07 (1.00)	0.06 (0.07)	57.56	N
145.097	CH <sub>3</sub> OH	3(1, 3) – 2(1, 2) <i>E</i>	19.5	-4.95	4.00 (0.10)	1.23 (0.23)	0.27 (0.06)	33.63	N
145.103	CH <sub>3</sub> OH	3(0, 3) – 2(0, 2) <i>A</i>	13.9	-4.91	4.01 (0.05)	1.07 (0.09)	0.34 (0.06)	46.30	N
145.126	CH <sub>3</sub> OH	3(-2, 2) – 2(-2, 1) <i>E</i>	36.2	-5.16	3.84 (0.12)	1.54 (0.41)	0.03 (0.01)	4.42	Y
145.126	CH <sub>3</sub> OH	3(2, 1) – 2(2, 0) <i>E</i>	39.8	-5.16					Y
145.131	CH <sub>3</sub> OH	3(-1, 2) – 2(-1, 1) <i>E</i>	35.0	-4.95	3.96 (0.11)	1.40 (0.40)	0.03 (0.01)	6.31	N
145.560	HC <sub>3</sub> N	$J = 16 - 15$	59.4	-3.61	4.05 (0.02)	1.10 (0.04)	0.11 (0.01)	4.35	N
145.602	H <sub>2</sub> CO	2(0, 2) – 1(0, 1)	10.5	-4.10	4.08 (0.01)	1.23 (0.01)	1.16 (0.01)	4.19	N
146.368	CH <sub>3</sub> OH	3(1, 2) – 2(1, 1) <i>A</i>	28.6	-4.96	3.93 (0.10)	1.27 (0.22)	0.02 (0.01)	4.83	N
154.657	HC <sub>3</sub> N	$J = 17 - 16$	66.8	-3.53	4.07 (0.03)	1.25 (0.09)	0.10 (0.01)	7.04	N
155.518	c-C <sub>3</sub> H <sub>2</sub>	3(2, 2) – 2(1, 1)	16.1	-3.95	4.19 (0.02)	0.95 (0.06)	0.11 (0.01)	7.28	N
157.246	CH <sub>3</sub> OH	4(-0, 4) – 4(1, 4) <i>E</i>	36.3	-4.67	4.25 (0.10)	1.46 (0.23)	0.04 (0.01)	7.28	N
157.270	CH <sub>3</sub> OH	1(-0, 1) – 1(1, 1) <i>E</i>	15.4	-4.65	3.99 (0.06)	1.21 (0.14)	0.12 (0.01)	6.85	N
157.272	CH <sub>3</sub> OH	3(-0, 3) – 3(1, 3) <i>E</i>	27.1	-4.66	4.00 (0.16)	1.46 (0.63)	0.07 (0.02)	6.91	N
157.276	CH <sub>3</sub> OH	2(-0, 2) – 2(1, 2) <i>E</i>	20.1	-4.66	3.98 (0.08)	1.26 (0.21)	0.10 (0.02)	6.57	N
158.971	SO	3(4) – 2(3)	28.7	-4.37	4.12 (0.06)	1.80 (0.17)	0.07 (0.01)	7.01	N
Tuning: 202 GHz									
206.176	SO	4(5) – 3(4)	38.6	-3.99	4.11 (0.10)	1.54 (0.26)	0.13 (0.03)	26.15	N
216.112	DCO <sup>+</sup>	$J = 3 - 2$	20.7	-3.11	4.11 (0.01)	0.86 (0.02)	0.77 (0.03)	27.50	N
216.278	c-C <sub>3</sub> H <sub>2</sub>	3(3, 0) – 2(2, 1)	19.5	-3.59	4.12 (0.03)	0.97 (0.08)	0.27 (0.03)	23.81	N
216.372	CCD	$N = 3 - 2, J = 7/2 - 5/2$	20.8	-3.52					Y
216.373	CCD	$N = 3 - 2, J = 7/2 - 5/2$	20.8	-3.57	3.57 (0.10)	1.65 (0.24)	0.11 (0.03)	28.43	Y
216.373	CCD	$N = 3 - 2, J = 7/2 - 5/2$	20.8	-3.55					Y
217.238	DCN	$J = 3 - 2$	20.9	-3.33	4.15 (0.08)	1.09 (0.20)	0.12 (0.03)	24.58	N
217.822	c-C <sub>3</sub> H <sub>2</sub>	6(1, 6) – 5(0, 5)	38.6	-3.26	4.13 (0.03)	1.10 (0.08)	0.27 (0.03)	28.04	N
217.940	c-C <sub>3</sub> H <sub>2</sub>	5(1, 4) – 4(2, 3)	35.4	-3.39	4.15 (0.05)	0.91 (0.10)	0.17 (0.03)	25.74	N
218.222	H <sub>2</sub> CO	3(0, 3) – 2(0, 2)	21.0	-3.54	4.02 (0.01)	1.16 (0.02)	1.31 (0.03)	24.59	N
218.440	CH <sub>3</sub> OH	4(-2, 3) – 3(-1, 2) <i>E</i>	45.5	-3.32	3.91 (0.10)	0.98 (0.20)	0.09 (0.03)	26.27	N
219.560	C <sup>18</sup> O	$J = 2 - 1$	15.8	-6.22	4.07 (0.01)	1.09 (0.01)	3.69 (0.05)	32.17	N
219.560	H <sub>2</sub> CN	3(0, 3) – 2(0, 2)	21.1	-5.05	3.77 (0.14)	0.90 (0.42)	0.10 (0.04)	33.09	N
219.949	SO	6(5) – 5(4)	35.0	-3.87	4.14 (0.04)	1.23 (0.09)	0.29 (0.04)	33.54	N
220.398	<sup>13</sup> CO	$J = 2 - 1$	15.9	-6.21	4.13 (0.01)	1.55 (0.01)	8.75 (0.11)	30.68	N
Tuning: 210 GHz									
211.211	H <sub>2</sub> CO	3(1, 3) – 2(1, 2)	32.1	-3.64	4.13 (0.01)	1.07 (0.02)	2.048 (0.06)	44.13	N
212.928	H <sub>2</sub> CN	3(1, 3) – 2(1, 2)	32.3	-3.68	3.92 (0.15)	1.29 (0.36)	0.09 (0.04)	34.86	N
224.714	C <sup>17</sup> O	$J = 2 - 1$	16.2	-6.34	4.77 (0.01)	1.47 (0.04)	1.04 (0.04)	29.31	N
225.697	H <sub>2</sub> CO	3(1, 2) – 2(1, 1)	33.4	-3.55	4.09 (0.01)	1.12 (0.01)	1.78 (0.04)	29.47	N
226.298	CN	$N = 2 - 1, J = 3/2 - 3/2$	16.3	-5.08	4.53 (0.14)	1.00 (0.23)	0.09 (0.04)	31.07	N
226.303	CN	$N = 2 - 1, J = 3/2 - 3/2$	16.3	-5.37	4.03 (0.06)	0.48 (0.17)	0.13 (0.05)	34.72	N
226.314	CN	$N = 2 - 1, J = 3/2 - 3/2$	16.3	-5.00	4.09 (0.07)	0.76 (0.17)	0.13 (0.04)	36.27	N
226.359	CN	$N = 2 - 1, J = 3/2 - 3/2$	16.3	-4.79	4.11 (0.04)	1.06 (0.09)	0.26 (0.04)	29.72	N
226.632	CN	$N = 2 - 1, J = 3/2 - 1/2$	16.3	-4.37	4.11 (0.02)	0.92 (0.05)	0.40 (0.04)	31.92	N
226.659	CN	$N = 2 - 1, J = 3/2 - 1/2$	16.3	-4.02	4.13 (0.02)	1.02 (0.06)	0.91 (0.09)	71.64	N
226.663	CN	$N = 2 - 1, J = 3/2 - 1/2$	16.3	-4.07	4.10 (0.15)	0.96 (0.33)	0.27 (0.13)	70.84	N
226.679	CN	$N = 2 - 1, J = 3/2 - 1/2$	16.3	-4.27	4.12 (0.05)	0.93 (0.11)	0.43 (0.11)	85.94	N
226.874	CN	$N = 2 - 1, J = 5/2 - 3/2$	16.3	-4.06	3.59 (0.02)	1.72 (0.06)	1.63 (0.09)	73.74	N
226.887	CN	$N = 2 - 1, J = 5/2 - 3/2$	16.3	-4.56	4.25 (0.26)	0.66 (0.45)	0.26 (0.36)	284	N
226.892	CN	$N = 2 - 1, J = 5/2 - 3/2$	16.3	-4.74	4.14 (0.27)	0.79 (0.47)	0.28 (0.36)	285	N
227.169	c-C <sub>3</sub> H <sub>2</sub>	4(3, 2) – 3(2, 1)	29.1	-3.51	4.20 (0.05)	0.86 (0.13)	0.18 (0.04)	29.02	N

Table A.1: continued.

Rest frequency (GHz)	Molecule	Quantum numbers	$E_{up}^{(a)}$ (K)	$\log_{10}A_{ij}^{(b)}$ ( $s^{-1}$ )	$v_{LSR}^{(*)}$ ( $km\ s^{-1}$ )	$\Delta v^{(*)}$ ( $km\ s^{-1}$ )	$T_{MB}^{(*)}$ (K)	rms (mK)	Blended? (Y/N)
228.910	DNC	$J = 3 - 2$	22.0	-3.25	4.18 (0.08)	1.05 (0.18)	0.16 (0.05)	41.83	N
230.538	CO	$J = 2 - 1$	16.6	-6.16	...	...	...	...	...
Tuning: 242 GHz									
241.767	CH <sub>3</sub> OH	$5(1, 5) - 4(1, 4) E$	40.4	-4.23	4.22 (0.14)	1.42 (0.47)	0.16 (0.08)	61.14	N
241.791	CH <sub>3</sub> OH	$5(0, 5) - 4(0, 4) A$	34.8	-4.21	4.08 (0.08)	1.01 (0.18)	0.19 (0.08)	57.21	N
244.935	CS	$J = 5 - 4$	35.3	-3.52	4.12 (0.01)	1.15 (0.02)	1.23 (0.05)	37.76	N
258.255	SO	$6(6) - 5(5)$	56.5	-3.66	4.24 (0.09)	1.26 (0.22)	0.18 (0.06)	45.20	N
260.255	H <sup>13</sup> CO <sup>+</sup>	$J = 3 - 2$	25.0	-2.87	4.05 (0.02)	0.93 (0.05)	0.84 (0.08)	63.97	N
261.805	CH <sub>3</sub> OH	$2(-1, 1) - 1(-0, 1) E$	28.0	-4.25	4.50 (0.11)	1.17 (0.28)	0.20 (0.08)	58.26	N
261.843	SO	$7(6) - 6(5)$	47.6	-3.64	4.06 (0.09)	1.20 (0.21)	0.22 (0.08)	61.15	N
262.004	CCH	$N = 3 - 2, J = 7/2 - 5/2$	25.1	-4.27	4.06 (0.03)	1.04 (0.07)	1.20 (0.13)	56.72	N
262.006	CCH	$N = 3 - 2, J = 7/2 - 5/2$	25.1	-4.29	4.12 (0.06)	1.13 (0.15)	0.85 (0.16)	53.22	N
262.064	CCH	$N = 3 - 2, J = 5/2 - 3/2$	25.2	-4.31	4.12 (0.03)	1.06 (0.08)	0.88 (0.11)	61.20	N
262.067	CCH	$N = 3 - 2, J = 7/2 - 5/2$	25.2	-4.34	4.09 (0.06)	0.98 (0.14)	0.67 (0.13)	58.27	N

**Notes.** <sup>(a)</sup> Upper energy level. <sup>(b)</sup> Einstein coefficient. <sup>(\*)</sup> Parameters from the Gaussian fit results, where the formal errors of the fits are given in parentheses. The rms is a result from the baseline fitting.

Table A.2: Lines detected toward V1057 Cyg with the APEX 12-m telescope.

Rest frequency (GHz)	Molecule	Quantum numbers	$E_{up}^{(a)}$ (K)	$\log_{10}A_{ij}^{(b)}$ ( $s^{-1}$ )	$v_{LSR}$ ( $km\ s^{-1}$ )	$\Delta v$ ( $km\ s^{-1}$ )	$T_{MB}$ (K)	rms (mK)	Blended? (Y/N)
Receiver: nFLASH230, Tuning: 219.2 GHz									
216.112	DCO <sup>+</sup>	$J = 3 - 2$	20.7	-3.11	4.31 (0.01)	0.76 (0.02)	0.36 (0.02)	18.45	N
216.278	c-C <sub>3</sub> H <sub>2</sub>	$3(3, 0) - 2(2, 1)$	19.5	-3.55	4.30 (0.04)	1.07 (0.09)	0.13 (0.02)	19.43	N
218.222	H <sub>2</sub> CO	$3(0, 3) - 2(0, 2)$	21.0	-3.54	4.09 (0.01)	1.26 (0.03)	0.38 (0.02)	20.38	N
217.822	c-C <sub>3</sub> H <sub>2</sub>	$6(0, 6) - 5(1, 5)$	38.6	-3.26	4.14 (0.04)	0.77 (0.10)	0.82 (0.02)	20.04	Y
217.822	c-C <sub>3</sub> H <sub>2</sub>	$6(1, 6) - 5(0, 5)$	38.6	-3.26	4.14 (0.04)	0.77 (0.10)	0.82 (0.02)	20.04	Y
219.560	C <sup>18</sup> O	$J = 2 - 1$	15.8	-6.22	4.15 (0.01)	0.97 (0.01)	1.70 (0.02)	19.27	N
219.949	SO	$6(5) - 5(4)$	35.0	-3.87	4.12 (0.06)	1.48 (0.14)	0.08 (0.02)	20.01	N
220.398	<sup>13</sup> CO	$J = 2 - 1$	15.9	-6.21	4.25 (0.01)	1.21 (0.01)	4.77 (0.05)	21.09	N
230.538	CO	$J = 2 - 1$	16.6	-6.16	...	...	...	...	...
231.321	N <sub>2</sub> D <sup>+</sup>	$J = 3 - 2$	22.2	-3.14	4.45 (0.06)	0.71 (0.19)	0.08 (0.02)	19.79	N
Receiver: nFLASH230, Tuning: 227.2 GHz, Mode: onOff									
224.714	C <sup>17</sup> O	$J = 3 - 2$	16.2	-6.19	4.28 (0.01)	1.51 (0.05)	0.28 (0.02)	18.25	N
225.697	H <sub>2</sub> CO	$3(1, 2) - 2(1, 1)$	33.4	-3.55	4.14 (0.01)	1.21 (0.02)	0.49 (0.02)	18.74	N
226.359	CN	$N = 2 - 1, J = 3/2 - 3/2$	16.3	-4.79	4.24 (0.04)	0.96 (0.12)	0.10 (0.02)	20.78	N
226.632	CN	$N = 2 - 1, J = 3/2 - 1/2$	16.3	-4.37	4.26 (0.03)	0.90 (0.08)	0.11 (0.02)	19.47	N
226.659	CN	$N = 2 - 1, J = 3/2 - 1/2$	16.3	-4.02	4.31 (0.02)	0.78 (0.03)	0.31 (0.04)	30.83	N
226.663	CN	$N = 2 - 1, J = 3/2 - 1/2$	16.3	-4.07	4.24 (0.08)	0.99 (0.20)	0.10 (0.04)	19.41	N
226.679	CN	$N = 2 - 1, J = 3/2 - 1/2$	16.3	-4.27	4.33 (0.08)	0.93 (0.08)	0.12 (0.04)	31.88	N
226.874	CN	$N = 2 - 1, J = 5/2 - 3/2$	16.3	-4.01	4.41 (0.01)	1.78 (0.04)	0.48 (0.03)	18.40	Y
226.875	CN	$N = 2 - 1, J = 5/2 - 3/2$	16.3	-3.94	4.41 (0.01)	1.78 (0.04)	0.48 (0.03)	18.40	Y
226.887	CN	$N = 2 - 1, J = 5/2 - 3/2$	16.3	-4.56	4.18 (0.04)	0.93 (0.10)	0.11 (0.04)	20.60	N
226.892	CN	$N = 2 - 1, J = 5/2 - 3/2$	16.3	-4.74	4.26 (0.04)	0.87 (0.07)	0.13 (0.03)	20.97	N
228.910	DNC	$J = 3 - 2$	22.0	-3.25	4.40 (0.02)	0.61 (0.05)	0.16 (0.03)	21.64	N
241.767	CH <sub>3</sub> OH	$5(1, 5) - 4(1, 4) E$	40.4	-4.23	4.12 (0.05)	1.04 (0.12)	0.08 (0.03)	26.21	N
241.791	CH <sub>3</sub> OH	$5(0, 5) - 4(0, 4) A$	34.8	-4.21	4.01 (0.03)	1.35 (0.07)	0.09 (0.02)	14.66	N
244.935	CS	$J = 5 - 4$	35.3	-3.52	4.16 (0.01)	1.21 (0.02)	0.31 (0.02)	16.86	N
Receiver: nFLASH230, Tuning: 227.2 GHz, Mode: off									
219.560	C <sup>18</sup> O	$J = 2 - 1$	15.8	-6.22	4.03 (0.03)	0.81 (0.10)	0.20 (0.05)	35.45	N
220.398	<sup>13</sup> CO	$J = 2 - 1$	15.9	-6.21	3.95 (0.01)	1.36 (0.02)	1.01 (0.05)	34.67	N
230.538	CO	$J = 2 - 1$	16.6	-6.16	...	...	...	...	...
Receiver: LAsMA345, Tuning: 344.2 GHz, Observation date: 2021-11-19, Mode: off									
345.795	CO	$J = 3 - 2$	33.2	-5.60	...	...	...	...	...
356.734 <sup>(*)</sup>	HCO <sup>+</sup>	$4 - 3$	42.8	-2.44	4.05 (0.06)	1.31 (0.12)	2.65 (0.63)	455	N
Receiver: SEPIA345, Tuning: 291 GHz									
279.511	N <sub>2</sub> H <sup>+</sup>	$J = 3 - 2$	26.8	-2.89	4.46 (0.01)	0.89 (0.02)	0.47 (0.03)	26.47	N
290.623	H <sub>2</sub> CO	$4(0, 4) - 3(0, 3)$	34.9	-3.16	4.09 (0.04)	1.36 (0.10)	0.79 (0.02)	18.83	N
293.912	CS	$J = 6 - 5$	49.4	-3.28	4.36 (0.03)	0.99 (0.08)	0.14 (0.02)	20.34	N

**Notes.** <sup>(a)</sup> Upper energy level. <sup>(b)</sup> Einstein coefficient. <sup>(\*)</sup> The spectrum was spectrally smoothed by a factor of 2 using the `smooth` built-in function in CLASS, and presented as such throughout this paper.

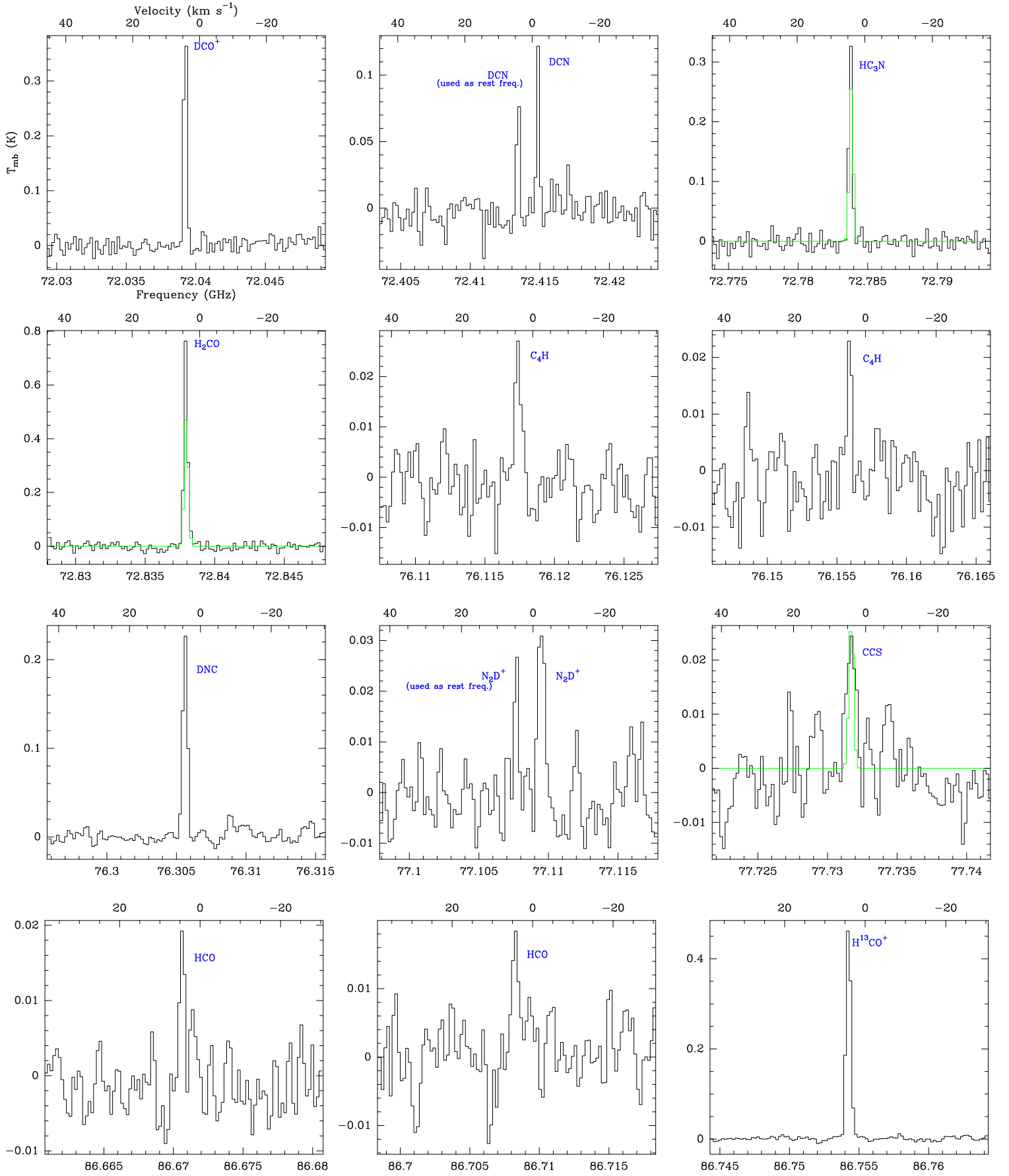


Fig. A.1: Spectra of lines detected towards V1057 Cyg with the IRAM 30-m telescope in the 73 GHz tuning, displayed in main-beam temperature scale. Molecule names for identified lines are labelled in blue, the synthetic model (displayed in the population diagrams in Fig. 7) is overlaid in green, tentative detections are labelled in dark green, and unidentified lines are labelled in red. In certain panels, extra text describes the species or transition used as rest frequency to display the top axis.



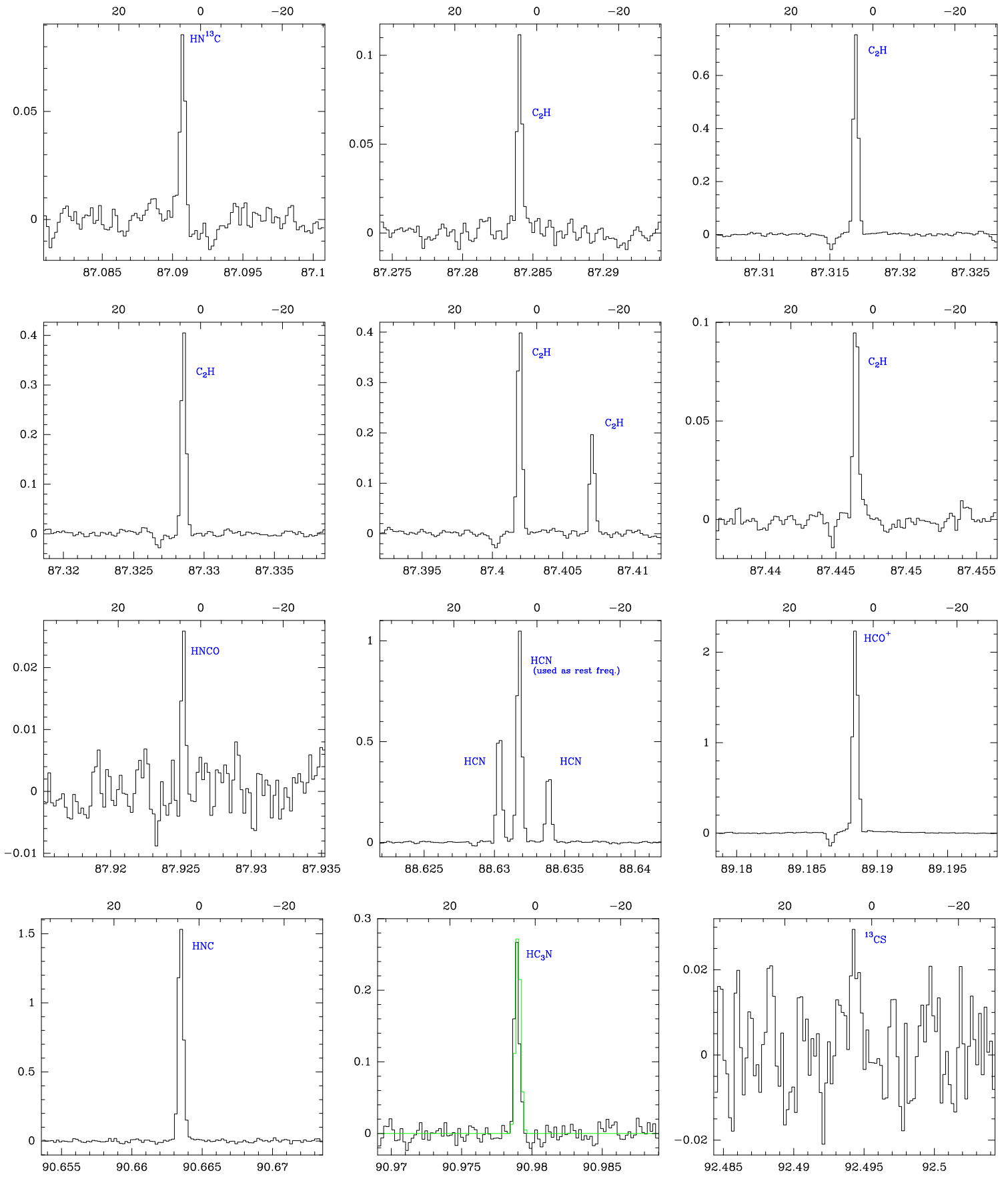


Fig. A.1: Continued.

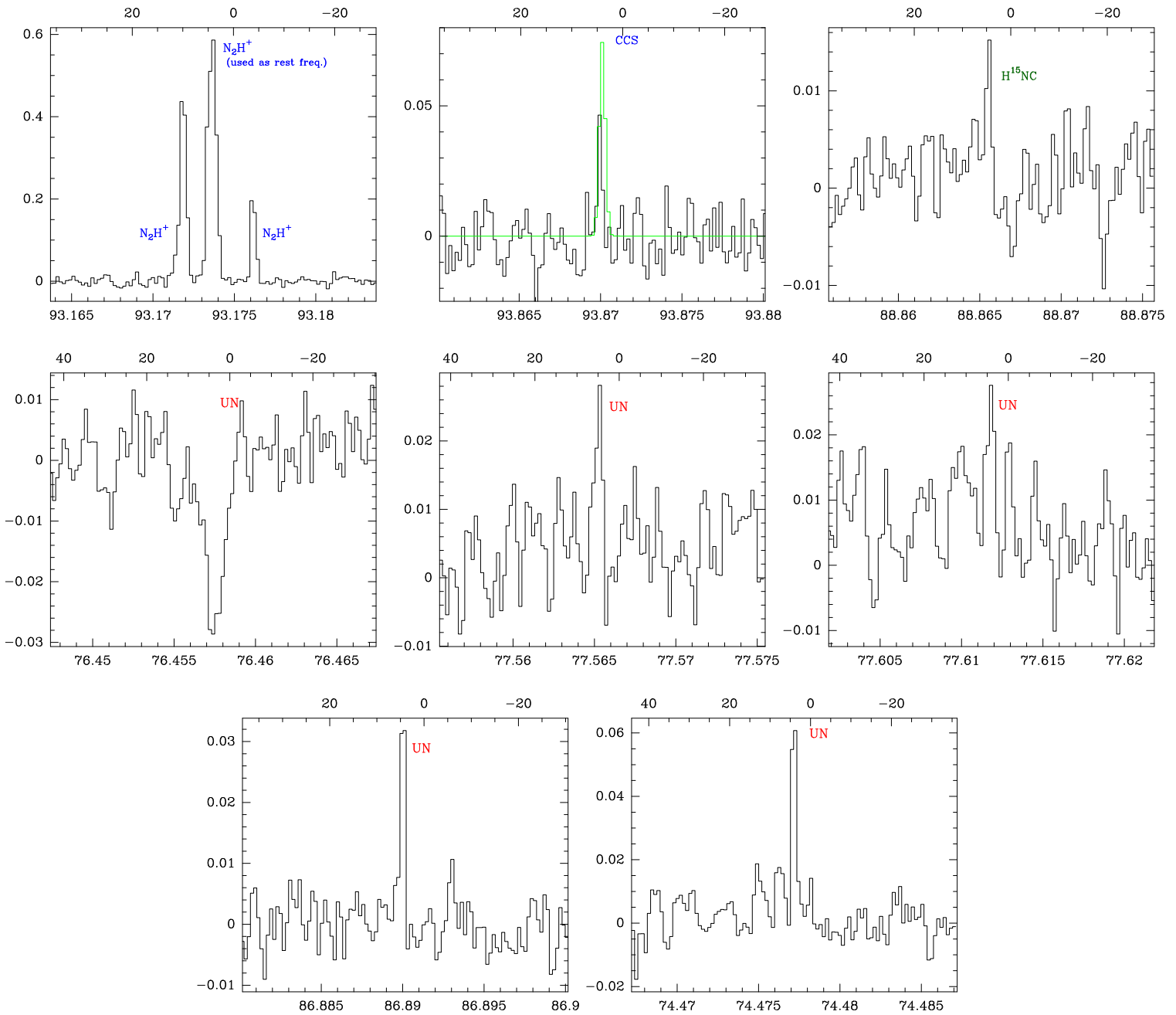


Fig. A.1: Continued.

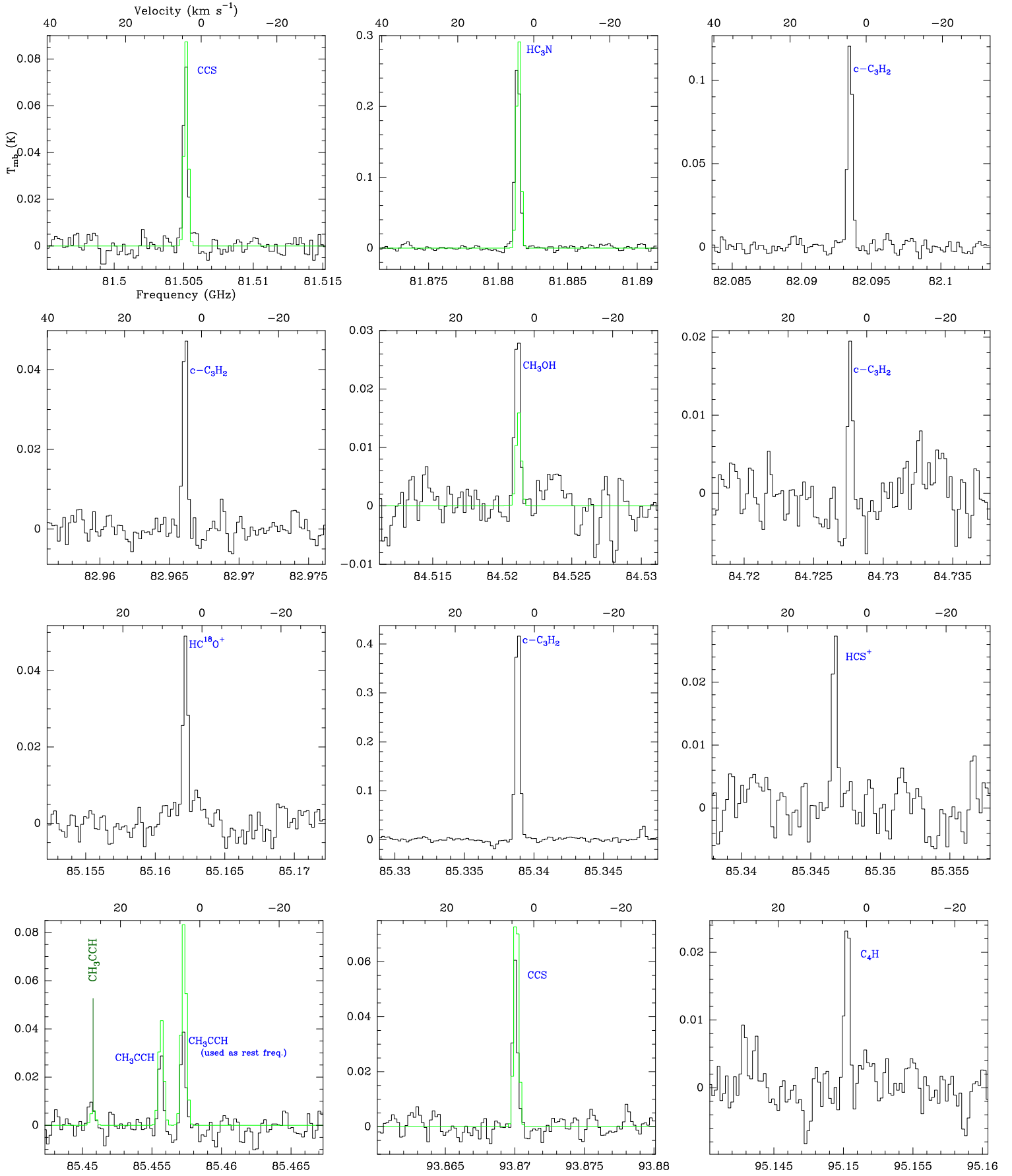


Fig. A.2: Same as Fig. A.1 but for the tuning at 80 GHz.

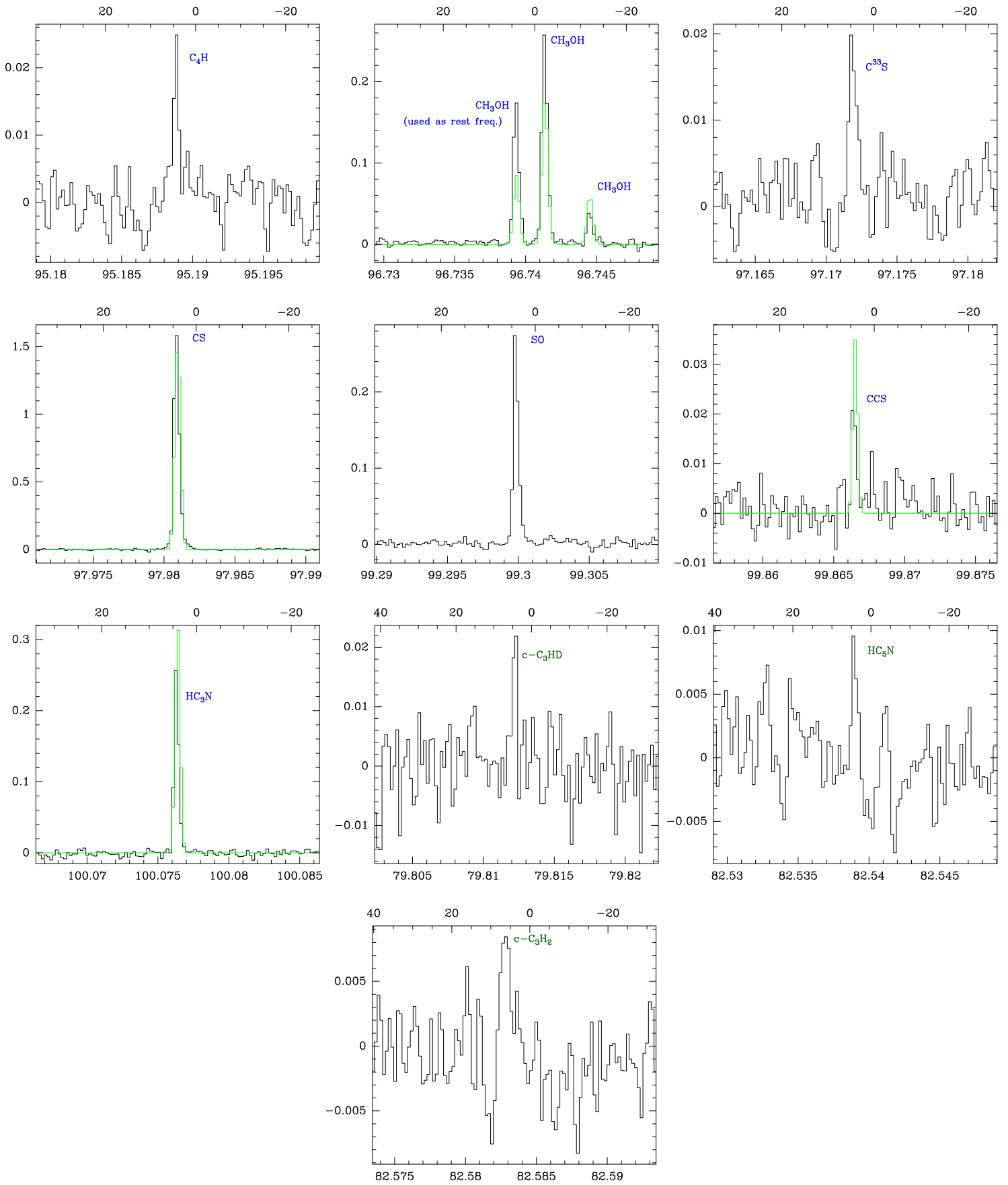


Fig. A.2: Continued.

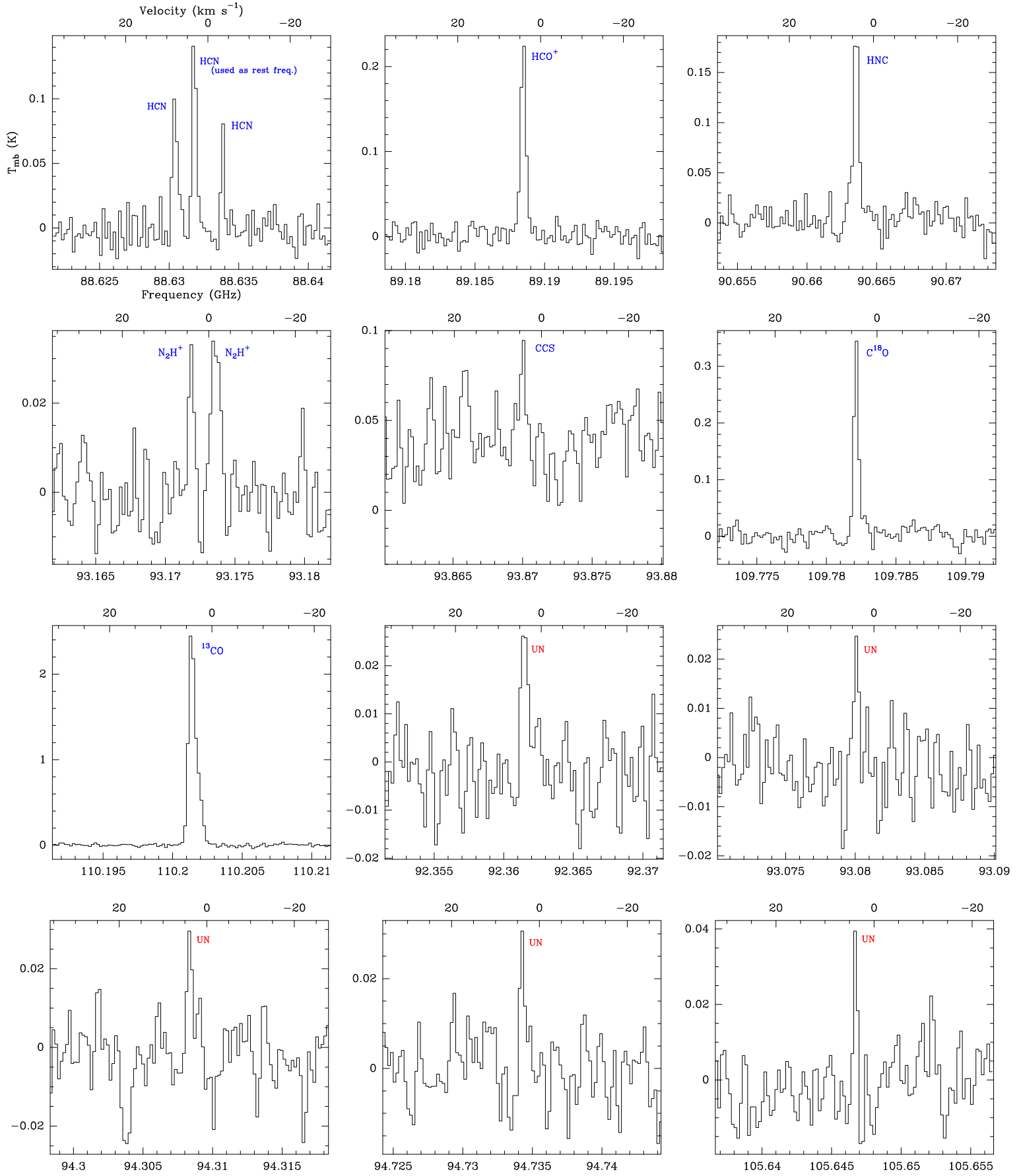


Fig. A.3: Same as Fig. A.1 but for the tuning at 90 GHz in the off mode at the source position.

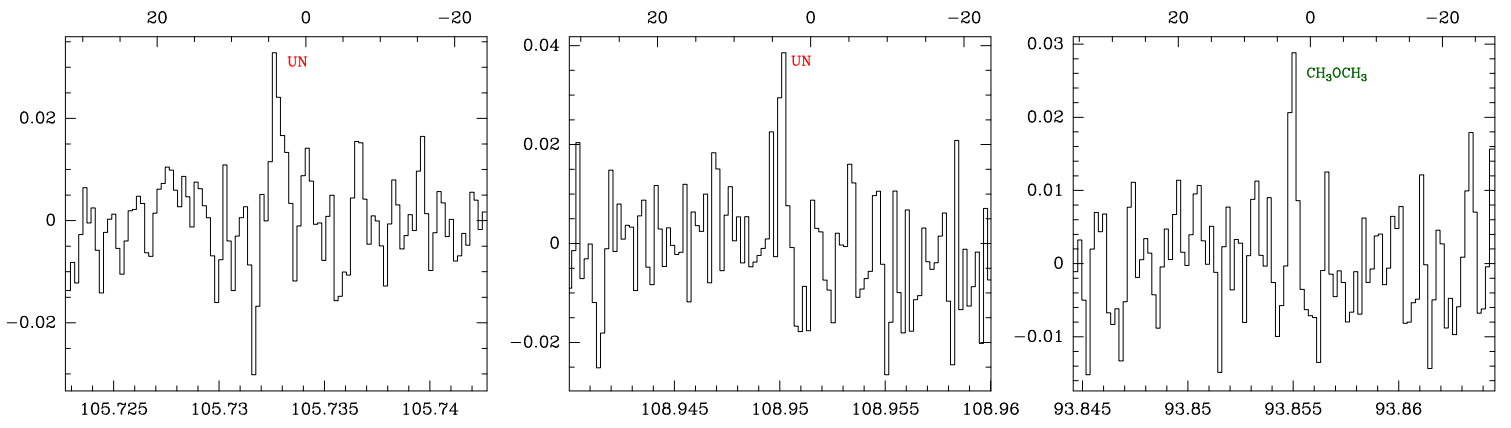


Fig. A.3: Continued.



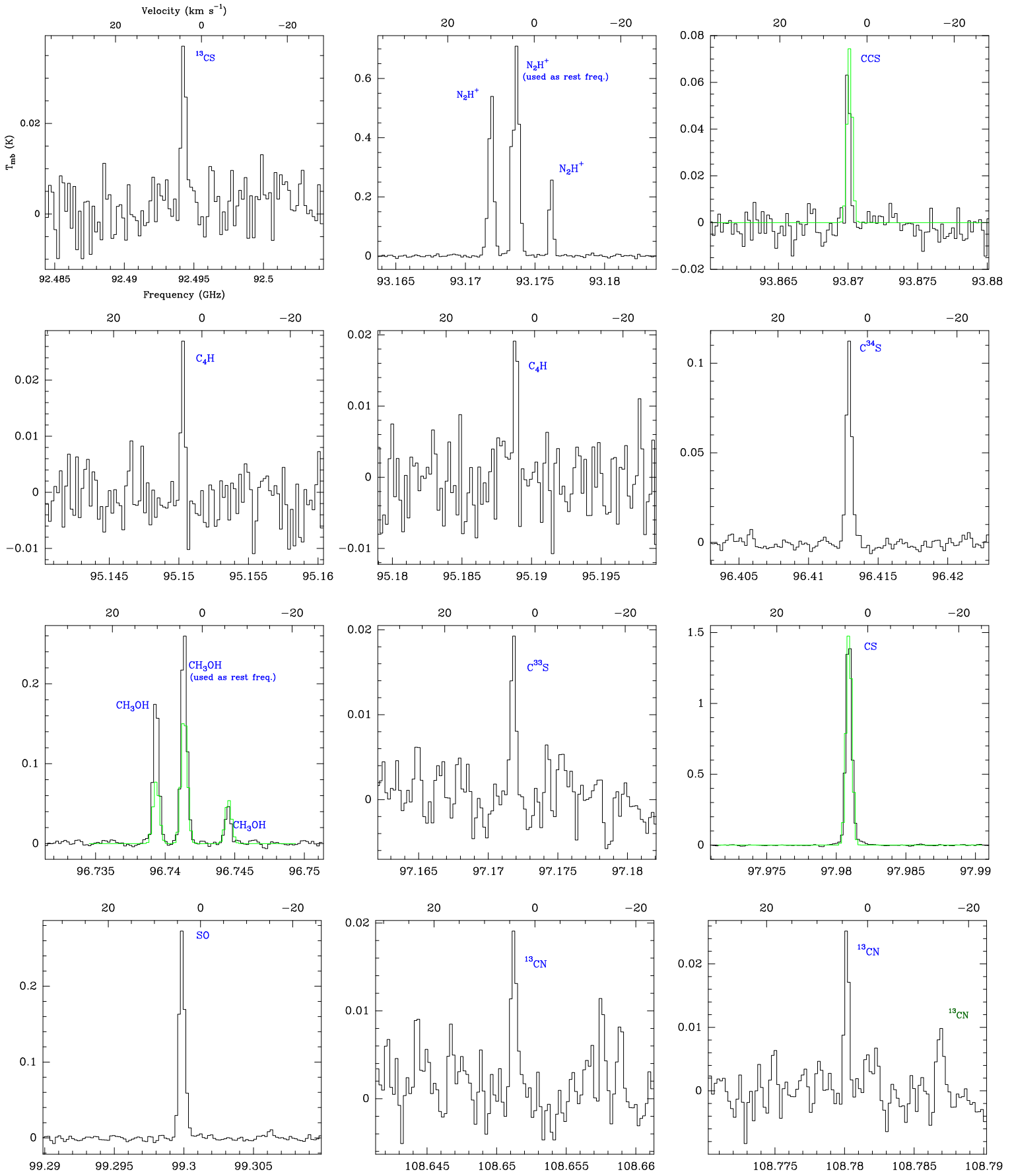


Fig. A.4: Same as Fig. A.1 but for the tuning at 94 GHz. Possible contamination from the image band (indicating rest frequency and peak temperature in K in the image band) are labelled in red.

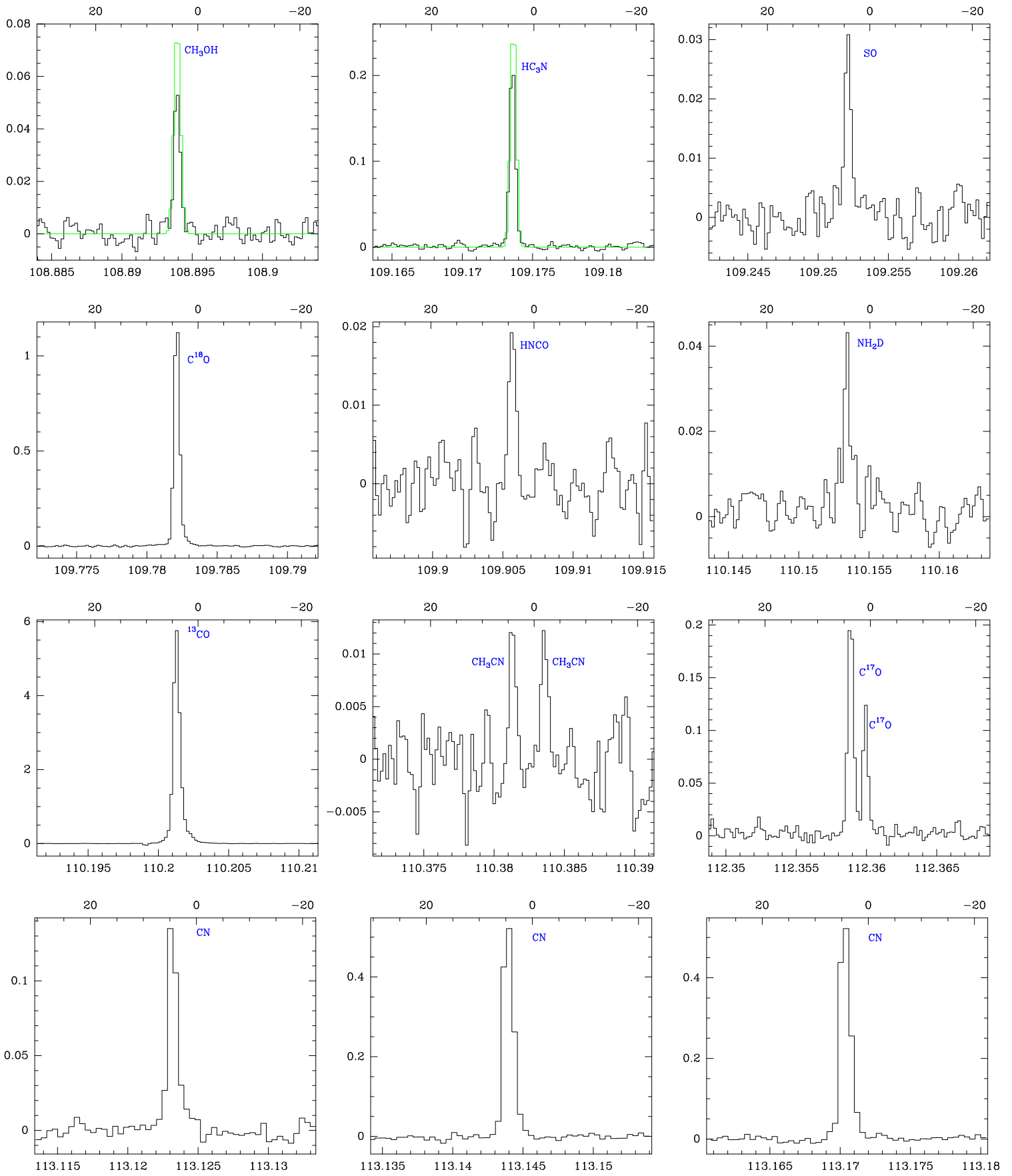


Fig. A.4: Continued.

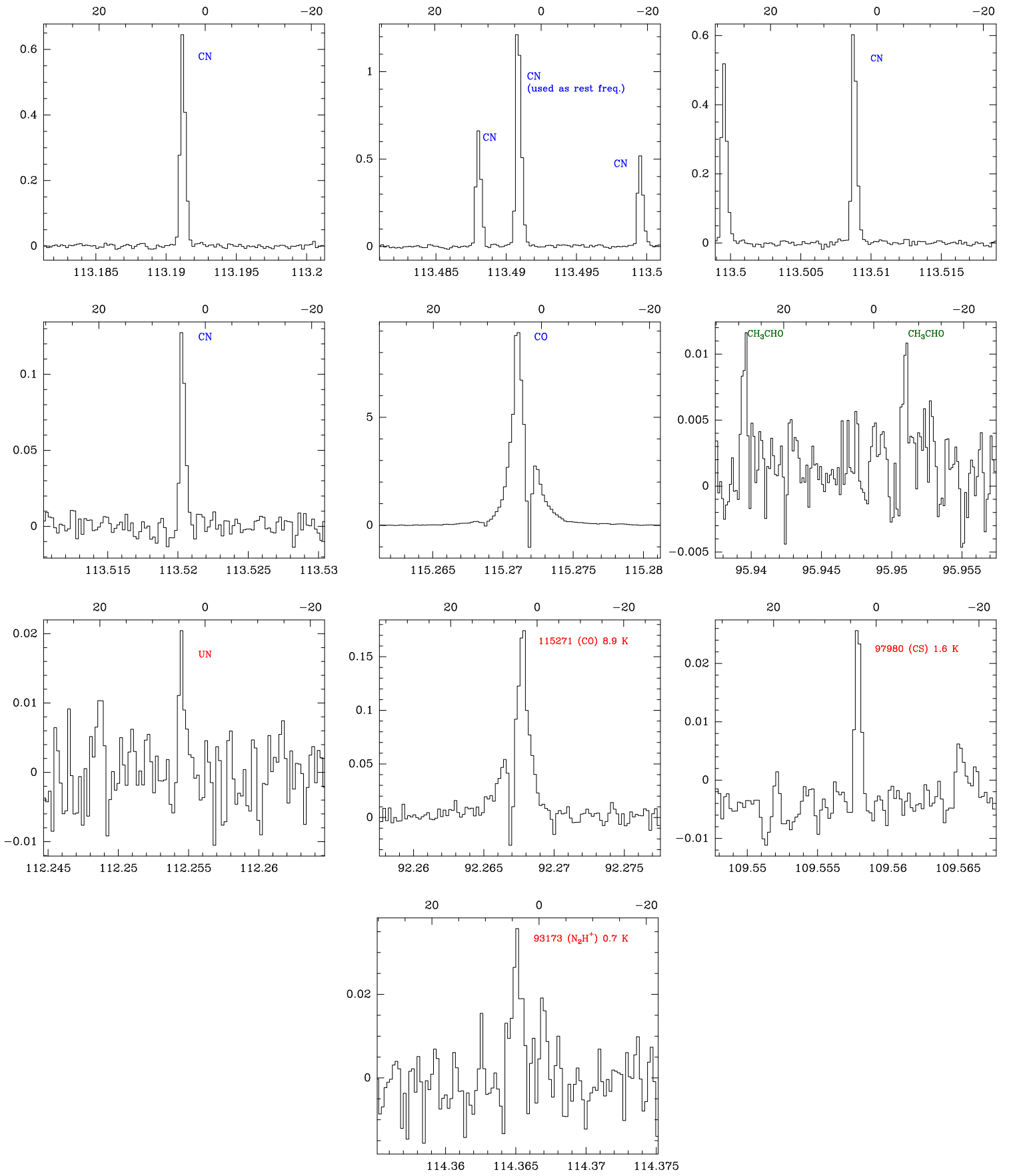


Fig. A.4: Continued.

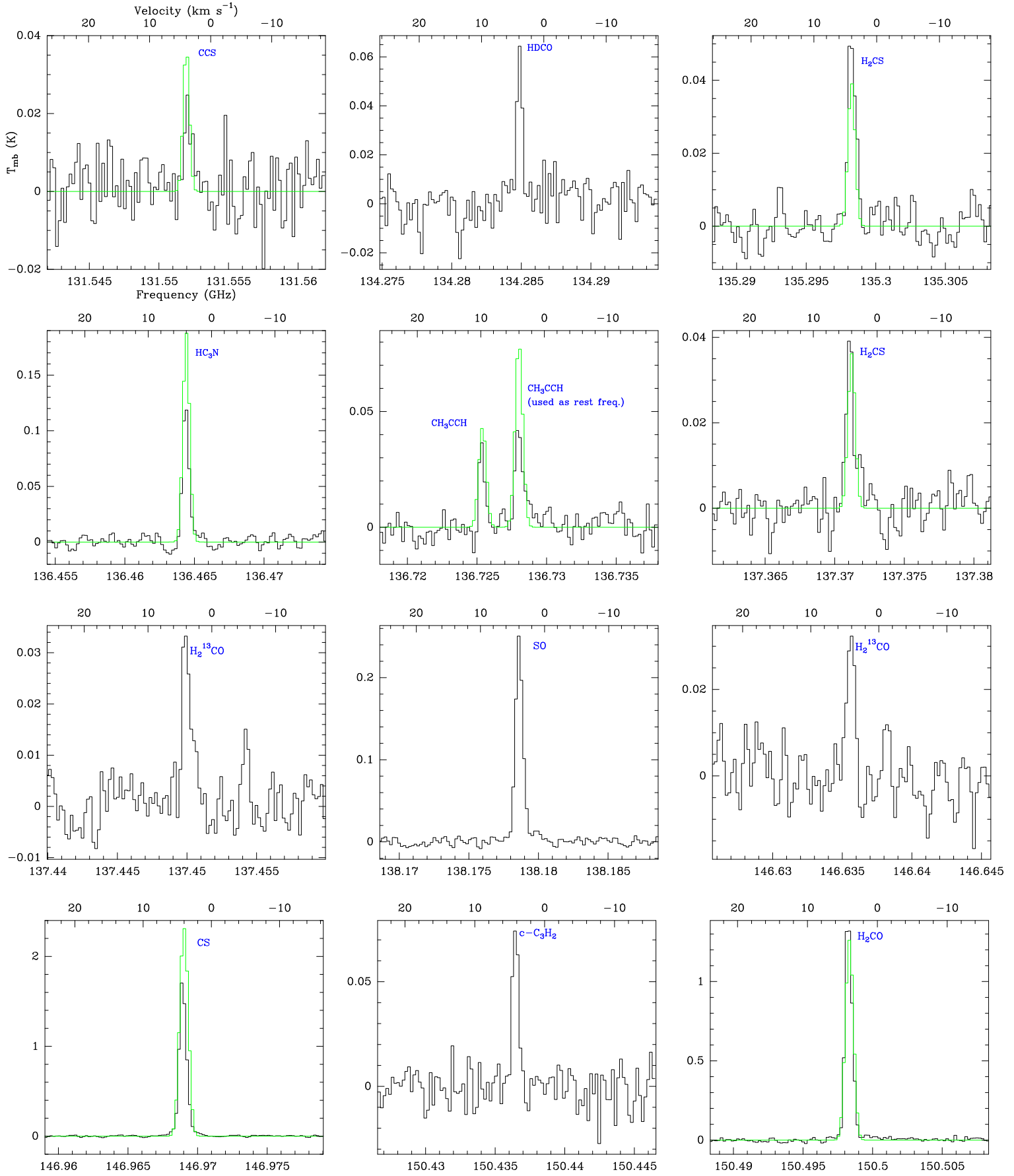


Fig. A.5: Same as Fig. A.1 but for the tuning at 133 GHz.

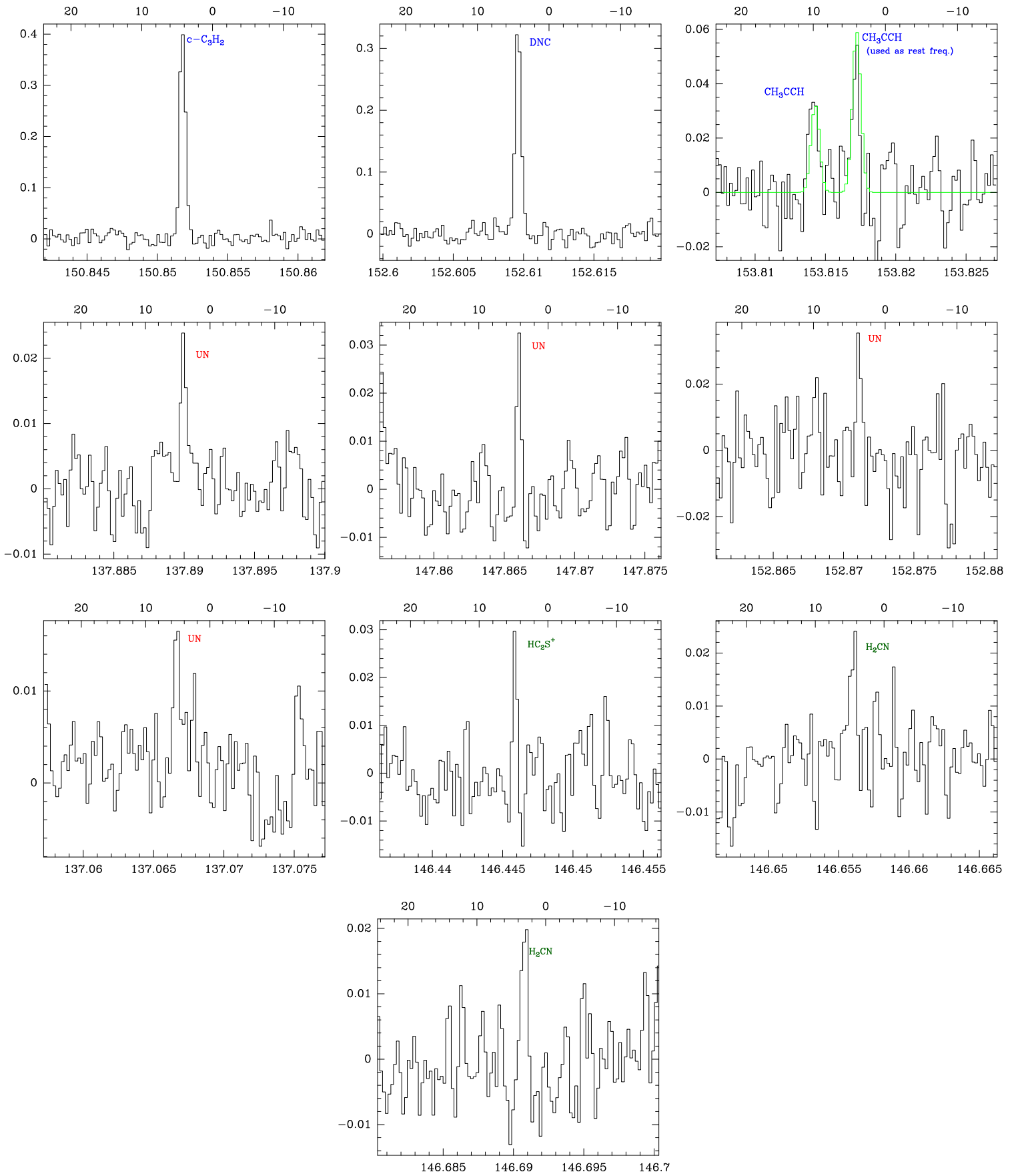


Fig. A.5: Continued.

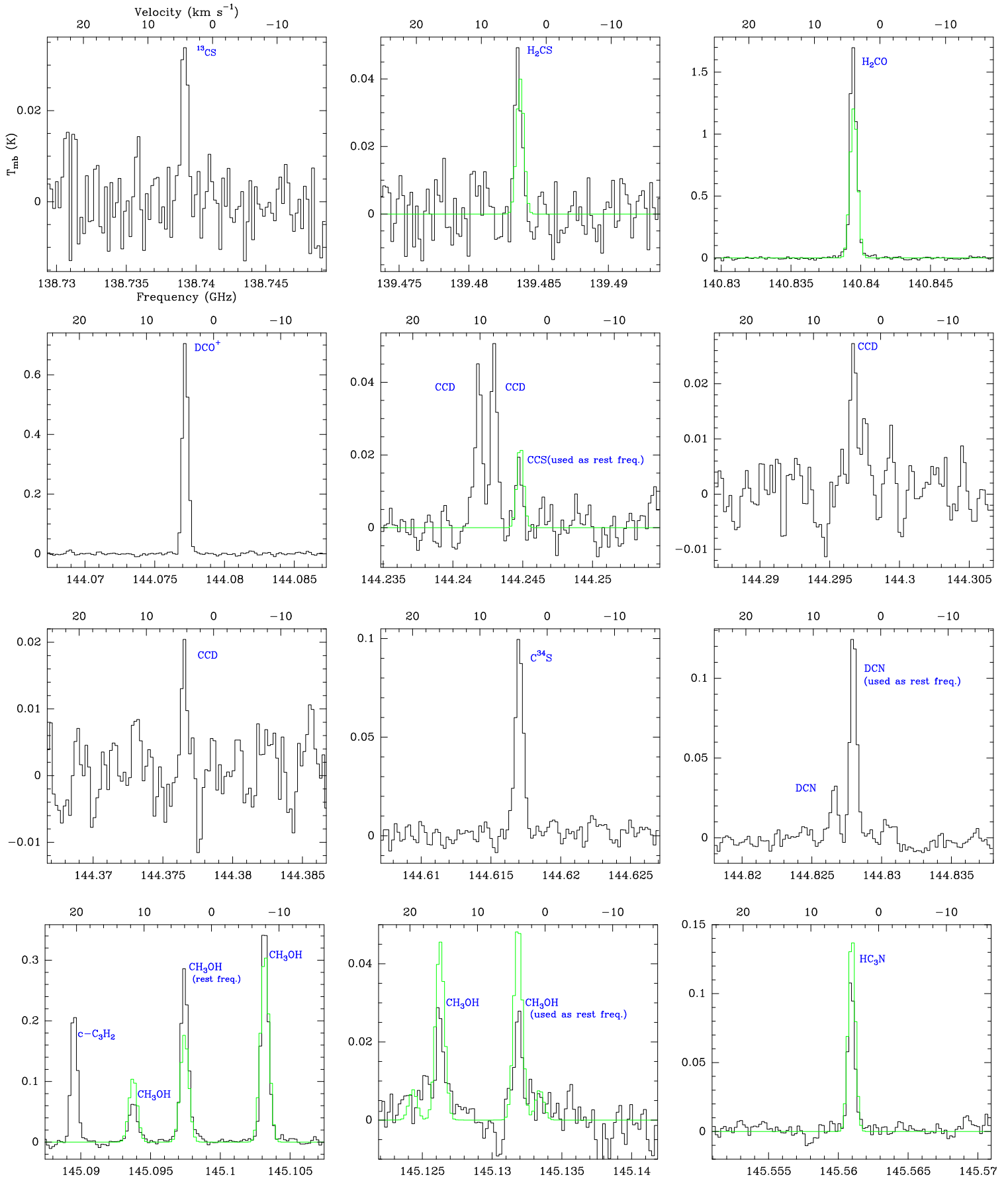


Fig. A.6: Same as Fig. A.1 but for the tuning at 141 GHz.

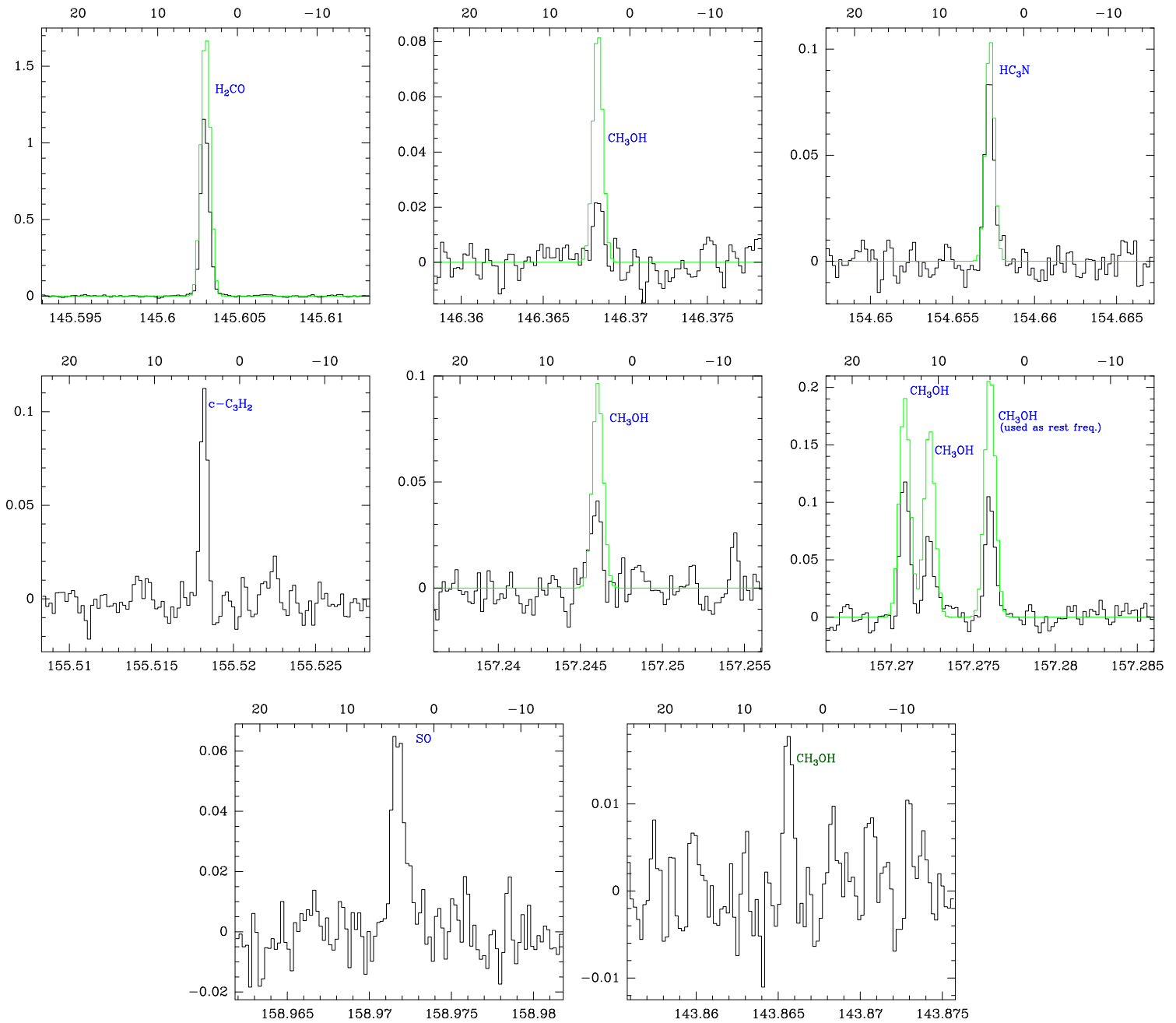


Fig. A.6: Continued.



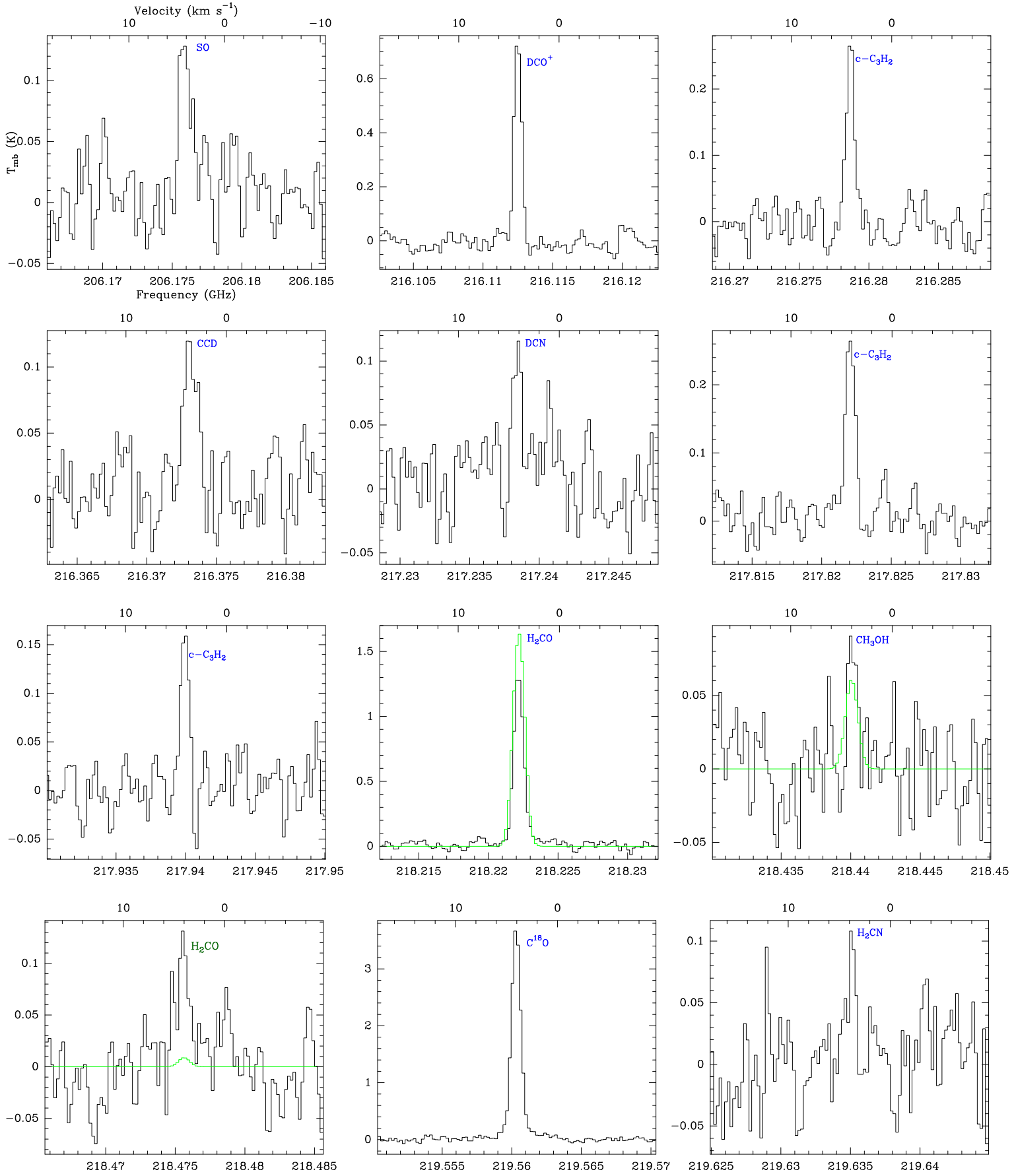


Fig. A.7: Same as Fig. A.1 but for the tuning at 202 GHz.

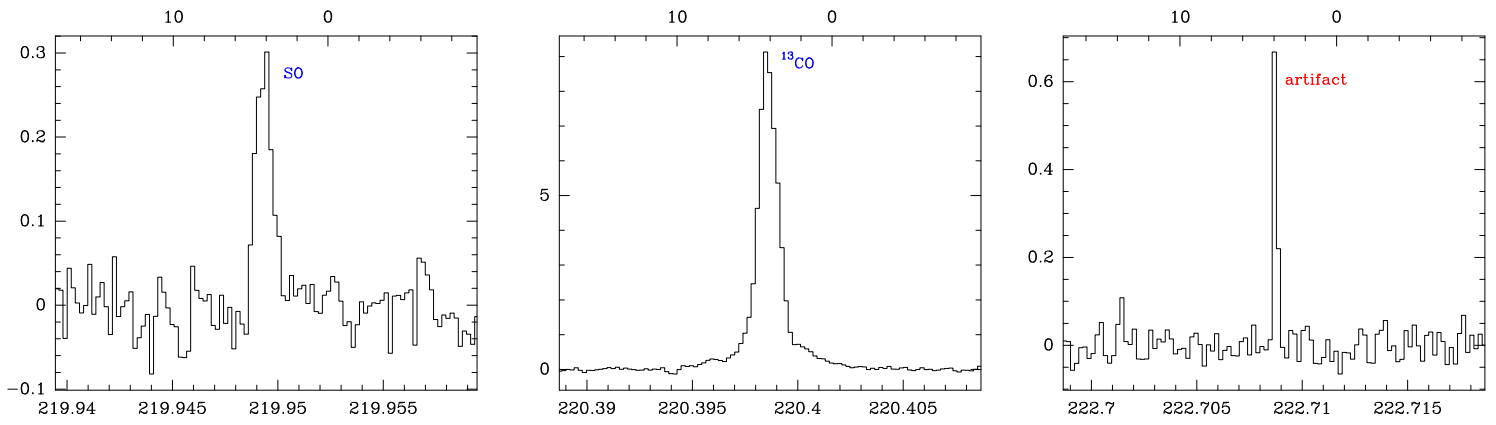


Fig. A.7: Continued.

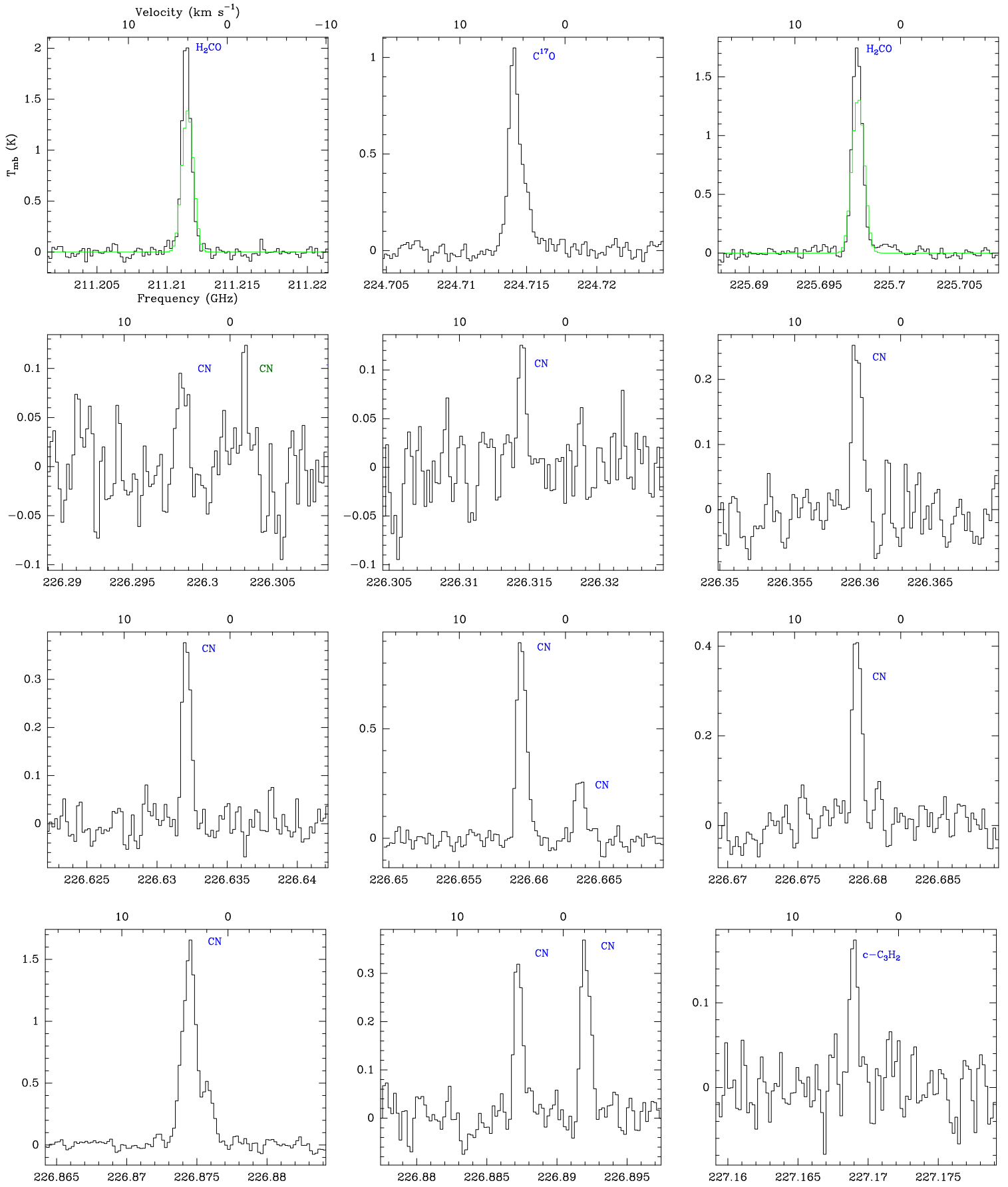


Fig. A.8: Same as Fig. A.1 but for the tuning at 210 GHz. Possible contamination from the image band (indicating rest frequency and peak temperature in K in the image band) are labelled in red.

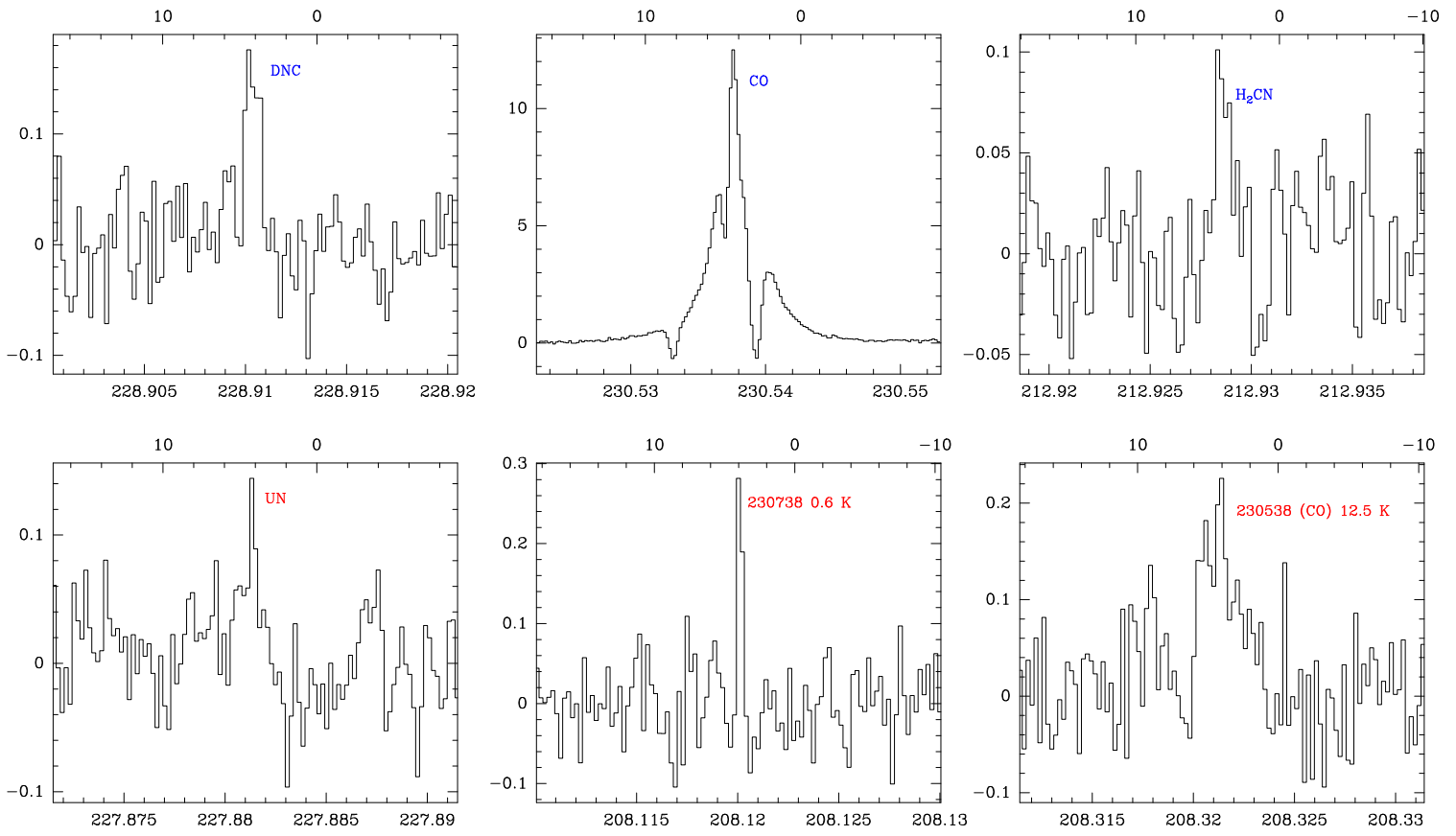


Fig. A.8: Continued.

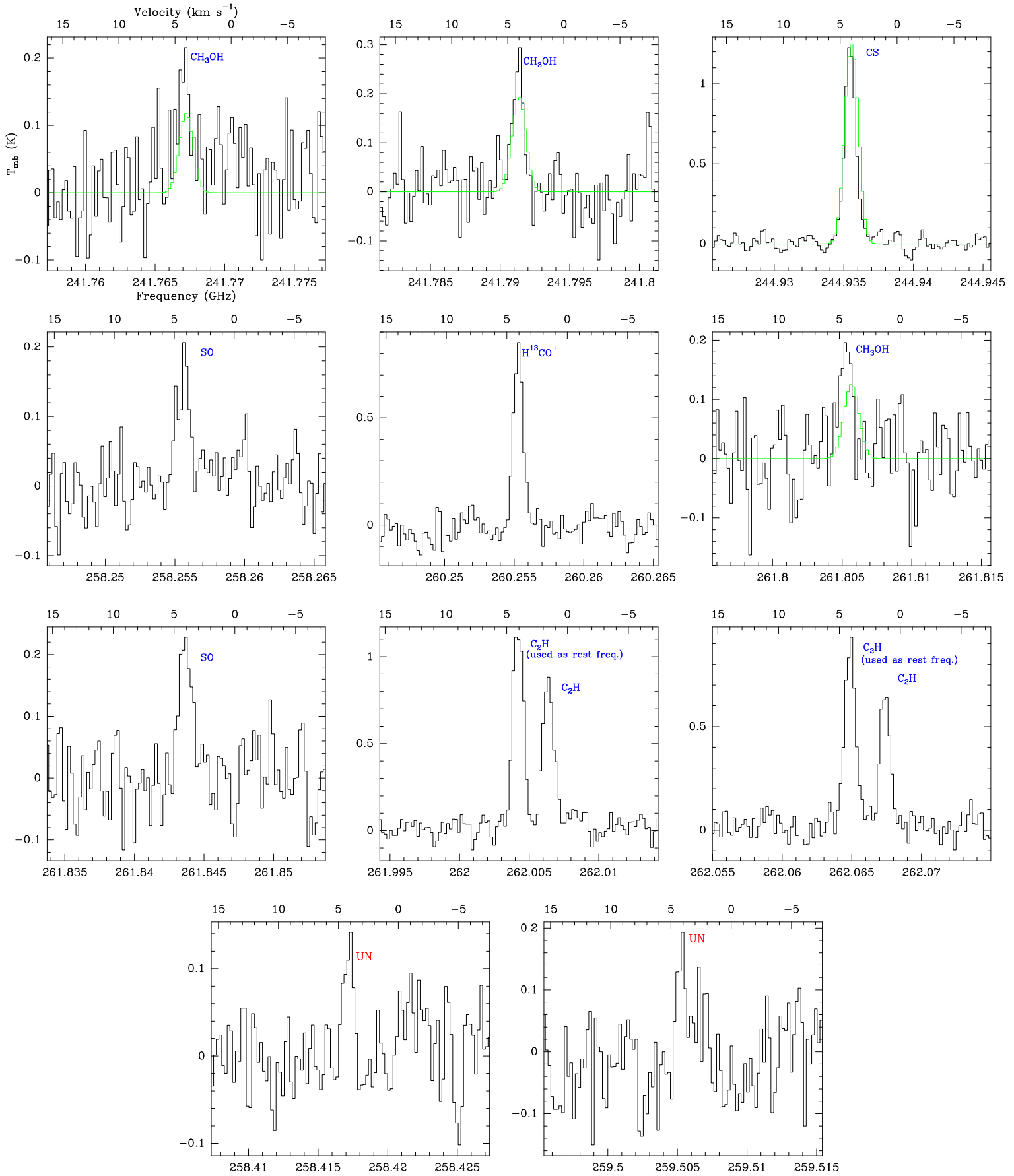


Fig. A.9: Same as Fig. A.1 but for the tuning at 242 GHz.



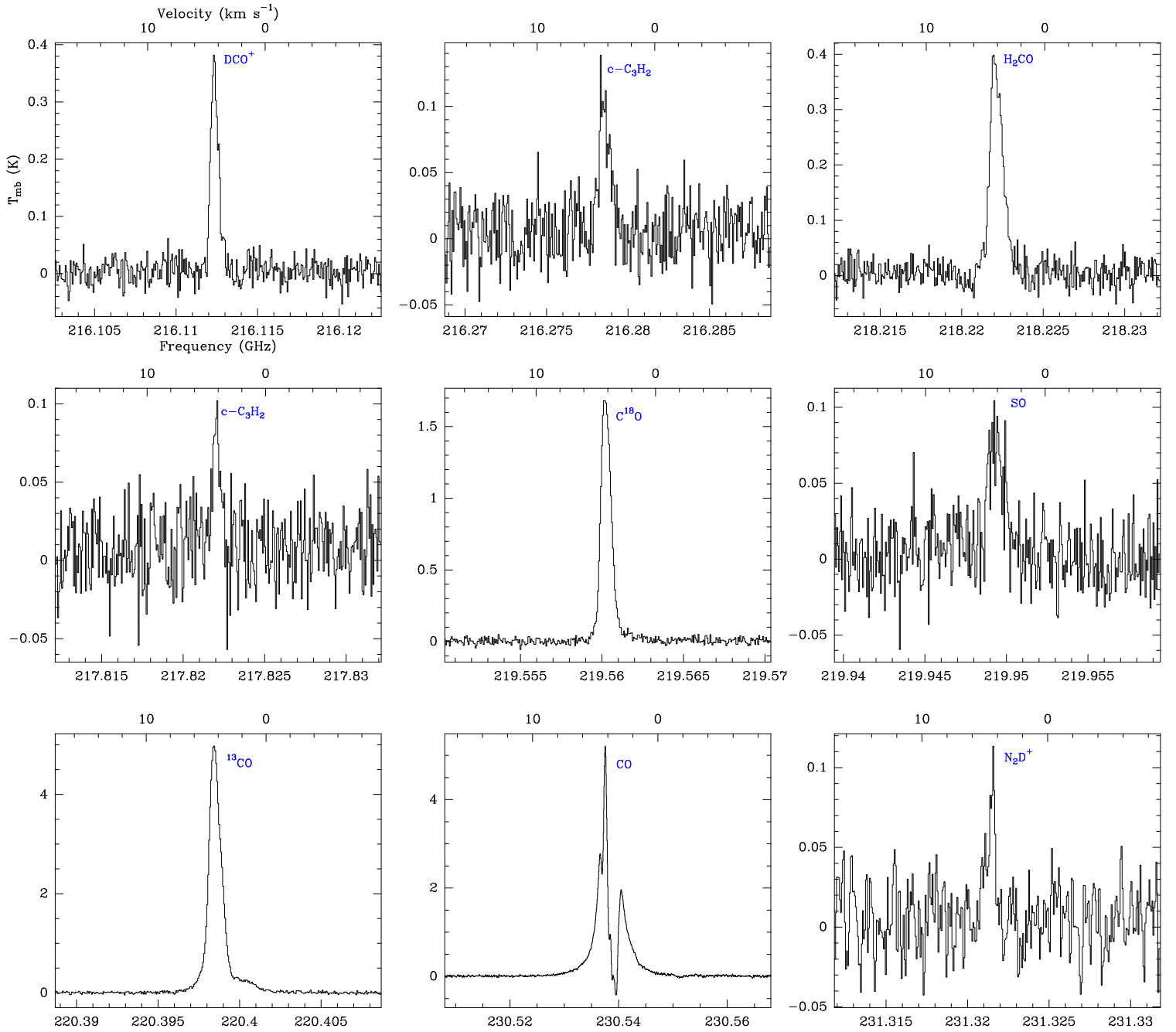


Fig. A.10: Spectra of lines detected towards V1057 Cyg with the APEX 12-m telescope with nFLASH, displayed in main-beam temperature scale. Molecule names for identified lines are labelled in blue.

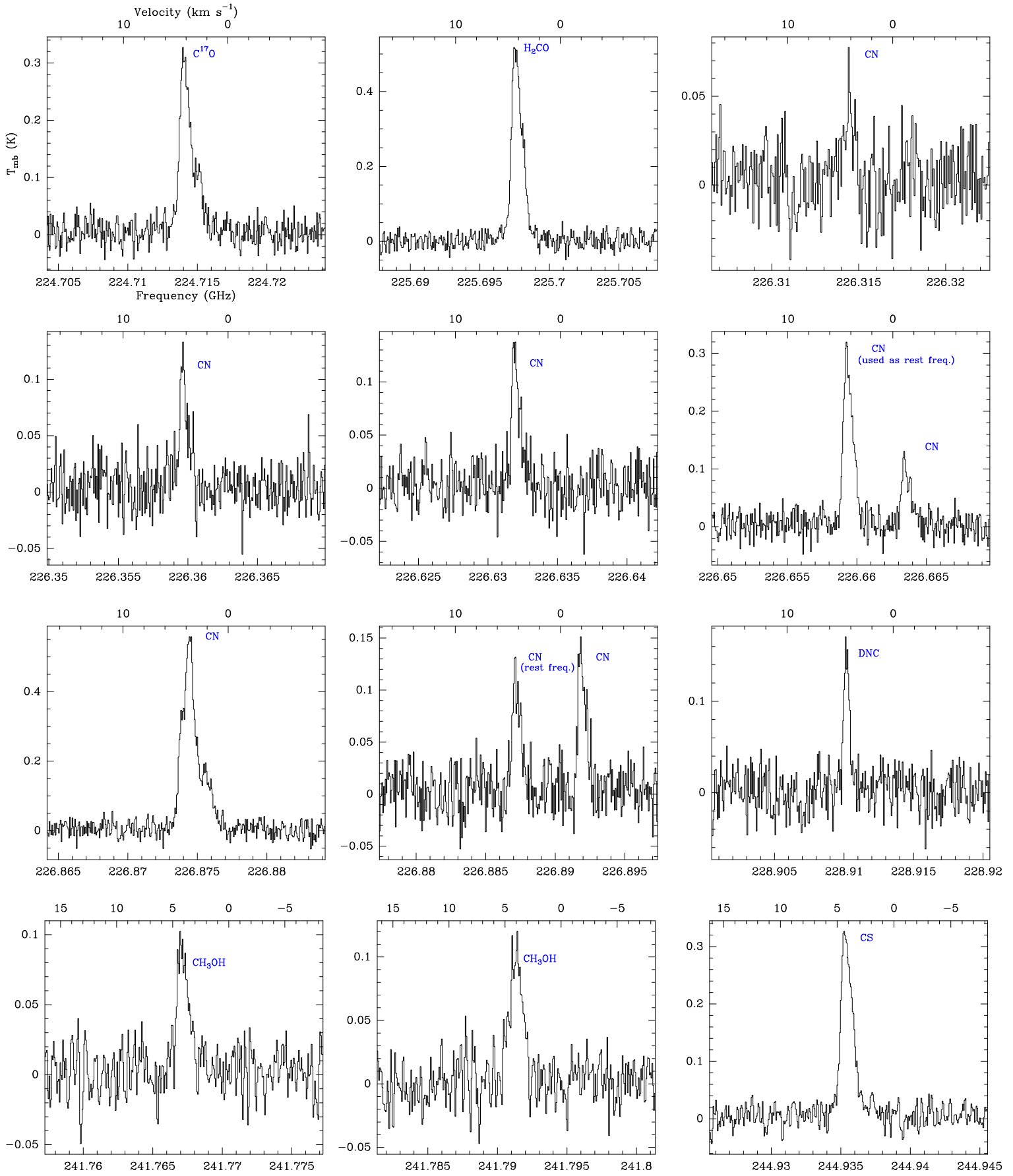


Fig. A.11: Same as Fig. A.10 but for the 227 GHz tuning.

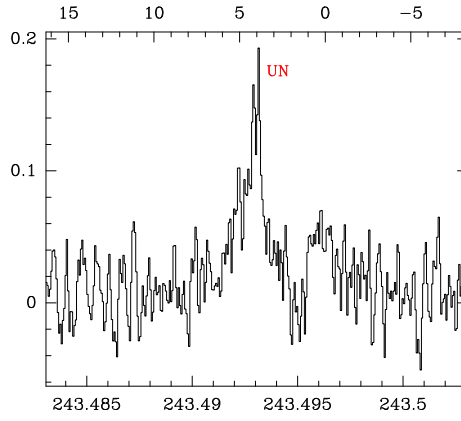


Fig. A.11: Continued.

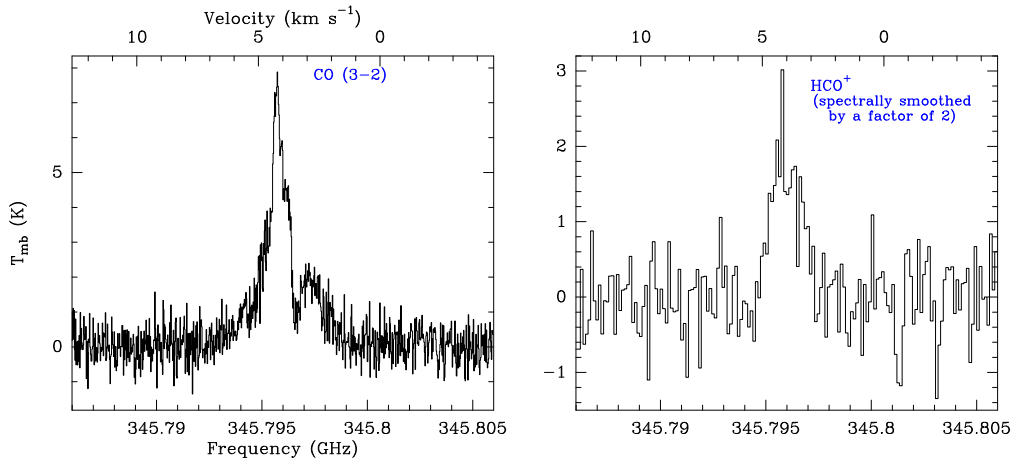


Fig. A.12: Spectra obtained at the position of V1057 Cyg (i.e.,  $0'',0''$ ) using the APEX 12-m telescope with LAsMA in the ofb mode, displayed in main-beam temperature scale. The names of identified lines are labelled in blue.

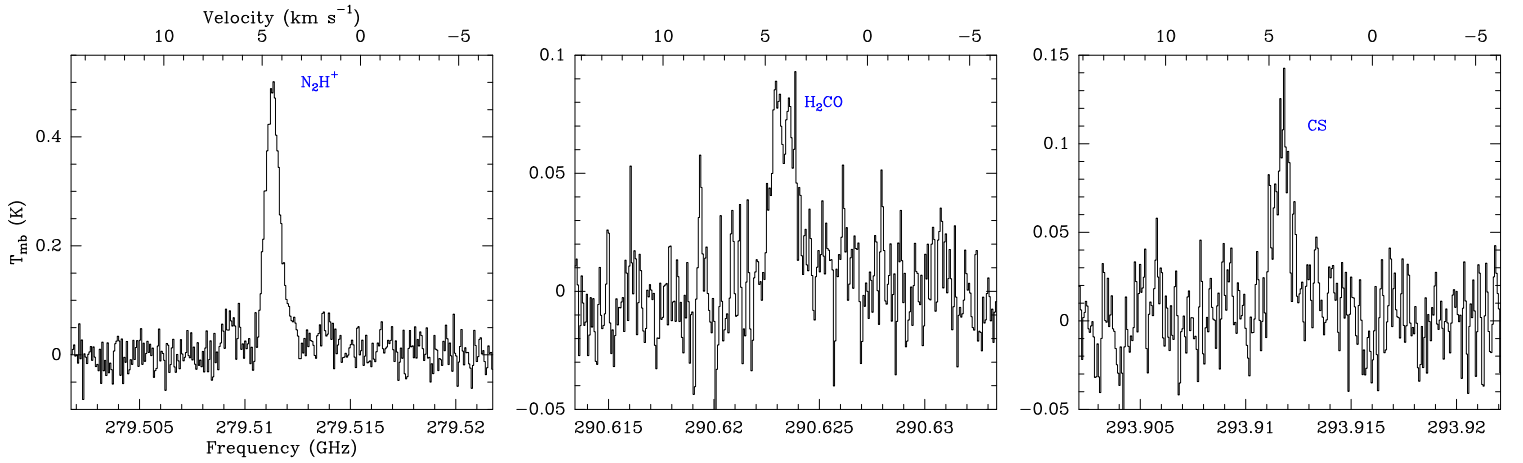


Fig. A.13: Spectra obtained towards V1057 Cyg with the APEX 12-m telescope with SEPIA, displayed in main-beam temperature scale. The names of identified lines are labelled in blue.